Doctoral Dissertation

A study of atomic scale mechanics by in situ transmission electron microscopy with a quartz length-extension resonator

Zhang Jiaqi

Supervisor: Professor Yoshifumi Oshima

Graduate School of Advanced Science and Technology

Japan Advanced Institute of Science and Technology

[Materials Science]

January 2021

Abstract

A study of atomic scale mechanics by in situ transmission electron microscopy with a quartz length-extension resonator

Zhang Jiaqi

s1820021

In this thesis, the mechanical properties of Pt and Au nanocontacts (NCs) are investigated by in situ transmission electron microscopy (TEM) observation combined with length-extension resonator (LER) to obtain structural information simultaneously with measuring the spring constant (force constant) and conductance measurements.

The Pt and Au NCs were fabricated with our developed *in situ* TEM holder, which equipped with a quartz length-extension resonator (LER) as a force sensor to examine the elastic properties of atomic-scale materials. The spring constants were determined based on shifts in the resonance frequency of the LER during TEM observation. The mechanical stability of our developed TEM holder was sufficient to allow chains of Pt atoms in the NC to be maintained for at least several seconds. This holder shows high mechanical stability therefore has significant potential with regard to the characterization of nanoscale mechanical properties.

Using our developed holder, we precisely determine the individual bond spring constant in tip-suspended platinum (Pt) monatomic chains using transmission electron microscopy combined with force spectroscopy enabled by a quartz length-extension resonator. We synthesize ~150 Pt monatomic chains consisting of 2–5 atoms. The single bond spring constant at the middle of chain is estimated to be 25 N/m, while that of the bond to the suspending tip is 23 N/m. The chain spring constant shows plateau-like behavior during stretching process, similarly to the quantized conductance. These characteristics including the breaking point are explained by the configurations minimizing the calculated string tension.

In addition, the deformation process and size effect on the Young's modulus of Au nanojunctions with diameter below 3 nm along the [111] direction is evaluated. The narrowest part of the plastic ultrathin nanocontacts becomes thinner under stretch while the angle of the pyramidal shape Au tips still constant. Such deformation process indicates the volume of the nanocontact is not constant and the additional atoms are migrating to the contact area through surface diffusion. The Young's modulus, which is calculated from the spring constant and corresponding geometrical information of the nanocontact, is found to be gradually decrease when the size is reduced. The size dependence of the Young's modulus can be explained by a core-shell model, which shows that the shell of 1 atom layer in thickness has very low Young's modulus (~25 Gpa) and the core has the similar value to the one of bulk [111] Au crystal. These results are in consistent of the observation of surface atom diffusion and indicate that the surface atoms play an important role in the mechanical properties of ultrathin nanomaterials.

Finally, the influence of dislocation on the mechanical properties for Au crystal has been studied. An edge dislocation was found to be appeared and disappeared repeatedly in the Au nanowire when it was stretched. The dislocation would be climbed up during stretching, and the new atom layer will be formed

leading to elimination of the dislocation. The spring constant of the nanocrystal will be largely reduced when the dislocation is formed and recover to the normal value after the dislocation is eliminated.

In conclusion, mechanical properties of atomic scale materials are investigated by our homemade TEM holder. Our result indicate that the atomic scale shows unique mechanical properties than the bulk one. The understanding of mechanics in atomic scale provide essential information for fundamental understanding and applications such as future atomic scale devices and catalyst.

Keywords: structure-dependent electronic properties, suspended graphene nanoribbons, in-situ TEM observation, nonequilibrium phase transitions, restructure

Table of Contents

Chapter 1 Background

Introduction

The first chapter will introduce the background on the nanoscale mechanics which have been mainly studied, and explains the recent progress on these topics.

In Chapter 1.1, we introduce the unique mechanical properties for nanoscale materials and how important is the mechanical properties for the materials. In Chapter 1.2, we give a brief overview of recent research progress about nano-mechanics from theoretical and experimental aspect of view. In Chapter 1.3, we show the propose and the method in this thesis.

1.1 Nano-mechanics

Metal nanomaterials has been reported to play important roles in future advance applications such as next generation nanodevices and catalyst [1-3]. Nowadays, nanoelectronic devices in 7 nm sizes scale have been commercialized, and we can expect that the devices in sub-3-nm regime will be realized soon. However, still there are many challenges for applying nanoscaled materials since their physical and chemical properties are much different from the properties of the bulk counterpart due to surface effects and quantum confinements [4-5]. Ohnishi et al. have found that the quantized conductance of Au nanocontact depended on the number of atomic chains. For example, one atomic row has the conductance of 1 G_0, and two atomic rows have the conductance of 2 G_0. as shown in figure1.1 [6]. Furthermore, quantized thermal transport characteristic is also found in Au atomic contacts and the Pt monoatomic chains have been reported to have emerging magnetic orders [7,8]. These unique properties provide more possibilities for future advanced applications. The mechanical properties, as one of the most important characteristic for the application and fundamental understanding of nanomaterials, have attract much interest in the world but still is a challenging task and has not been clarified yet [9].

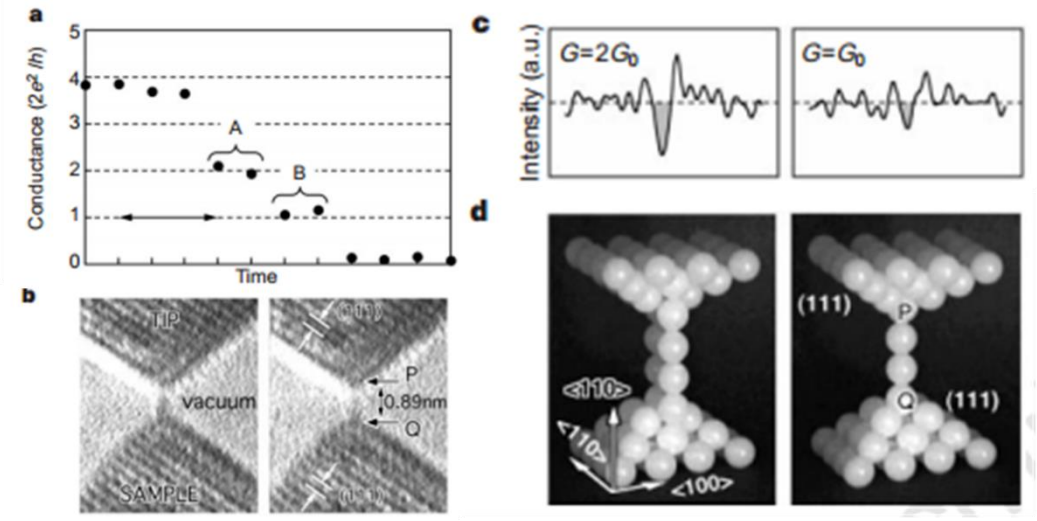

Figure 1.1 Conductance values of the Au nanocontacts and corresponding TEM images and structure models by Ohnishi et al [6].

Nanomaterials usually shows unique mechanical properties compared with the bulk one. For the nanomaterials, the surface to volume ratio is increased and the influence of surface atoms cannot be ignored [10]. So the size effect on the mechanical properties becomes obvious when the size of the material is small. The Young's modulus of ZnO nanowires have been found to be size dependent and have excellent elasticity, which has potential applications for NEMS and nanogenerators [11]. On the other hand, Sun et al. found that the sub-10-nm Ag nanoparticles show liquid-like pseudoelasticity behavior, which is useful for future shape-controlling nanodevices as shown in figure 1.2 [12]. The size effect on the Young's modulus of nanomaterials is also considered to be related to temperature. Ao et al pointed out that the Young's modulus of face centered

cubic (FCC) metals such as Au and Cu increased when the size is decrease at 0K, while it shows the opposite tendency at the room temperature as shown in Figure 1.3 [13].

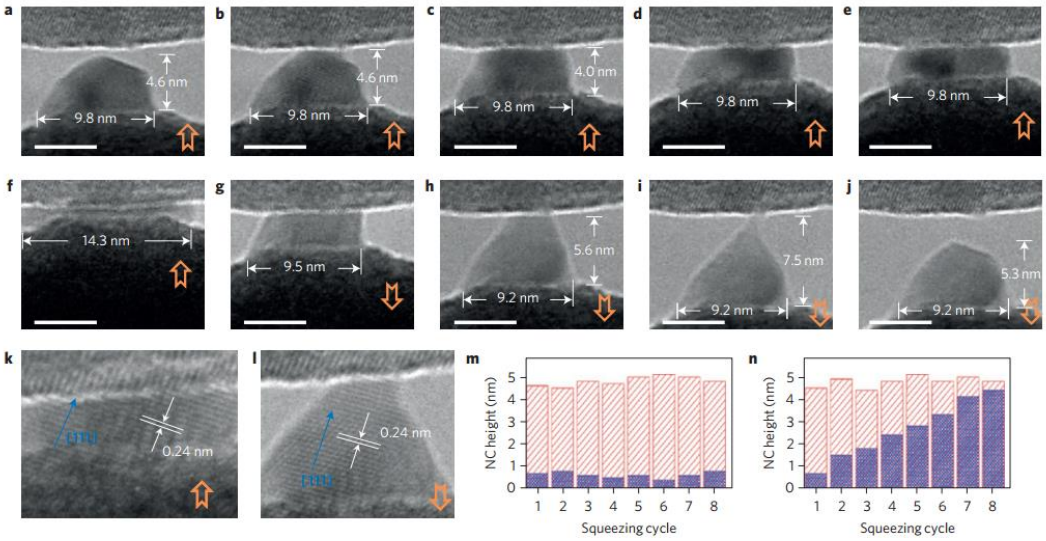

Figure 1.2 Liquid-like pseudoelasticity deformation behavior of the Ag nanoparticle observed by Sun et al [12].

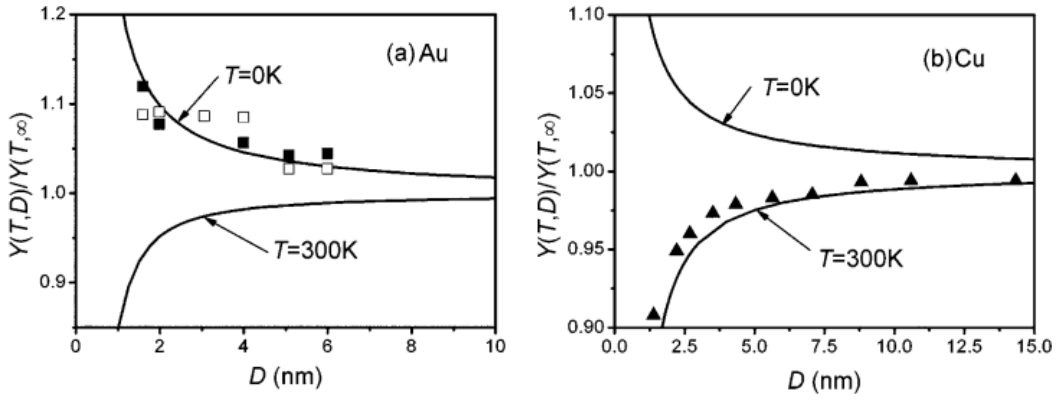

Figure 1.3 Size dependence Young's modulus as a function of diameter of the Au and Cu nanowires under 0K and 300K evaluated by Ao et al [13].

In addition, previous research indicated that the mechanical properties of nanomaterials strongly depended on their atomic structure such as the crystal orientation and the atom arrangement. Tavazza et al. pointed out that the electrical properties of Au monatomic chains were affected by their configurations such as the bond length and the angle between two bonds [14]. Quantum switching between 1 and 2 G0 ($= 2e^2/h$, where e is the elementary charge and h is the Planck constant) during mechanical displacement have been realized by controlling the zigzag configuration of the Au atomic chain: the conductance was found to depend on the angle between the bonds [15]. The special mechanical properties appearing in such nanocotacts or nanowires are suggested to depend on the change in the bond strength of surface atoms due to lack of coordination [16,17]. However, the previous results about them are not consistent with each other, and there is no consensus about the surface effect [18].

1.2 The previous investigation of nano-mechanics: A brief review

1.2.1 nano-mechanics investigated by theoretical approach

Many researchers have investigated the mechanical properties of nanomaterials by the density functional theory (DFT) calculations. Due to the limitation of the calculation resource, these calculations mainly focus on the structure consisting of several atoms in the cell. The energy of the system and equilibrium position of the atoms can be obtained by DFT calculation. The force response such as the breaking force and force constant of the nanomaterials can be estimated by from the first and second derivative of the energy. Zarechnaya et al, investigated the bond strength and breaking forces in atomic chains, dimers and bulk structures of Cu, Pd, Pt, Cu, Ag and Au metals within local density approximation (LDA) and generalized gradient approximation (GGA) by obtaining these interatomic potentials as shown in figure 1.4 [19]. The binding energy, breaking force and equilibrium bond length were analyzed. Their results indicated that Pt and Au were more likely to form the monatomic chains. On the other hand, Tavazza et al. use the Dmol3 code to exam the elongation and breaking process of the Au nanowires. They found that some intermediate structures were formed during the stretching process and the force needed to break the nanowire was consistent regardless of the deformation path [20]. Calvo et al pointed out that the relativistic effect played an important role in the mechanical properties and the formation of a single atomic contact [21].

For a larger system, molecular dynamics (MD) simulation method is often used, which is applicable up to several hundred atoms. The deformation process and force response can be obtained by such method. The Young's modulus and yield strength of 1-30nm <100> Au nanowires under the bending and tension mode have been investigated by Deb Nath et al. by MD simulations, they found nanowires with smaller diameter shows higher modulus and strength [22]. Diao et al. found that a surface-stress-induced phase transformation, which was from face-centered-cubic structure to a body-centered-tetragonal structure, was occurred in gold nanowires by the MD simulation [23].

However, there are many parameters such as the exchange-correlation functional or quasi-potentials to be chosen for the calculation. There parameters may strongly influence the calculated result. For example, Zhou et al. found that the size effect on the Young's modulus shows different behavior when they use the different potentials. The embedded atom method (EAM) potential shows that the materials become stiffer when the size is smaller, however, they become softer when they use the Lennard-Jones potential as shown in figure 1.5 [24]. The theoretical result shows the nanomaterials have unique mechanical properties but still not clarified.

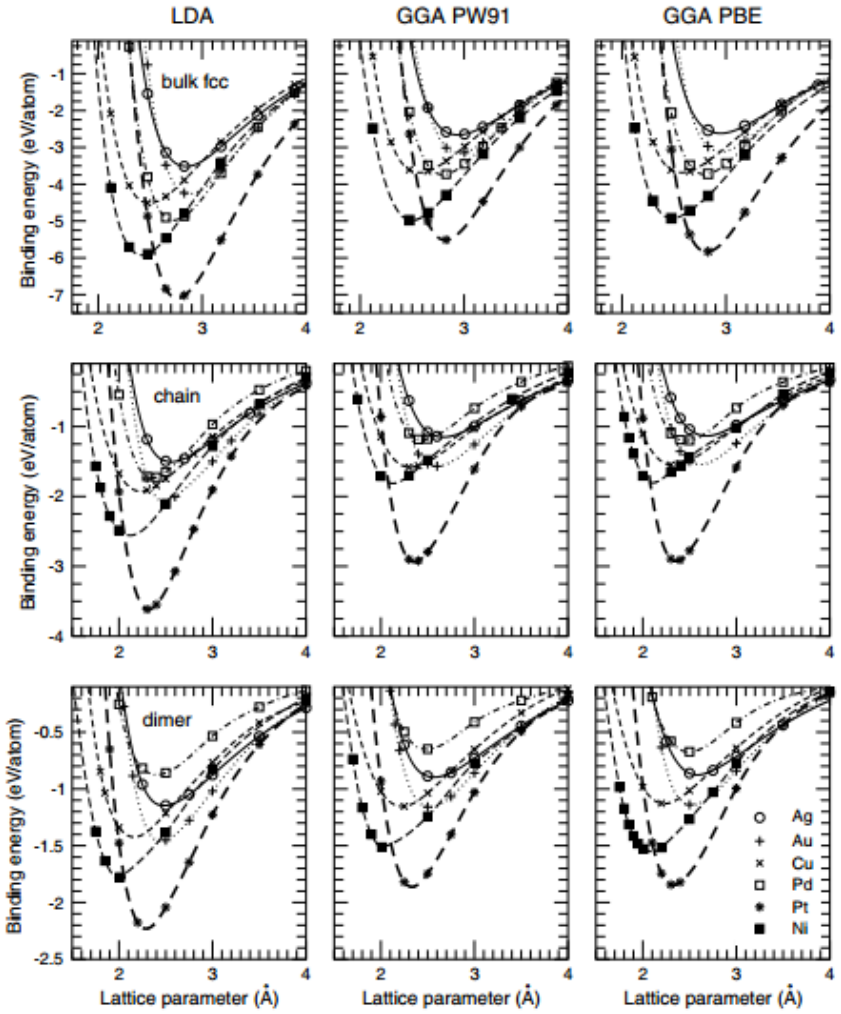

Figure 1.4 Binging energy as a function of interatomic distance for bulk fcc crystal, linear chain, and dimer structures of different element with different approximations by Zarechnaya et al [19].

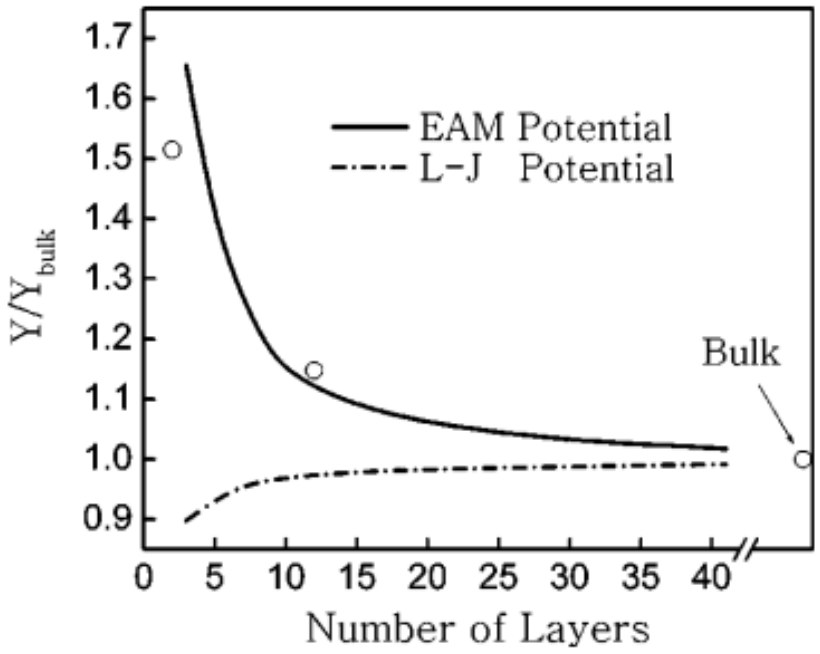

Figure 1.5 Young's modulus as a function of thickness of the nanoplate use EAM and Lennard-Jones potentials calculated by Zhou et al [24].

1.2.1 nano-mechanics investigated by experimental approach

In the past several decades, many researchers tried to understand the nano-mechanics by experiment approaches. Various of methods have been developed for investigating the mechanical properties of the nanomaterials such as optical based method and probe microscopy based method.

For optical based method, transient absorption or a Raman spectrum are used for characterizing the elastic properties of nanomaterials [25]. For example, Petrova et al. examined Young's modulus of gold nanorods in the [100] direction. The nanorods were

grown by seed mediated growth method. They found that the Young's modulus of the gold nanorod was measured to be about 31 GPa by transient absorption method as shown in figure 1.6 [26]. This value is smaller than that of the bulk crystal of the [100] direction (42GPa). However, the optical method can only obtain the mechanical properties of the materials in an area, which is averaged by amount of materials. It cannot measure the mechanical properties of individual materials. In detail, these structures are different among each other (such as the length, diameter or atomic structure).

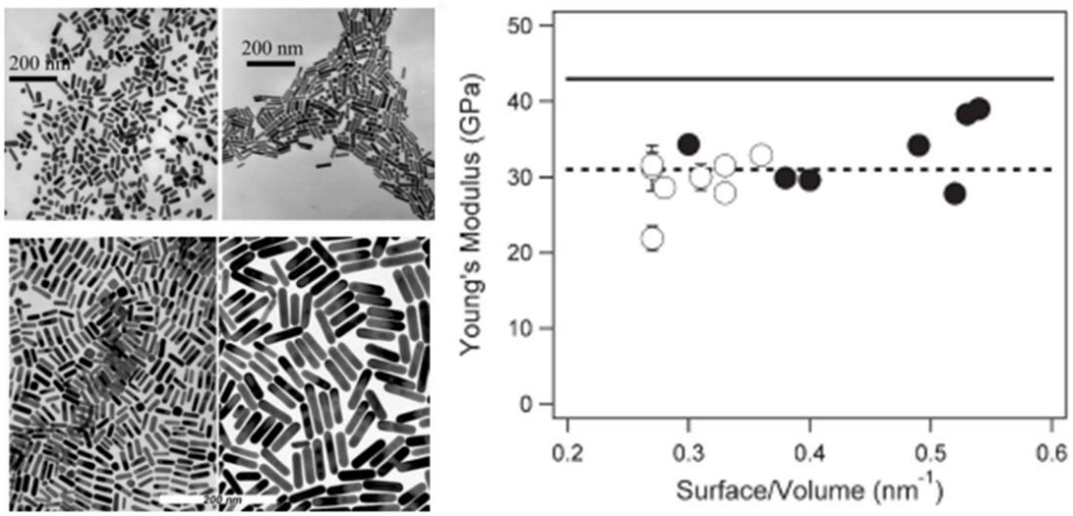

Figure 1.6 The prepared gold nanorod and Young's modulus by Petrova et al [26].

Previously, atomic force microscopy (AFM) was often used to obtain the force response of the nanomaterials. Typically, a silicon cantilever is used as the force censor, the force applied on the materials can be retrieved from the deformation and the spring

constant of the cantilever. Wu et al. used a cantilever to investigate the mechanical properties of an Au nanowire by bending it in the middle while both ends of the nanowire were fixed. They found that Young's modulus is independent of diameter in the range of 40-250nm as shown in Figure 1.7 [27].

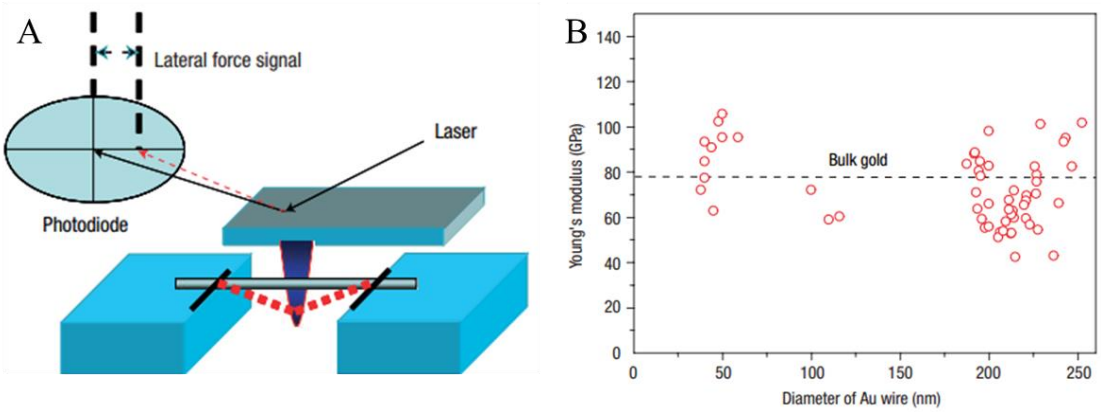

Figure 1.7 (A) Schematic of fixed wire in a lateral bending test with an AFM tip., (B) Size dependence Young's modulus of Au nanowires. By Wu et al [27].

Some researchers used frequency modulation method to investigate the mechanical properties of nanomaterials. By using such method, the gradient of force (force constant or so called spring constant) can be measured from the shift of the resonance frequency of the force sensor. Shiota et al. used mechanically controllable break junction (MCBJ) system combined with a tuning fork as a force sensor to investigate the mechanical properties of Pt nanocontacts and Pt atomic chains. The spring constant and conductance can be obtained at the same time by such system as shown in Figure 1.8 [28].

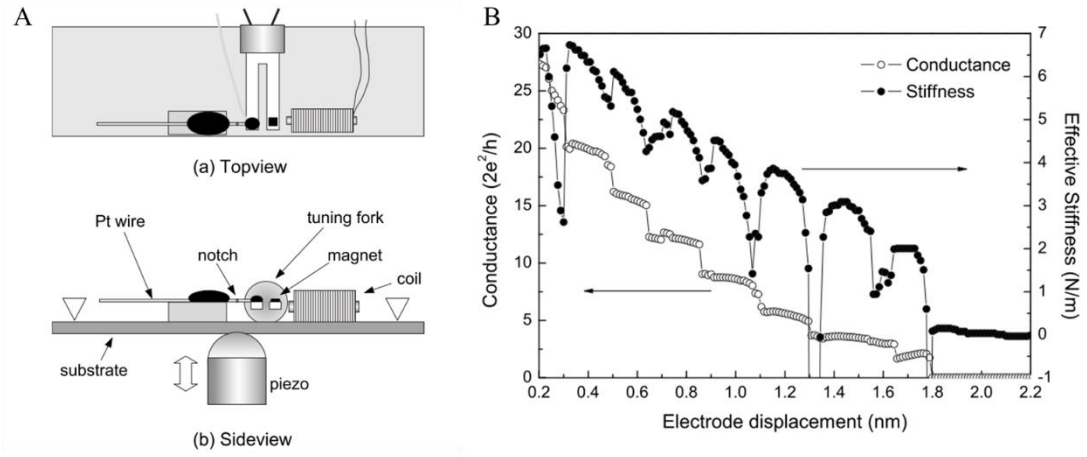

Figure 1.8 (A) Schematics of the MCBJ system combined with a tuning fork as a force sensor proposed by shiota et al. (B) conductance and spring constant measured by such system [28].

The force or force gradient of the nanocontact can be obtained by AFM or MCBJ method. However, it is difficult to get the structural information by such methods, which limit its applicable to clarify nano-mechanics because the physical properties strongly depend on the atomic configurations as mentioned. Some researchers use experimental approach to obtain a force response combined with DFT calculations to simulate the atomic configurations [29,30]. But the simulations cannot always represent the real one. To clarify both of the mechanical properties and corresponding atomic configuration of atom-sized material, force measurement combined with microscopy technique is required. For example, Lu et al. used transmission electron microscopy (TEM) with a Si

cantilever to investigate the fracture of Au nanowires as shown in figure 1.9. The force can be measured with the TEM observation [32]. However, it is difficult to estimate the elastic properties such as the Young's modulus by this method since the elastic elongation may be below 1nm, which is difficult to measure precisely in the TEM images.

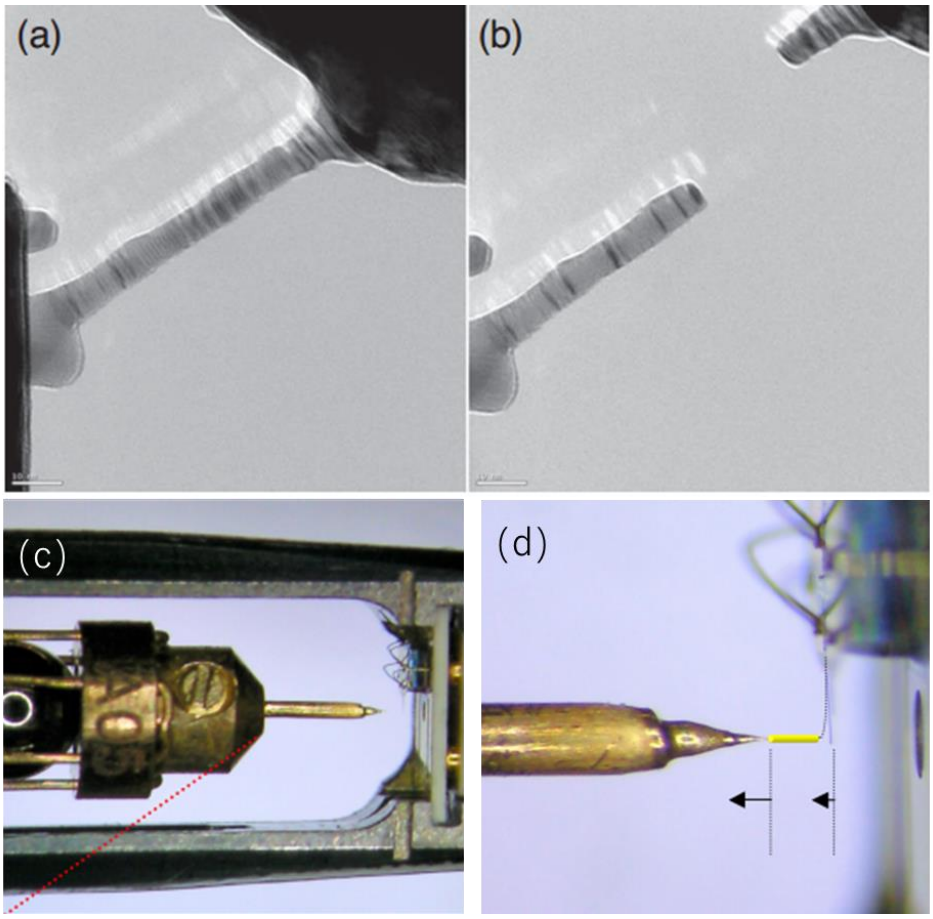

Figure 1.9 (a) and (b) TEM images obtained by the TEM-AFM holder. (c) photo of the TEM holder and (d) enlargement of the measurement part by Lu et al.

1.3 Purpose and method of present research

To address above issues, we have developed a TEM holder combined a length-extension resonator (LER) to simultaneously obtain the atom arrangement information, equivalent spring constant (force constant) and conductance measurements. The shape, size and crystal orientation of the nanocontact can be measured in the TEM images and the relation between the atomic configuration and mechanical properties can be analyzed from our data. Our *in-situ* TEM method is a powerful tool to investigate the nano-mechanics as we have discussed in the Chapter 1.2 and 1.3.

My work distinguishes from five key elements:

1. A TEM holder with a LER as the sensor was developed, an ultrasonic motor was chosen as the coarse motion. The conductance and spring constant values of the nanocontact can be measured at the same time by using this holder which shows high stability.
2. To precisely measure the spring constant value of the nanocontact, the properties (such as the sensitivity and spring constant) of LER was carefully evaluated. Au foil was chosen as the connection media to measure the conductance of the nanocontact.
3. Pt monatomic chains were formed before the Pt nanocontact rupture. The formation of Pt monatomic was confirmed from the TEM image and corresponding conductance value. The spring constant of monatomic chains with 2-5 atoms was

obtained. The individual bond spring constant in the chain could be estimated. The characteristics of mechanics of the bond are explained by the configurations minimizing the calculated string tension.

4. Au nanocontacts were fabricated along the [111] direction, and the deformation process was investigated in the TEM images. We foundd that Young's modulus of Au [111] nanocontact, which could be estimated from a differential method, reduced with decreasing the diameter. It can be explained by low Young's modulus of surface layer.
5. A dislocation assisted deformation process was discussed. An edge dislocation was found to be formed at the middle of the Au nanocontact. When stretching the nanocontact, the dislocation was climbed and finally eliminated to form a new atom layer. When further stretching, a new dislocation was created and eliminated repeatedly. The spring constant of the nanocontact reduced when the dislocation was formed, indicating that the dislocation weakened the strength of the Au contact.

Conclusion

In this chapter, we introduced specific features of nano-mechanics, which is the main topic in this thesis. Then we introduced the previous method to explore nano-mechanics from the theoretical and experimental aspect of view, both of the advantages

and limitations of these present methods were analyzed. Finally, we clarified the purpose of our research, the method and the main point of this thesis.

Reference

[1] A. Saffarzadeh, F. Demir, and G. Kirczenow, Thermoelectric Voltage Switching in Gold Atomic Wire Junctions, *Phys. Rev. B* 98, 115436 (2018).

[2] K. Terabe, T. Hasegawa, T. Nakayama, and M. Aono, Quantized Conductance Atomic Switch, *Nature* 433, 47 (2005).

[3] A. M. Lord, Q. M. Ramasse, D. M. Kepaptsoglou, P. Periwal, F. M. Ross, and S. P. Wilks, Stability of Schottky and Ohmic Au Nanocatalysts to ZnO Nanowires, *Nano Letters* 17, 6626 (2017).

[4] M. A. Meyers and K. K. Chawla, Mechanical Behavior of Materials (Cambridge university press, 2008).

[5] N. Agraït, Quantum Properties of Atomic-Sized Conductors, *Physics Reports* 377, 81 (2003).

[6] H. Ohnishi, Y. Kondo, and K. Takayanagi, Quantized Conductance through Individual Rows of Suspended Gold Atoms, *Nature* 395, 780 (1998).

[7] L. Cui, W. Jeong, S. Hur, M. Matt, J. C. Klöckner, F. Pauly, P. Nielaba, J. C. Cuevas, E. Meyhofer, and P. Reddy, Quantized Thermal Transport in Single-Atom Junctions, *Science* 355, 1192 (2017).

[8] F. Strigl, C. Espy, M. Bückle, E. Scheer, and T. Pietsch, Emerging Magnetic Order in Platinum Atomic Contacts and Chains, Nat. Commun. 6, (2015).

[9] Y. Chen, X. An, and X. Liao, Mechanical Behaviors of Nanowires, *Applied Physics Reviews* 4, 031104 (2017).

[10] B. A. M. Elsner, S. Müller, S. Bargmann, and J. Weissmüller, Surface Excess Elasticity of Gold: Ab Initio Coefficients and Impact on the Effective Elastic Response of Nanowires, *Acta Materialia* 124, 468 (2017).

[11] F. Xu, Q. Qin, A. Mishra, Y. Gu, and Y. Zhu, Mechanical Properties of ZnO Nanowires under Different Loading Modes, *Nano Res*. 3, 271 (2010).

[12] J. Sun, L. He, Y.-C. Lo, T. Xu, H. Bi, L. Sun, Z. Zhang, S. X. Mao, and J. Li, Liquid-like Pseudoelasticity of Sub-10-Nm Crystalline Silver Particles, *Nature Mater* 13, 1007 (2014).

[13] Z. M. Ao, S. Li, and Q. Jiang, The Determination of Young's Modulus in Noble Metal Nanowires, *Appl. Phys. Lett.* 93, 081905 (2008).

[14] F. Tavazza, S. Barzilai, D. T. Smith, and L. E. Levine, The Increase in Conductance of a Gold Single Atom Chain during Elastic Elongation, *Journal of Applied Physics* 113, 054316 (2013).

[15] Y. Oshima, Y. Kurui, and K. Takayanagi, Controlling Quantized Steps in Conductance of Gold Zigzag Nanowires, *Appl. Phys. Express* 4, 055002 (2011).

[16] J. Paul and S. Narasimhan, Effect of Coordination on Bond Properties: A First Principles Study, *Bull Mater Sci* 31, 569 (2008).

[17] C. Q. Sun, Y. Sun, Y. G. Nie, Y. Wang, J. S. Pan, G. Ouyang, L. K. Pan, and Z. Sun, Coordination-Resolved C−C Bond Length and the C 1s Binding Energy of Carbon Allotropes and the Effective Atomic Coordination of the Few-Layer Graphene, *J. Phys. Chem. C* 113, 16464 (2009).

[18] J. H. Rose, J. Ferrante, and J. R. Smith, Universal Binding Energy Curves for Metals and Bimetallic Interfaces, *Phys. Rev. Lett.* 47, 675 (1981).

[19] E. Yu. Zarechnaya, N. V. Skorodumova, S. I. Simak, B. Johansson, and E. I. Isaev, Theoretical Study of Linear Monoatomic Nanowires, Dimer and Bulk of Cu, Ag, Au, Ni, Pd and Pt, *Computational Materials Science* 43, 522 (2008).

[20] F. Tavazza, L. E. Levine, and A. M. Chaka, Elongation and Breaking Mechanisms of Gold Nanowires under a Wide Range of Tensile Conditions, *Journal of Applied Physics* 106, 043522 (2009).

[21] M. R. Calvo, C. Sabater, W. Dednam, E. B. Lombardi, M. J. Caturla, and C. Untiedt, Influence of Relativistic Effects on the Contact Formation of Transition Metals, *Phys. Rev. Lett*. 120, 076802 (2018).

[22] S. K. Deb Nath and S.-G. Kim, On the Elastic, Elastic-Plastic Properties of Au Nanowires in the Range of Diameter 1-200 Nm, *Journal of Applied Physics* 112,

123522 (2012).

[23] J. Diao, K. Gall, and M. L. Dunn, Surface-Stress-Induced Phase Transformation in Metal Nanowires, *Nature Materials* 2, 5 (2003).

[24] L. G. Zhou and H. Huang, Are Surfaces Elastically Softer or Stiffer?, *Appl. Phys. Lett*. 84, 1940 (2004).

[25] X. X. Yang, J. W. Li, Z. F. Zhou, Y. Wang, L. W. Yang, W. T. Zheng, and C. Q. Sun, Raman Spectroscopic Determination of the Length, Strength, Compressibility, Debye Temperature, Elasticity, and Force Constant of the C–C Bond in Graphene, *Nanoscale* 4, 502 (2012).

[26] H. Petrova, J. Perez-Juste, Z. Zhang, J. Zhang, T. Kosel, and G. V. Hartland, Crystal Structure Dependence of the Elastic Constants of Gold Nanorods, *J. Mater. Chem.* 16, 3957 (2006).

[27] B. Wu, A. Heidelberg, and J. J. Boland, Mechanical Properties of Ultrahigh-Strength Gold Nanowires, *Nat Mater* 4, 525 (2005).

[28] T. Shiota, A. I. Mares, A. M. C. Valkering, T. H. Oosterkamp, and J. M. van Ruitenbeek, Mechanical Properties of Pt Monatomic Chains, *Phys. Rev. B* 77, 125411 (2008).

[29] A. Hasmy, L. Rincon, R. Hernandez, V. Mujica, M. Marquez, and C. Gonzalez, On the Formation of Suspended Noble-Metal Monatomic Chains, *Phys. Rev. B.*

78, 115409 (2008).

[30] F. Tavazza, D. T. Smith, L. E. Levine, J. R. Pratt, and A. M. Chaka, Electron Transport in Gold Nanowires: Stable 1-, 2- and 3-Dimensional Atomic Structures and Noninteger Conduction States, *Phys. Rev. Lett.* 107, 126802 (2011).

[31] T. Kizuka, Y. Takatani, K. Asaka, and R. Yoshizaki, Measurements of the Atomistic Mechanics of Single Crystalline Silicon Wires of Nanometer Width, *Phys. Rev. B* 72, 035333 (2005).

[32] Lu Yang, Song Jun, Huang Jian Yu, and Lou Jun, Fracture of Sub-20nm Ultrathin Gold Nanowires, *Advanced Functional Materials* 21, 3982 (2011).

Chapter 2 Principle for measuring nano-mechanics

Introduction

This chapter describes the measurement principle which is related to this study. In Chapter 2.1, we introduce the basic principle of TEM characterization. In Chapter 2.2, the principle of force measurement are introduced for two AFM methods, contact mode and frequency modulation mode. In Chapter 2.3, the principle of LER, including the oscillation mode and the electrical circuit of LER are introduced.

2.1 Transmission electron microscopy

In this study, a transmission electron microscope (TEM) is used, which is attractive in various fields as an indispensable tool for nanostructure evaluation. Different from optical microscope, electron waves are used as the light source in TEM and magnetic lens are used. A big advantage of TEM is that it can identify the crystalline (amorphous) structure of a material with high spatial resolution on the atomic order because of the short wavelength of the electron wave. For example, evaluation of defect structure at heterojunctions of semiconductors and identification of grain boundary and segregates of metallic materials. The TEM can obtain real space image of the nanomaterial to characteristic its shape information. In addition to obtain a real space information, the crystal structure can be identified by using an electron diffraction pattern. By using Energy Dispersive X-ray Spectroscopy (EDS) and Electron Energy Loss Spectroscopy (EELS) of a specific region of a sample, the chemical composition and electronic state of sample can be analyzed. Another major feature is that it can be performed with spatial resolution. The electron beam irradiate on the thin sample can bring the sample information as transmitted electrons, scattered electrons, or X-rays. Among them, transmission electrons, elastically scattered electrons and secondary electrons provide information on the morphology and atomic structure of the sample. The X-rays and inelastically scattered electrons are used for EDS and EELS analysis, respectively.

Figure 2.1 shows the optical system of the electron microscope. The illumination system is composed of an electron gun and an illumination lens system. The electron gun generates electrons and focuses and accelerates the emitted electrons. Electron sources that generate electrons can be classified into thermionic emission type and field emission type. The thermionic emission type is further classified into tungsten type and LaB_6 type, and the field emission type is classified into Schottky type and cold cathode field emission type. In general, the brightness increases in the order of tungsten type, LaB_6 type, Schottky type, and cold cathode field emission type, and the electron energy width and beam diameter decrease. The electron beam used in TEM is generally accelerated with an accelerating voltage of tens to hundreds of kV. On the other hand, the rest energy of electrons is about 511 keV, so the electron beam used in TEM needs to be treated in consideration of the relativistic effect. The advantage of microscopy using an electron beam is that it has a wavelength (about 0.025Å for 200 kV) sufficiently smaller than that of atoms (lattice spacing), but because it is a charged particle, it is easy to form an image with an electric or magnetic field lens.

The electron beam emitted from the electron gun is focused by the condenser lens and irradiate on the sample. The electrons transmitted through the sample or scattered by the sample are focused by the objective lens, and an electron diffraction pattern is formed on the back focal plane and an image of the sample projected on the image plane.

When the image plane of the objective lens is magnified with an intermediate lens and a projection lens as shown in (a), a microscope image is obtained like an observation plane (fluorescent plate or CCD camera), if the back focal plane of the objective lens is enlarged (as shown in (b)), an electron diffraction pattern is obtained. In this study, the structure of nanocontacts was evaluated by recording a microscope image with a CCD camera.

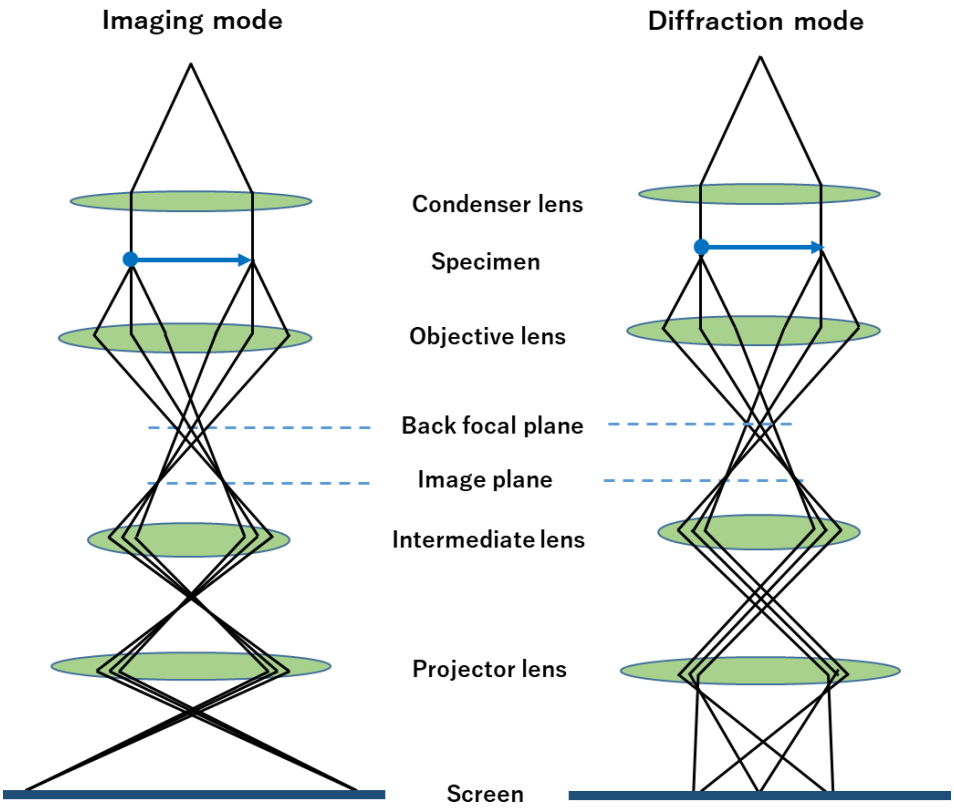

Figure 2.1 (a) A microscope image can be obtained by enlarging the image plane of the objective lens. (b) A diffraction pattern can be obtained by enlarging the posterior focal plane of the objective lens.

2.2 Force measurement by atomic force microscopy (AFM) method

2.2.1 Contact mode AFM

Atomic force microscopy (AFM) is one of the most important equipment to characteristic the materials. Usually it can be categorized in contact mode and non-contact mode. The contact mode AFM has a mechanism that detects the amount of deformation of a cantilever beam (which is deformed by the force acting between it and the sample) with a probe attached to the free end. At present, it is common to use the optical lever method for detecting the amount of bending. The force acting between the probe and the sample is commonly referred to as the atomic force, hence the name Atomic Force Microscope (AFM) [1].

As shown in Figure 2.2, when the distance between two atoms is long, the Van der Waals (VdW) force acts as an attractive force, and when they approach with each other, the chemical bond force acts as a stronger attractive force. In addition, when both electrons are so close to each other that they overlap, a strong repulsive force acts due to Pauli exclusion principle. When atoms are closer to each other than the distance at which the chemical bond force works, the atomic force changes significantly with the change in distance. In contact mode AFM, this is used in the repulsive force region, and the surface is scanned while searching for the sample position with respect to the probe so that the atomic force between the probe tip and the sample surface becomes constant,

resulting in high resolution in the height direction. (Even if there is some error in the force measurement, the corresponding distance error is small).

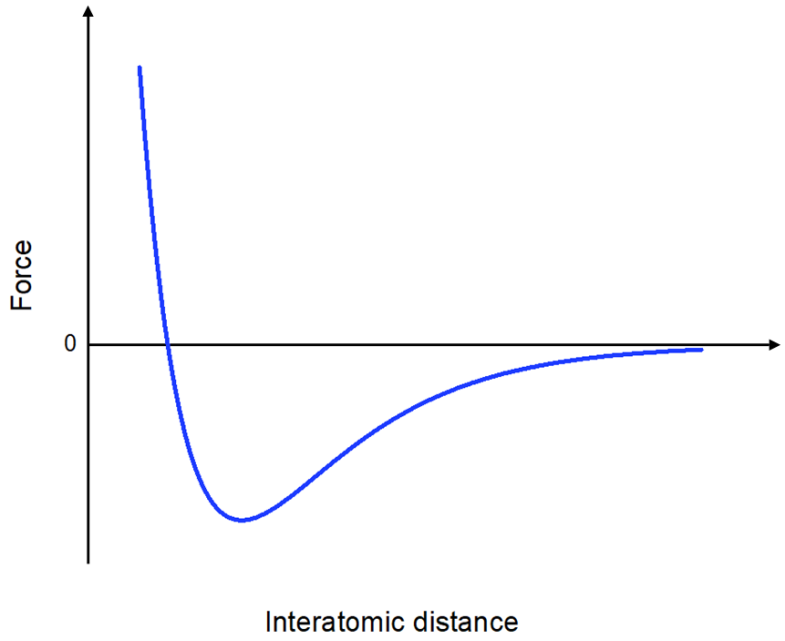

Figure 2.2 The force acting between two atoms as a function of interatomic distance

A schematic diagram of the typical AFM measurement system is shown in Figure 2.3. The magnitude of the force acting between the probe and the sample corresponds to the amount of cantilever deformation according to Hooke's law. By moving the sample in the z direction using a piezo and searching for the position where the cantilever has an arbitrary amount of bending at each point on the x-y plane, the surface structure can be visualized. A laser and a split photodiode are used to determine the amount of cantilever deformation. One or both sides of the cantilever are usually coated

with gold to form a small mirror. When the cantilever is irradiated with a laser, the direction of the reflected light changes depending on the amount of deformation. By giving feedback to the sample position z with reference to the photodiode reflected light position at an arbitrary amount of deformation, the cantilever searches for z at which the amount of deformation becomes arbitrary.

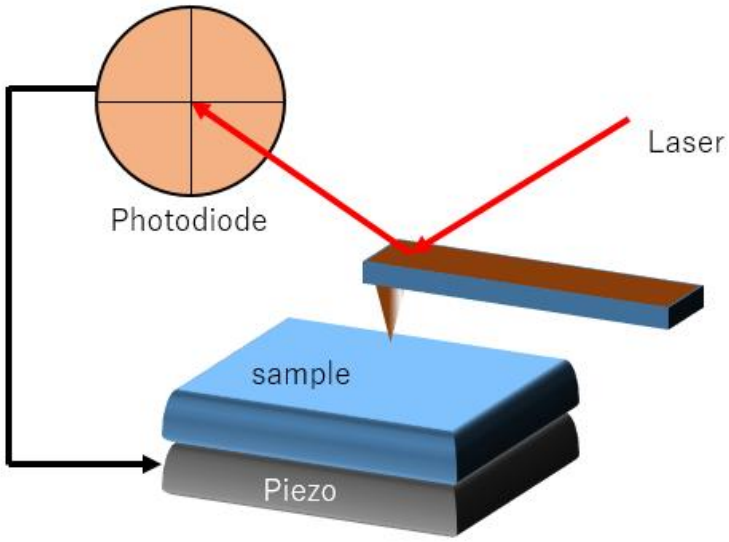

Figure 2.3 Schematic diagram of the AFM measurement

2.2.2 Frequency modulation-AFM

Frequency modulation-AFM (FM-AFM) is a method to detect the interaction between the sensor and the sample by using the resonance frequency of the sensor. In general, the measurement is performed with the probe and the sample separated, so this

is also called non-contact mode AFM which is different to the contact mode described above. FM-AFM has made progress since it achieved the acquisition of atomic resolution images in an ultra-high vacuum environment in 1995, and is now being applied in both atmospheric and liquid environments [2]. Initially, a cantilever was used as the sensor, and recently a crystal oscillator is used in addition to this.

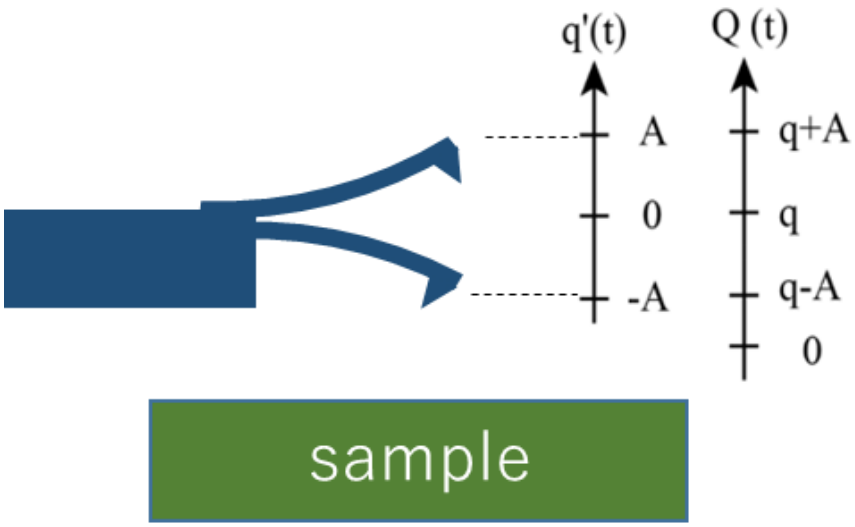

Figure 2.4 Schematic diagram of the oscillation of the sensor

When measuring the force response by FM-AFM, the sample is close to the sensor which probe is oscillating with amplitude A, and the $\mu*$ and k is the effective mass and spring constant of the sensor, respectively. If we assume the oscillation center position of the oscillating probe is q and the probe position is $q'(t)$ if the oscillation center is assumed to be the origin position, the probe position based on the sample

surface is $Q(t) = q'(t) + q$ (Fig. 2.4). If the interaction potential between the probe and the sample is $V_{ts}(Q)$, the equation of motion of the sensor is:

$$\mu^* \frac{d^2q'}{dt^2} = -kq' + F_{ts}(Q) \tag{2.1}$$

Here, $F_{ts}(Q) \equiv \frac{dV_{ts}}{dQ}\Big|_Q$, and $\frac{d^2Q}{dt^2} = \frac{d^2q'}{dt^2}$ is used. Simple oscillation in the absence of interaction V_{ts}

$$q'(t) \equiv A\cos(2\pi f_0 t) \tag{2.2}$$

Then, the frequency at this time is the natural frequency (resonance frequency) of the sensor.

$$f_0 = \frac{1}{2\pi}\sqrt{\frac{k}{\mu^*}} \tag{2.3}$$

In the region $-A \le q' \le A$,When the k_{ts} is exist as $\frac{dF_{ts}}{dq'} = -\frac{d^2V_{ts}}{dq'^2} = -k_{ts}$, the resonance frequency of the sensor is:

$$\Delta f = f - f_0 = \frac{1}{2\pi}\sqrt{\frac{k+k_{ts}}{\mu^*}} \tag{2.4}$$

When $k_{ts} \ll k$, the frequency shift becomes:

$$\Delta f = f_0\left(1 + \frac{k_{ts}}{k}\right)^{\frac{1}{2}} - f_0$$

$$\cong \frac{k_{ts}}{2k} f_0 \tag{2.5}$$

Therefore, the equivalent spring constant k_{ts} which corresponds to the gradient of the force acting between the probe and the sample, can be obtained from the resonance frequency shift Δf of the sensor.

In the case of contact mode, the force applying to the nanocontact can be obtained

directly, while in the case of non-contact mode, the spring constant can be obtained. They have advantages and disadvantages [1]. For example, if the force can be measured directly, the yield or breaking stress of nanocontacts or atomic wires can be measured. That is, it is convenient to see the characteristics of plastic deformation. However, in order to observe the elastic deformation region, the strain of the contact is demanded to be evaluated, which is difficult because of nanoscale size. On the other hand, if the spring constant and elastic constant can be directly measured, it is easy to evaluate the elastic response. However, in order to know the force applied to the contact point, the spatial distribution of the elastic constant (to integrate into the dimension of the force) and the value corresponding to the constant of integration are required [3].

For the above reasons, the force measurement by FM method is used in this study instead of the contact mode since we focus on the elastic properties of the materials. For the crystal unit, a Length-extension resonator, which has a spring constant larger than that of the tuning fork type, is used.

2.3 Length-extension resonator (LER) as a force sensor

In this study, a length extension resonator (LER) (Fig. 2.5) is used as the force sensor by FM method. One of the reasons for choosing this sensor is due to its large spring constant [4,5]. The spring constant of a general crystal oscillator is about 10^3

N/m, the spring constant of LER is as large as 10^5 N/m, which is more suitable for force measurement in the coupling region. This high rigidity is also advantageous in terms of TEM observation. Because the higher the rigidity, the easier it is to reduce the sensor amplitude to measure the elastic response, which enables us to obtain the atomic resolved TEM images without obvious blur. The LER used in this study is a product of STATEK (3EXW-1073), and the spring constant per rod is approximately 9.2×10^5 N/m and the resonance frequency is ~1 MHz.

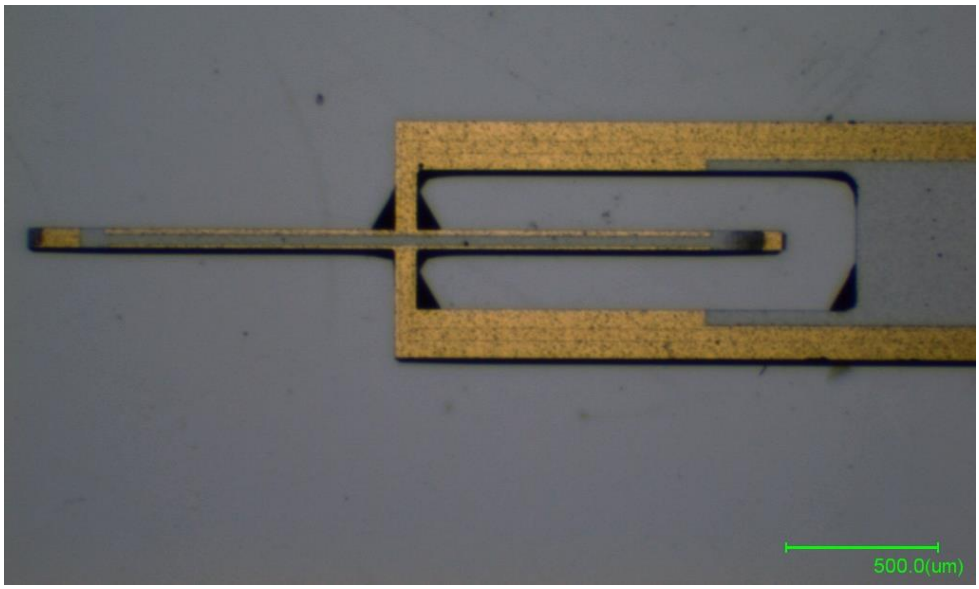

Figure 2.5 Photograph of the LER.

2.3.1 Oscillation of LER

The LER is made of quartz crystal. Since the crystal is spontaneously polarized, it

exhibits a (reverse) piezoelectric effect. Therefore, in addition to mechanical excitation, electrical excitation by applying an AC voltage is possible. It also means that oscillation can be detected electrically. Gold electrodes vapor-deposited on the LER are used for electrical excitation and oscillation detection. Figure 2.6 shows the arrangement of the electrodes of the LER. There are two types of electrodes, shown in red and blue, which are not electrically coupled. In addition, these are vapor-deposited on both side surfaces of the rod. For electrical excitation, a voltage is applied to only one of the electrodes. When an AC voltage is applied, stress is generated in the axial direction of the rod due to the inverse piezoelectric effect, and the rod expands and contracts repeatedly (Fig. 2.6). Since an induced charge is generated on the side surface of the rod due to the deformation of the rod, oscillation can be detected by the induced charge.

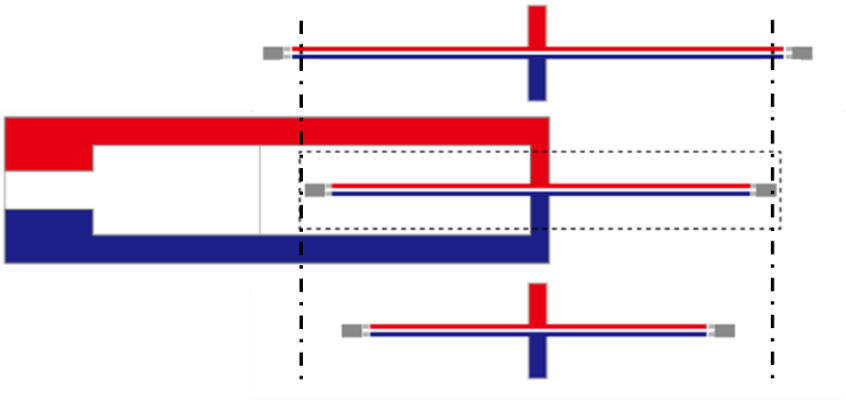

Figure 2.6 Schematic diagram of the electrode and oscillation of LER.

In the LER of Figure 2.7, the two beams are fixed to the substrate with a spring constant k_c. We assume that qc is the center of the displacement of the beam (point c), q_1 and q_2 are the displacements of two beams (right and left-side) from their natural length positions, respectively, and the spring constant and effective mass is k_{LER}, μ^* for each beam, respectively. When the external force acting on the probe attached to the right-side beam, the gradient of force (equivalent spring constant) is k_{ts}, the equation of motion can be written as follows.

$$\begin{cases} \mu^* \frac{\partial^2 q_1}{\partial t^2} = -k_{ts} q_1 - k_{LER}(q_1 - q_C) \\ \mu^* \frac{\partial^2 q_2}{\partial t^2} = -k_{LER}(q_2 - q_C) \end{cases} \tag{2.6}$$

Here, the following relationship can be obtained from the balance of the point c as shown in Fig. 2.7.

$$-k_C q_C = -k_{LER}(q_1 - q_C) - k_{LER}(q_2 - q_C)$$

$$q_C = \frac{q_1 - q_2}{2 + \frac{k_C}{k_{LER}}} \tag{2.7}$$

If we define κ as follows.

$$\kappa = \frac{1}{2 + \frac{k_C}{k_{LER}}} \tag{2.8}$$

$\omega_0^2 = \frac{k_{LER}}{\mu^*}$ can be obtained and the equation (2.6) can be rewritten as follows:

$$\begin{cases} \frac{\partial^2 q_1}{\partial t^2} = -\omega_0^2 \left(\frac{k_{ts}}{k_{LER}} + 1 - \kappa \right) q_1 + \omega_0^2 \kappa q_2 \\ \frac{\partial^2 q_2}{\partial t^2} = \omega_0^2 \kappa q_1 - \omega_0^2 (1 - \kappa) q_2 \end{cases} \tag{2.9}$$

Here we define,

$$\boldsymbol{M} \equiv \omega_0^2 \begin{pmatrix} \frac{k_{ts}}{k_{LER}} + 1 - \kappa & -\kappa \\ -\kappa & 1 - \kappa \end{pmatrix} \tag{2.10}$$

$$\boldsymbol{Q} \equiv \begin{pmatrix} q_1 \\ q_2 \end{pmatrix} \tag{2.11}$$

The equation (2.14) can be expressed as a matrix as follows.

$$\frac{\partial^2}{\partial t^2}\boldsymbol{Q} = -\boldsymbol{M}\boldsymbol{Q} \tag{2.12}$$

Assuming that the displacement of the beam is simple oscillation, which is defined as $q_i = A\cos(\omega_i t - \phi_i)$ and we assume the frequencies of two beams are the same $-\omega = \omega_1 = \omega_2$. Then

$$\frac{\partial^2}{\partial t^2}\boldsymbol{Q} = -\omega^2\boldsymbol{Q} = -\boldsymbol{M}\boldsymbol{Q} \tag{2.13}$$

Therefore, ω^2 is the eigenvalue of $\boldsymbol{M}$ with $\boldsymbol{Q}$ as the eigenvector. From det $\det(\boldsymbol{M} - \omega^2\boldsymbol{E}) = 0$, we obtain

$$\begin{vmatrix} \frac{k_{ts}}{k_{LER}} + 1 - \kappa - \frac{\omega^2}{\omega_0^2} & -\kappa \\ -\kappa & 1 - \kappa - \frac{\omega^2}{\omega_0^2} \end{vmatrix} = 0 \tag{2.14}$$

$$\omega_{\pm}^2 = \omega_0^2\left\{\left(\frac{k_{ts}}{k_{LER}} + 1 - \kappa\right) \pm \sqrt{(\frac{k_{ts}}{k_{LER}})^2 + \kappa^2}\right\} \tag{2.15}$$

The frequencies indicated by the plus and minus signs correspond to the resonant oscillate in opposite phase and in phase, respectively. In the limit of $k_{ts} \to 0$, $\omega_+^2 = \omega_0^2$, $\omega_-^2 = (1 - 2\kappa)\omega_0^2$. κ including the spring constant k_c of the beams fixing part appears only in the solution of the same phase. This is because when the beam vibrates in the opposite phase, the force applied to the fixing part is canceled. Since the oscillation of the opposite phase is used in this study, ω_+^2 is expressed as ω^2 and will

be discussed below. When the spring constant of the beam is sufficiently larger than the spring constant of the external force ($k_{LER} \gg k_{ts}$), we can obtain:

$$\omega^2 \approx \omega_0^2 \left\{ \left(\frac{k_{ts}}{2k_{LER}} + 1 - \kappa \right) + \kappa \right\} = \omega_0^2 \left(\frac{k_{ts}}{2k_{LER}} + 1 \right)$$

$$\omega \approx \omega_0 \left(\frac{k_{ts}}{4k_{LER}} + 1 \right) \tag{2.16}$$

Therefore, the relationship between the equivalent spring constant due to the loading force and the frequency shift of LER is

$$\Delta f = \frac{1}{2\pi} (\omega - \omega_0)$$

$$= \frac{k_{ts}}{4k_{LER}} f_0 \tag{2.17}$$

As compared with the equation (2.5), the effective spring constant of the LER is found to be twice the spring constant of one beam.

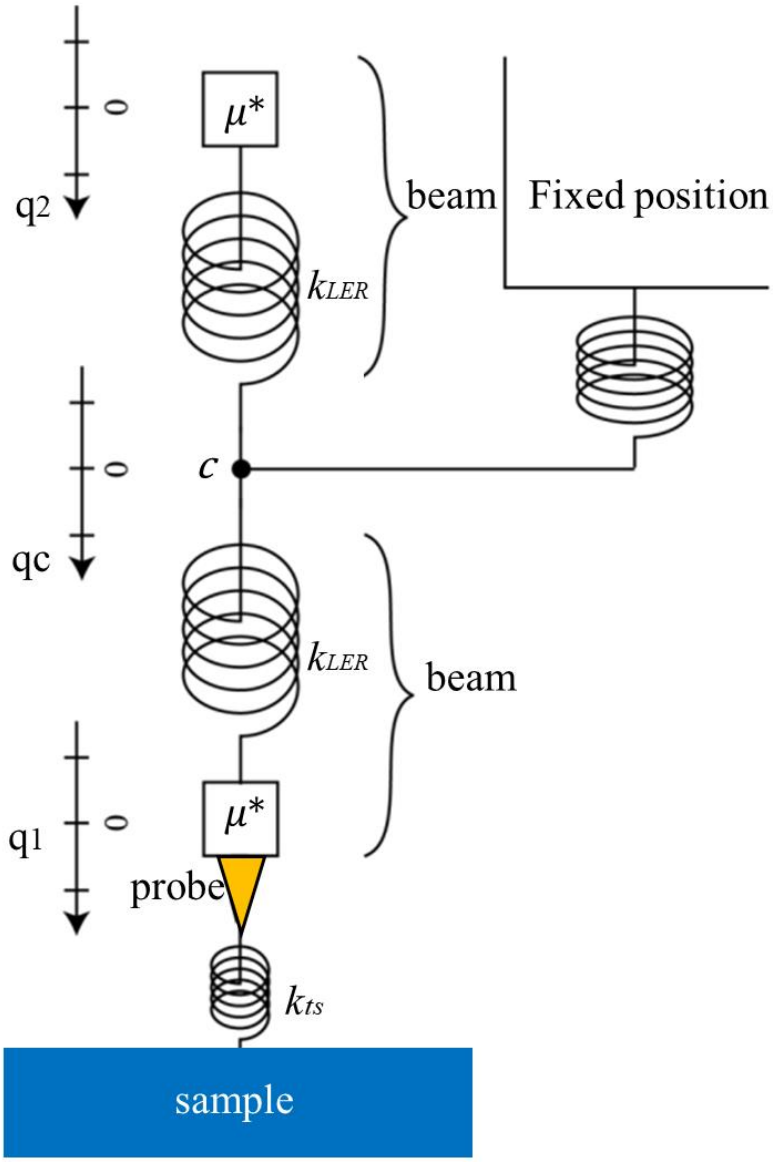

Figure 2.7 Model of the oscillation of the LER.

2.3.2 Equivalent electrical circuit of LER

The circuit characteristics of LER can be thought of as an LCR circuit. The impedance of a circuit including a capacitor and an inductor takes an extreme value when the imaginary part of the impedance becomes 0. We consider two different circuits that one capacitor *C*, one coil *L*, and one resistor *R* are connected in series and

in parallel. In the case of series connection, impedance *Z* is described by,

$$Z = R + \frac{1}{j\omega C} + j\omega L = R + j(-\frac{1}{\omega C} + \omega L) \tag{2.18}$$

When the alternative voltage of the frequency, $\omega = \frac{1}{\sqrt{CL}}$, is generated, the imaginary part of the impedance, Z, becomes 0 and the impedance takes a minimum value (series resonance). That is, the potential difference between both ends of the circuit becomes the minimum, and the current becomes the maximum. While, in the case of series connection, admittance *Y* is described by,

$$Y = \frac{1}{R} + j\omega \mathrm{C} + \frac{1}{j\omega \mathrm{L}} = \frac{1}{R} + j(\omega C - \frac{1}{\omega \mathrm{L}}) \tag{2.19}$$

In the case of the frequency, $\omega = \frac{1}{\sqrt{CL}}$, the imaginary part of the impedance, Z, becomes 0 and the admittance takes a minimum value (parallel resonance). At this time, the impedance becomes maximum. That is, the potential difference between both ends of the circuit becomes maximum, and the current becomes minimum. At this time, it can be seen that the impedance of the closed path including the capacitor and the coil becomes the minimum. At the time of parallel resonance, the loop current in the circuit becomes maximum.

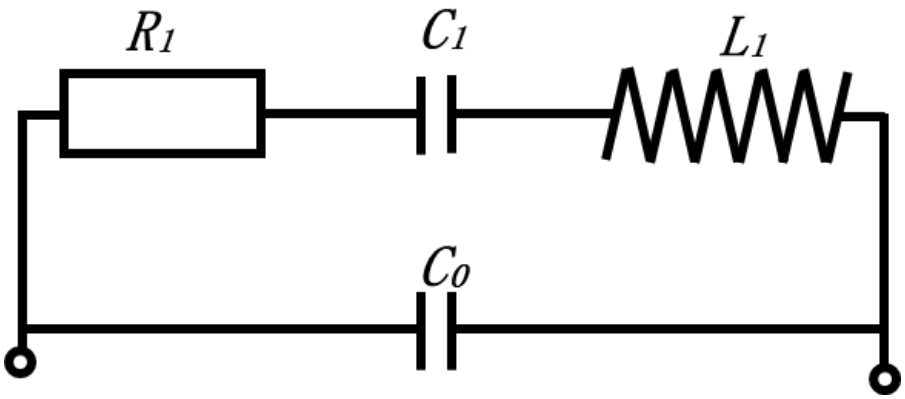

Figure 2.8 The equivalent electrical circuit of the LER.

The LER can be represented by the equivalent circuit shown in Fig. 2.8. R_1 is the equivalent series resistance, C_1 is the equivalent series capacitance, L_1 is the equivalent series inductance, and C_0 is the floating capacitance. The reciprocal of C_1 corresponds to the oscillator spring constant, and L_1 corresponds to the effective mass of the oscillator. The impedance Z_c of the LER is represented by the following.

$$Z_c = \frac{\left(R+\frac{1}{j\omega C_1}+j\omega L\right)\frac{1}{j\omega C_0}}{R+\frac{1}{j\omega C_1}+j\omega L+\frac{1}{j\omega C_0}} \tag{2.20}$$

This imaginary part of the impedance Z_c can be written as follows.

$$\mathrm{Im}[Z_c] = \frac{\left\{\left(\frac{L}{C_0}-\frac{1}{\omega^2 C_0 C_1}\right)\left(\omega L-\frac{1}{\omega C_1}-\frac{1}{\omega C_0}\right)-\frac{R^2}{\omega C_0}\right\}}{R^2+\left(\omega L-\frac{1}{\omega C_1}-\frac{1}{\omega C_0}\right)^2} \tag{2.21}$$

When $\omega C_0 \gg R^2$, if we can find a frequency $f = 2\pi\omega$ that make the imaginary part becomes 0,

$$\left(\frac{L}{C_0}-\frac{1}{\omega^2 C_0 C_1}\right)\left(\omega L-\frac{1}{\omega C_1}-\frac{1}{\omega C_0}\right) = 0 \tag{2.22}$$

$$f_r = \frac{1}{2\pi\sqrt{L_1 C_1}} \tag{2.23}$$

$$f_a = \frac{1}{2\pi\sqrt{L_1\frac{C_0C_1}{C_0+C_1}}} \tag{2.24}$$

These are the series resonance frequency (f_r) and the parallel resonance frequency (f_a), respectively. At these frequencies, the current that passes through the circuit (series resonance) or the current that loops through the circuit (parallel resonance) are maximized. Where f_a is

$$f_a = \frac{1}{2\pi\sqrt{L_1C_1}}\sqrt{\frac{C_0+C_1}{C_0}} \approx \frac{1}{2\pi\sqrt{L_1C_1}}\left(1+\frac{C_1}{2C_0}\right) = f_r\left(1+\frac{C_1}{2C_0}\right) \tag{2.25}$$

In general, $\frac{C_1}{C_0}$ is about $\frac{1}{200}$ to $\frac{1}{400}$, so f_a is slightly higher than f_r. The imaginary component of Z (reactance of the LER) is inductive only with respect to the frequency between f_r and f_a. Therefore, the input/output phase difference changes significantly near f_r or f_a. This property is used for accurately generating the oscillation with the resonant frequency. Simply, the transmitter can generate oscillate with the resonate frequency which is determined by using the resonant circuit of using the feedback. The values of the capacitors and coils required for this resonance circuit fluctuate depending on the temperature, so the resonance frequency changes depending on the temperature. Compared with such simple resonant circuit, LER is very stable. By replacing the resonance circuit itself with a LER or replacing the coil part with a LER (because the crystal oscillator works as a coil only in a limited frequency range), we can use LER as a stable oscillator.

2.4 Conclusion

In this chapter, we have demonstrated the main theories which will be used in this thesis for better understanding the result obtained from our experiment. Firstly, the principle of the transmission electron microscopy is introduced, including the basic composition of TEM and the imaging principles. Then the principle of the force measurement by AFM is introduced. We introduced the mechanism of contact mode AFM and the FM-AFM, and the relationship between the measured force constant and frequency shift is discussed. Finally, the force senor LER is introduced by explain its oscillation principle and equivalent electrical circuit.

References

[1] F. J. Giessibl, Advances in Atomic Force Microscopy, *Reviews of Modern Physics* 75, 949 (2003).

[2] F. J. Giessibl, Atomic Resolution of the Silicon (111)-(7×7) Surface by Atomic Force Microscopy, *Science* 267, 68 (1995).

[3] F. J. Giessibl, Forces and Frequency Shifts in Atomic-Resolution Dynamic-Force Microscopy, *Phys. Rev. B* 56, 16010 (1997).

[4] T. An, T. Eguchi, K. Akiyama, and Y. Hasegawa, Atomically-Resolved Imaging by Frequency-Modulation Atomic Force Microscopy Using a Quartz Length-Extension Resonator, *Appl. Phys. Lett*. 87, 133114 (2005).

[5] F. J. Giessibl, F. Pielmeier, T. Eguchi, T. An, and Y. Hasegawa, Comparison of Force Sensors for Atomic Force Microscopy Based on Quartz Tuning Forks and Length-Extensional Resonators, *Phys. Rev. B* 84, 125409 (2011).

Chapter 3 Experiment setup and sample preparation

Introduction

This chapter introduced the main experiment setup used in this thesis. In Chapter 3.1, we introduce the TEM machine used in this study and its advantages. In Chapter 3.2, we show the detail design of our developed TEM holder. In Chapter 3.3, we explain how to set the LER onto the PEEK board which is installed in the TEM holder. In Chapter 3.4 and 3.5, we introduce the equipment and measurement method for the mechanical measurement system and the conduction measurement system. In Chapter 3.6, the properties of LER are carefully calibrated.

3.1 Ultra-high vacuum TEM (UHV-TEM)

In the case of a general TEM, a phenomenon occurs in which contaminations may adhere to the sample surface due to electron beam irradiation during observation. It is thought that the hydrocarbon-based residual gas molecules in the sample chamber are dissociated and evaporated by electron beam irradiation and they are redeposited on the sample surface to form the contamination layer. It deteriorates the signal-to –noise ratio in the TEM image to hinder the structural information. The adverse effect on physical property measurement is even greater. In particular, for the smaller the measurement target due to its larger surface-to-volume ratio, the properties of the surface are easily affected by such contaminations especially for the mechanical properties. So, there is a possibility that the characteristics derived from contamination may be measured. Since UHV-TEM can maintain ultra-high vacuum (UHV) condition in the sample chamber on the order of 10^{-7} Pa. In such UHV condition, the evaporated molests consisting of carbon atoms are hardly redeposited on the surface and the contamination layer can be reduced to make a sample surface clean.

In this study, we used the UHV-TEM (JEM2000FXVB) manufactured by JEOL Ltd. as shown in Figure 3.1. The sample chamber of the TEM is evacuated by an ion pump and a titanium sublimation pump, and the maximum ultimate vacuum of the sample chamber reaches the order of 10^{-7} Pa. The spherical aberration of the objective

lens is 0.705 mm, and the point resolution of the high-resolution image is 0.21 nm. The electron gun is a field emission type. The accelerating voltage during structural observation is 200 kV, the measurement environment is room temperature (300 K), and the ultra-high vacuum (7×10^{-7} Pa). Schematic of the measurement system is shown in figure 3.2. The nanocontacts were fabricated in the TEM chamber, and the electrical conductance of the Pt NC was determined by applying a bias voltage of 12.2 mV to the nanocontacts and monitoring the voltage signal after conversion with a current amplifier at a sampling rate of 2.4 kHz. The LER was excited so as to oscillate at its resonance frequency by applying a sinusoidal voltage to one electrode of the LER. The electric charge that was induced sinusoidally by deformation of the quartz crystal due to the piezoelectric effect was monitored through the other electrode of the LER. The induced charge was converted to a voltage signal (hereafter, referred to as the output signal) using a charge amplifier (HQA-15M-10T, FEMTO Messtechnik GmbH, conversion ratio of 10 V/pC). The shift of resonance frequency (Δf) of the LER was determined employing a phase locked loop (PLL) (OC4, SPECS Zurich GmbH). These signals were also acquired at a sampling rate of 2.4 kHz.

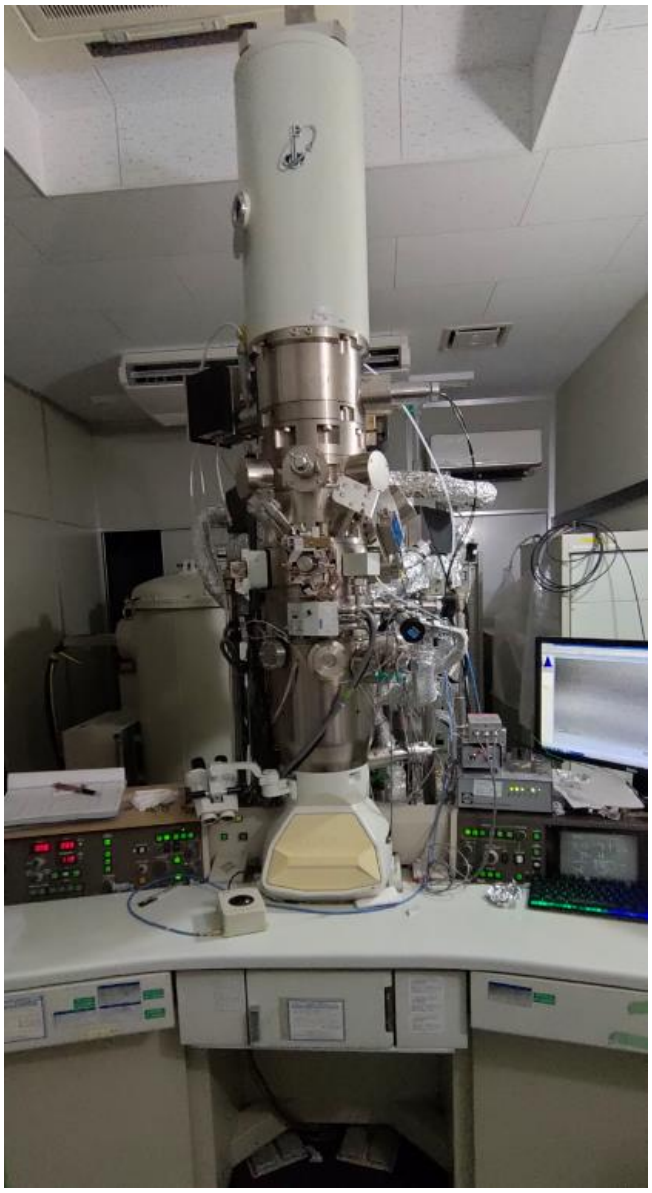

Figure 3.1 Photograph of UHV-TEM.

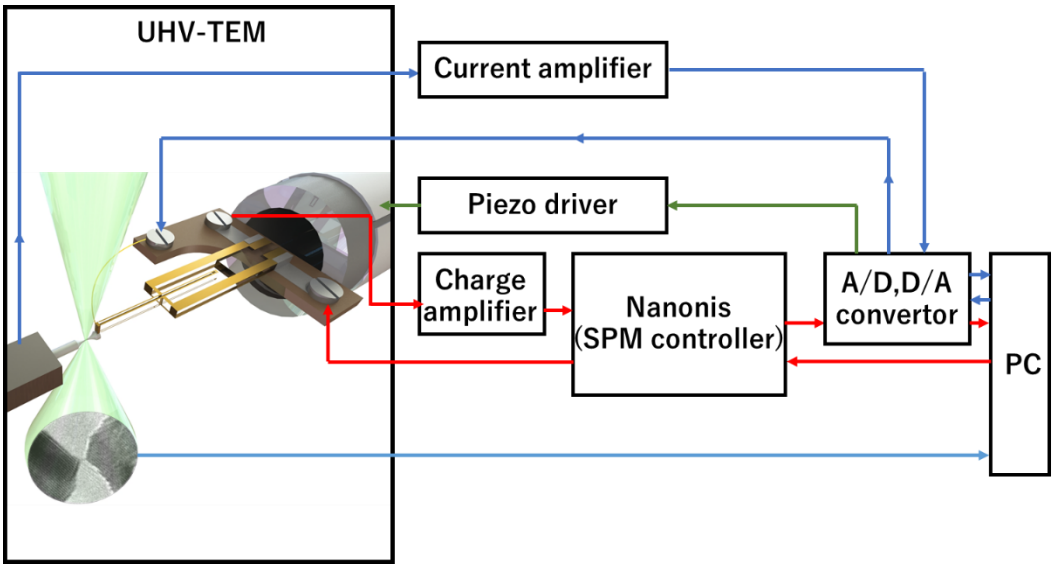

Figure 3.2 Schematic of the measurement system

3.2 Development of TEM holder with LER as force sensor

In this study, we developed a specific TEM sample holder (TEM-AFM holder) to measure the spring constant and conductance of metal nanocontacts and observe the structure at the same time. Figure 3.3 (a) shows a photo of our developed TEM holder and figure 3.3 (b, c) shows the design of the head part of our developed TEM holder schematically. The nanocontacts can be fabricated by making a contact with two metal wires with sharp edges, one of which is attached to a copper plate acting as a counter electrode and another one of which is attached to the edge of the LER with silver paste. The position of the latter wire can be controlled by a coarse motion and a fine motion system. An ultrasonic motor (TULA50, Technohands) is used for the coarse motion and the fine adjustments is realized by a tube piezo. The fine adjustment ranges in x, y and

z direction is about $\pm 1\mu$m (figure 3.3 b). The movement range of coarse motion in y direction is 5mm. The movement resolution of the coarse motion is about 50nm and resolution of the fine motion is about 10 pm.

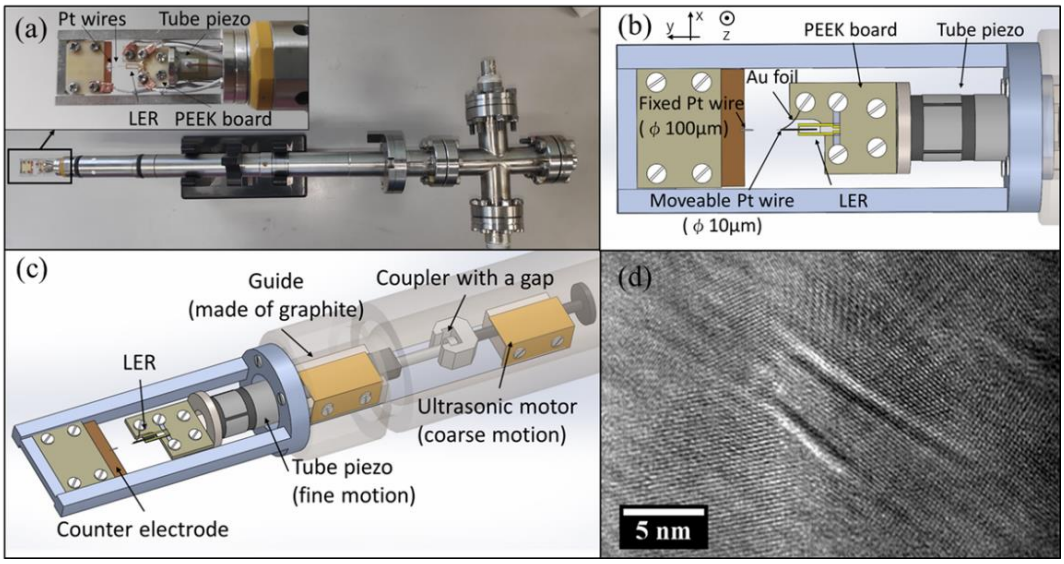

Figure 3.3 (a) Photograph of the developed TEM holder. Inset is an enlargement of the sample stage of the TEM holder. (b) an illustration of the sample stage in the TEM holder, (c) an illustration of the motion system of the TEM holder, and (d) an atomic resolution HR-TEM image of a Pt crystal captured using this TEM holder.

In our previously developed in-situ TEM holder, the coarse motion of the electrode was controlled by a micrometer attached to the tail part of the holder via a long rod which was necessary to transfer the linear motion. However, the long rod connected between a motor or micrometer reduced the mechanical stability of the moving

electrode because of the oscillation and drift. Instead, in our developed TEM holder, an ultrasonic motor, which is used as coarse motion, and also the guide, which is introduced to increase the rigidity of the moving part, keep the mechanical stability of the moving electrode as shown in figure 3.3(c). The minimum movement step of the ultrasonic motor can be controlled at several nanometer scale. A fine motion of piezo tube is connected to the electrode (fig 1(a, c)). Between the piezo tube and ultrasonic motor, a guide made of graphite is incorporated for improvement of the mechanical stability. The performance of these devices are shown in table 1. The stability of our developed holder is quite high so that we can obtain the atomic resolution TEM image as shown in figure 3.3 (d)

The movement of the ultrasonic motor is controlled by applying a voltage in rectangular wave on it. The movement of the motor can be adjusting by the parameters such as the voltage, duty of the applied voltages. The basic principle of the movement of the ultrasonic motor is shown in figure 3.4. The movement body is connecting to the rod made by the carbon fiber. There is a piezo element at the end of the rod. When the voltage is applied, the piezo element first deforms and the rod with the movement body is moved towards the direction in which the piezoelectric element bulges. After the voltage is removed, the piezo element and the rod back to their original positon and the movement body is left to the positon after the movement. So, the movement body can

be moved by applying a rectangular wave.

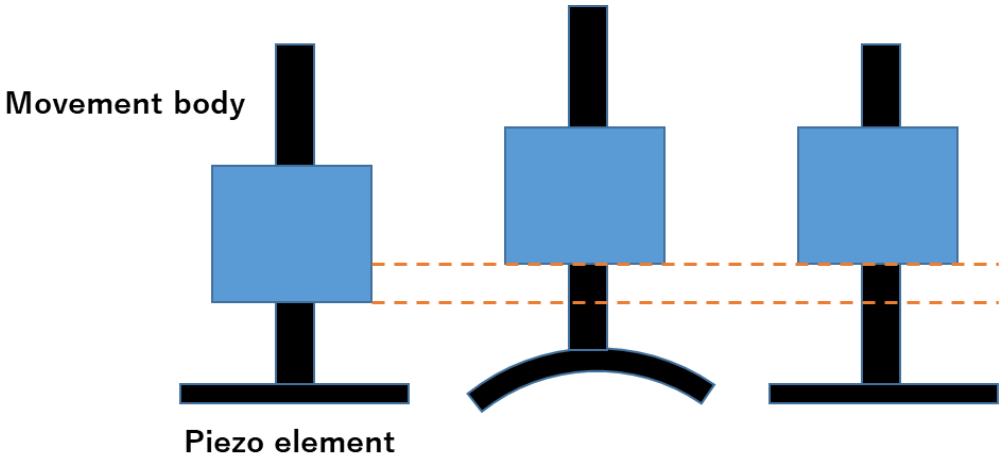

Figure 3.4 Mechanism of the movement for the ultrasonic motor

Accurate position control on the order of sub-nm is required to make, maintain and observe the nanocontacts. The tube piezo of 3-axis control is used to control the position of the LER sensor, which can be moved by 2.67 nm/V. The displacement of the tube piezo is controlled by the voltage applied on it. Figure 3.5 shows a photo of the piezo driver (MESS-TEK M-2680). Table 3.1 shows the performance of the motion system.

Table 3.1 performance of the motion system.

Type of Motion	Mechanism	Movement range	Movement resolution
Coarse	Ultrasonic motor	5mm (y direction)	~50nm
Fine	Piezo tube	1um in x-z plane and y direction	<1nm

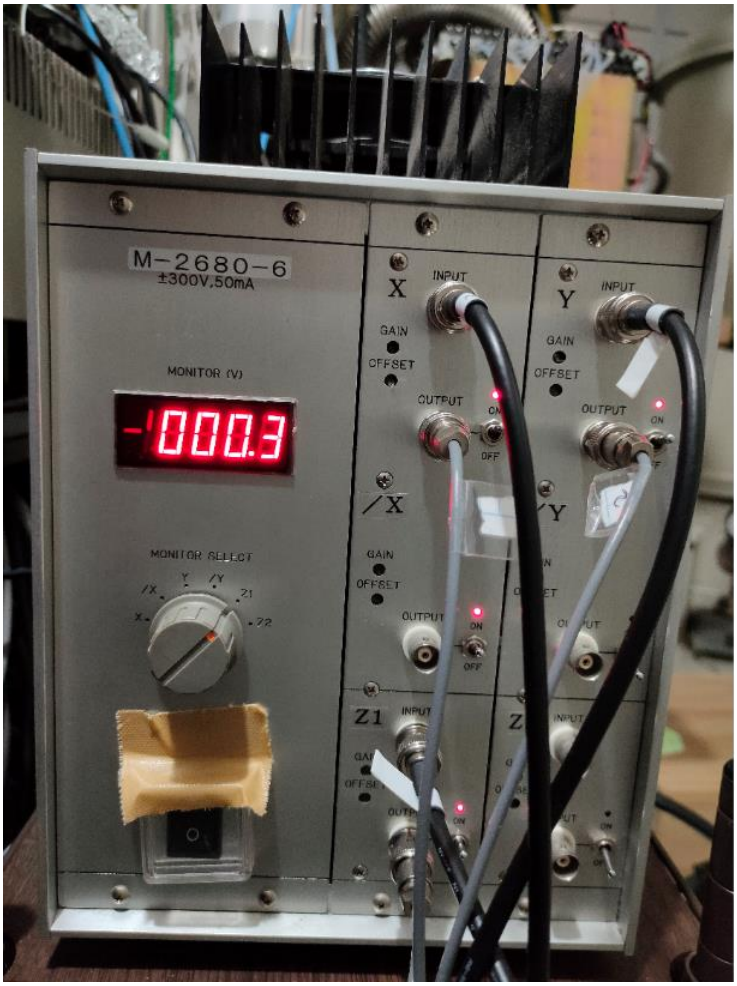

Figure 3.5 Photo of the piezo driver

3.3 Sample preparation

LER (3EXW-1073, STATEK) is glued onto the polyether ether ketone (PEEK) board with insulating epoxy, and the PEEK board is connected to the sample stage which can be moved by the tube piezo. The two electrodes of LER are electrically connected to two coaxial cables, one is for electrical excitation to enable LER oscillation and another is for measuring the signal from the LER. An Au foil ribbon (thickness: 1 μm and width: 20 μm) is glued to the metal wire placed on the edge of the LER by Ag paste to measure the conductance of the metal nanocontact. The metal wire is electrically isolated from two LER electrodes. The detail for prepareing the LER on PEEK board is present below.

The LER is fixed on a PEEK board and the electrical connection should be made to excited the LER and obtain the signal. Figure 3.6 shows the outline of this process. The peek substrate has been pre-drilled with five holes. The lower two holes is for screwing the board to the stage driven by piezo, the center two holes are for screwing the wiring for mechanical measurement, and the upper one hole for screwing the wiring for conduction measurement. Firstly, the burrs created during the drilling process are removed by the sandpaper. After polishing, the substrate is ultrasonically cleaned with acetone (Fig. 3.6. 1). Next, the surface near the holes for conduction measurement is covered with conductive resin (Fig. 3.6. 2), Epoxy Technology EPO-TEK H20E is used

as the conductive thermosetting resin (silver particle-containing, conductive). Then the LER is fixed on the PEEK board using thermosetting resin (insulation), the Epoxy Technology EPO-TEK H65-175MP is used as the thermosetting resin (insulation). After adjusting the angle so that the LER oscillator is parallel to the axis of the TEM holder, heat it in a furnace to cure the resin (Fig. 3.6. 3). Next, a wiring for mechanical measurement is prepared on the substrate surface using a conductive resin (Fig. 3.6. 4). After the curing of the conductive resin, a small amount of conductive resin is put on the edge of LER to fix and connect the electrical wire and the sample (Fig. 3.6. 5). In order to reduce the effect on the oscillator, the amount of resin used for adhesion is reduced as much as possible. After putting the conductive resin, one side of a gold foil ribbon (~20 μm in width and 1 μm in thickness) is attached to the resin, the other side of the ribbon is put on to the PEEK board where the cured conductive resin is glued (Fig. 3.6. 6). Then it is cured in a furnace. Next, conductive resins is used to fix and make electrical connection between the conductive resin on PEEK board and the gold foil ribbon (Fig. 3.6. 7). After the gold foil ribbon is fixed between the LER and the PEEK board, a short metal wire, which have been cut with a sharp edge, is glued on the edge of LER with the conductive resin to make an electrical connection with the gold foil ribbon (Fig. 3.6. 8).

The steps 4-8 are quite difficult to manipulate by hand, which is difficult to control

the amount of resin for adhesion on the LER thus reduce its Q factor. In addition, since the scale of the LER is too small, it is difficult to transfer the gold foil ribbon and the metal wires to the LER, which is fragile. We used a micro manipulator (Axis Pro, Micro Support Co. ltd) as shown in figure 3.7, which enable us to achieve these manipulation with high precision.

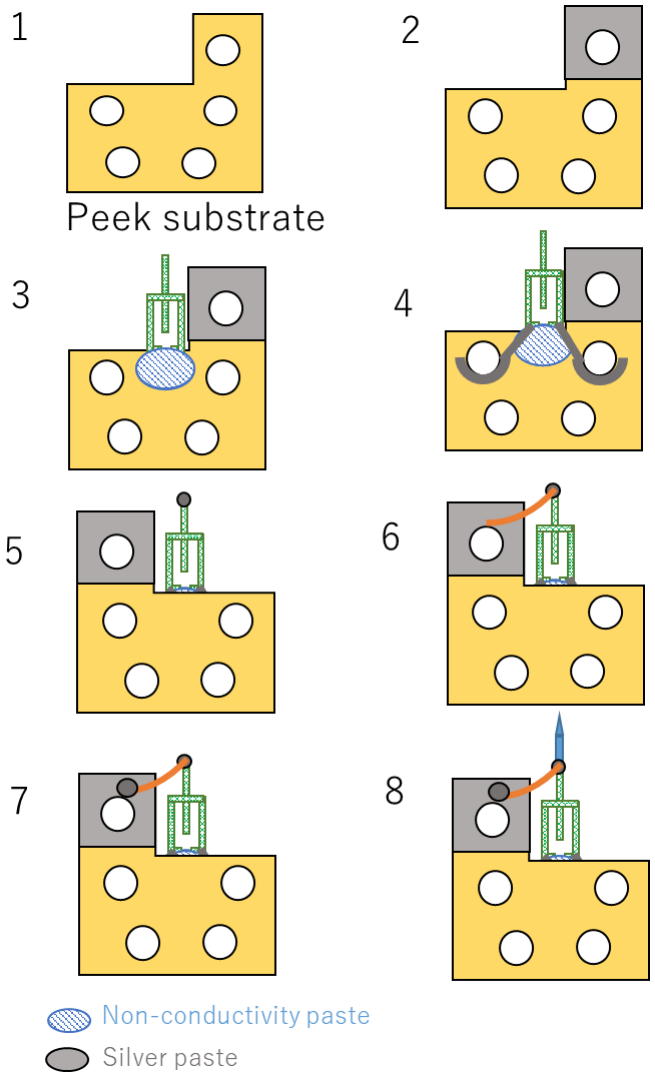

Figure 3.6 Procedure to prepare the sample.

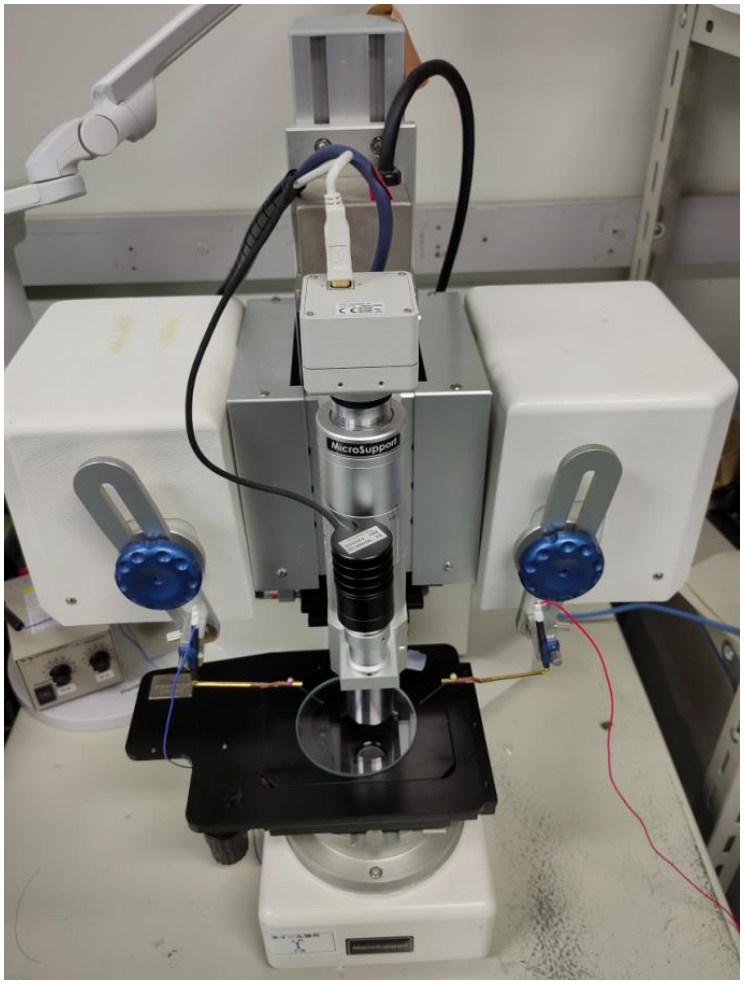

Figure 3.7 Photo of the micro manipulator.

The surface condition is quite important for making a nanocontact. The carbon atoms may have incorporated into the nanocontacts if the contaminations exist. So, it is important to make the surface of the metal wires clean to avoid such phenomena. After the sample is set onto the holder, the sample firstly was baked inside a JEC-4000DS dry pumping station (JEOL corp. figure 3.8) for at least 24 h prior to the insert into the TEM column. After the baking is finished, the holder is insert into the TEM column

and the sample is further irradiated by the electron beam irradiation for at least 24 h before experiment for further removing the contaminations (such as the hydro carbon) adsorbed on sample surface.

Figure 3.8 Photo of dry pumping station, which have the baking function, used in this study.

3.4 Mechanical measurement system

As mentioned above, we use the LER as the force sensor to measure the equivalent spring constant of the nanocontact using the FM method. In the FM method, the equivalent spring constant is calculated from the amount of shift in resonance frequency

of the sensor, so it is necessary to measure the resonance frequency of the sensor before making the contacts. The excitation signal (AC voltage) that keeps the amplitude constant is applied to the LER, and the amplitude of the output AC voltage is measured. The frequency of the excitation voltage is swept near the resonance frequency of LER which is ~1 MHz, and the frequency characteristics of the output signal are examined. The frequency at which the amplitude of the output signal is maximized was determined as the resonance frequency. And also, the phase difference between the the input (excitation) and output signals was estimated at the resonant frequency, which was used for detecting the shift of the resonant frequency due to contacting with a metal nanocontact.

Originally, the phase difference between the input (excitation) and output signals at resonance should be 0, but actually in the measurement system the phase difference between the excitation and output signals does not become 0 even at the resonance frequency. Because a charge amplifier (Koribri) is used for converting the charge to voltage signal and the offset due to the reactance is included in the system. At least, by the charge amplifier (Koribri), a phase difference of $\frac{\pi}{2}$ is generated. Figure 3.9 shows a photograph of the charge amplifier, which bandwidth is 250Hz -15MHz and Gain is 10V/pC. Feedback control is performed so as to maintain the initial phase difference between the input (excitation) and output signals using a phase-locked loop (PLL) so

that the resonance state of the oscillator is maintained. When a nanocontact is formed, the resonance frequency of the LER changes due to the mechanical response of the nanocontact, and the phase difference changes accordingly. The amount of the frequency shift is calculated from the change of the phase difference. Also, the oscillation amplitude of the LER is maintained at about 30 pm by keeping the output voltage, which is in proportion to the amplitude. Nanonis OC4 oscillation controller (SPECS crop, SPM controller) is used to excite the LER, measure the output voltage, which is converted from the charge generated in the LER during the oscillation. Also, it has the phase feedback through the phase synchronization circuit, and calculate the change of the resonance frequency.

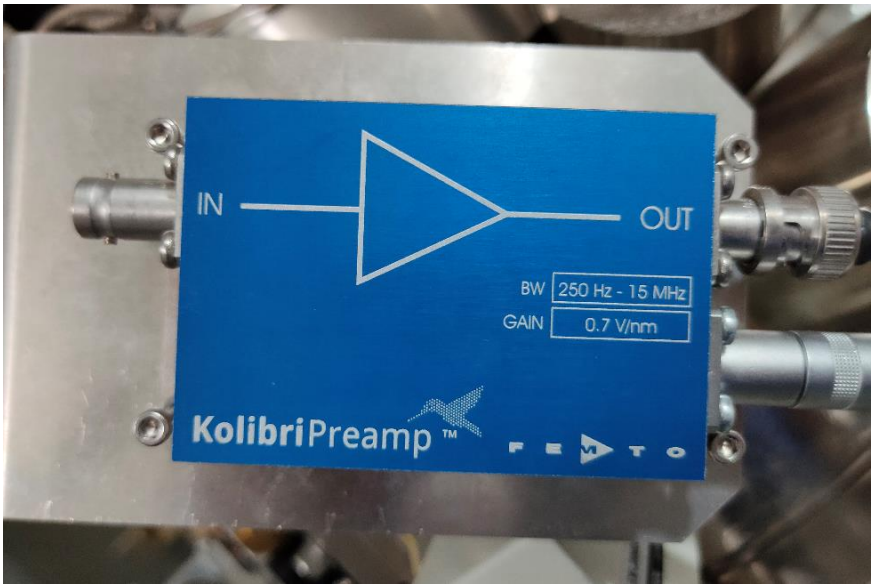

Figure 3.9 The change amplifier used in this study

The signal system are shown in figure 3.10. First, operate the SPM controller on the PC, and input the excitation signal (AC voltage) from the SPM controller to the LER on the peek board. The LER causes an inverse piezoelectric effect by the excitation signal, and at the same time it expands and contracts, and at the same time, a weak electric charge (oscillation signal) is induced in the electrode on the opposite side of LER by the piezoelectric effect. The oscillation signal is converted into a voltage by the Kolibri Preamp (HQA-15M-10T, FEMTO Messtechnik GmbH) and input to the SPM controller. The SPM controller calculates the amount of change in the resonance frequency from the excitation signal and oscillation signal, and inputs the corresponding analog signal to the A/D converter. The A/D converter converts an analog signal into a digital signal and outputs the measurement data to a PC. NI PXI 6289 manufactured by NATIONAL INSTRUMENTS is used for A / D and D / A converters as shown in figure 3.11.

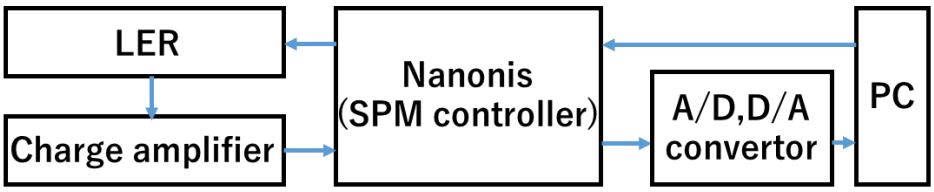

Figure 3.10 Signal paths of the mechanical measurement system in this study

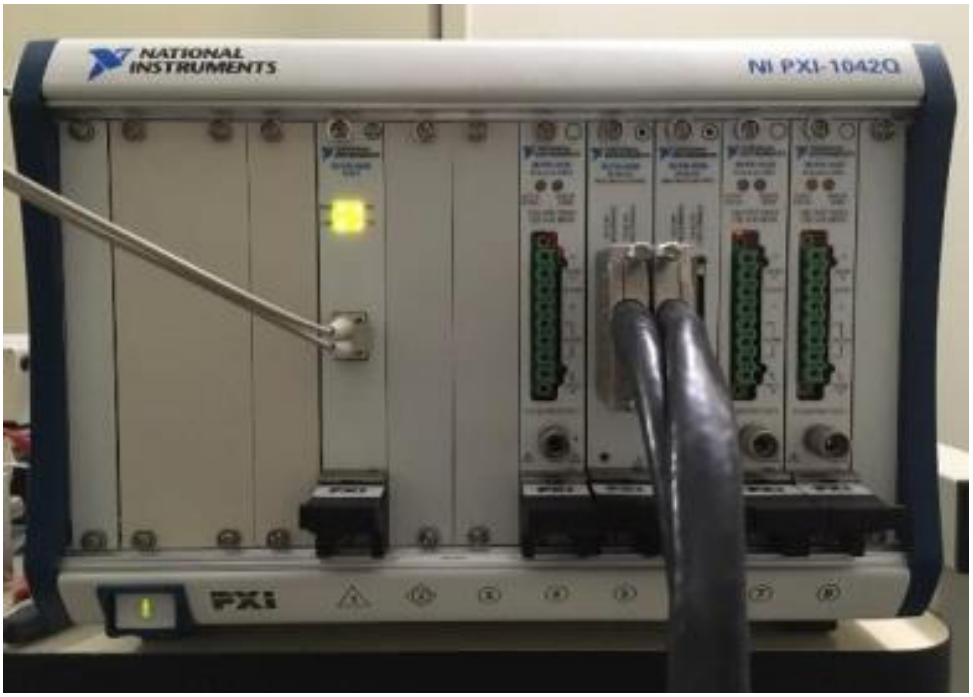

Figure 3.11 A/D, D/A converter used in this study

3.5 Electrical conductance measurement system

Conductance measurement of nanocontacts is performed at the same time as mechanical measurement. It is performed by a LabVIEW program. The excitation voltage for LER is applied to one side of the nanocontact and the current is detected by converting to the voltage. These values are recorded in synchronization with the results of the mechanical measurements. The DLPCA-200 (FEMTO) as shown in figure 3.12 is a current amplifier, which gain and measurable rage is from 10^3 to 10^{11} V/A and $\pm$10V, respectively. The nanocontact is connect in series with the D/A converter and the input terminal of the current amplifier. Therefore, the resistance value directly

obtained in the measurement system is the total resistance, which including the resistance value of the nano contact, the output impedance of the D/A converter and the input impedance of the current amplifier. Since these resistances are connected in series, the resistance value of the nanocontact is calculated by dividing each resistance from the measurement data.

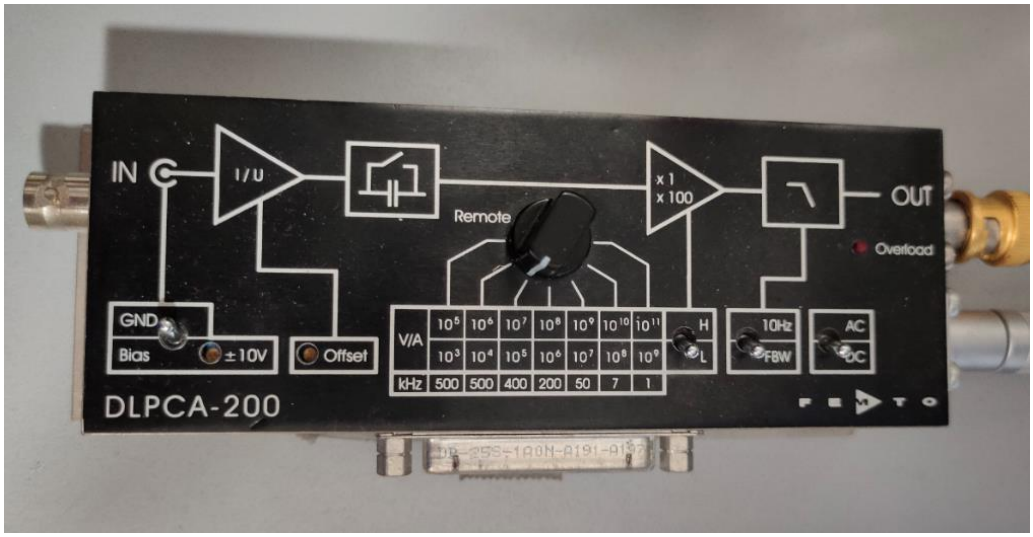

Figure 3.12 The current amplifier used in this study

3.6 Calibration of the force measurement system

3.6.1 Calibration of the sensitivity of LER from TEM observation

The spring constant of a quartz LER, k_0, should be estimated precisely, since it is necessary for calculation of the spring constant of nano contacts as shown in equation

2.5. It can be estimated by the shape, however, it is not reliable due to the measurement error and the irregular shape caused by the fabrication as marked in figure 3.13. Herein, we propose a new method for estimating the spring constant of LER by using thermal noise spectrum. Even when LER is not excited electrically or mechanically, at room temperature, it is thermally oscillated with its resonance frequency, which generate fluctuation of induced electrical charge by thermal noise. The thermal noise density, V[V/√Hz], is expressed by the following formula [1].

$$V\left[\mathrm{V}/\sqrt{\mathrm{Hz}}\right] = \frac{a}{S}\sqrt{\frac{2k_{\mathrm{B}}T}{\pi k f_o Q\left[\left\{1-\left(f/f_0\right)^2\right\}^2+\left(\frac{f/f_0}{Q}\right)^2\right]}+n_{\mathrm{def}}^2} \qquad 3.1$$

where a is the conversion ratio of the charge amplifier (10 V pC^{-1} in this study), $S[\mathrm{m}/V]$ is sensitivity, corresponding to the oscillation amplitude of the LER per the output voltage, k_0, spring constant of LER, f_0, resonance frequency, Q, Q-factor, k_B, Boltzmann constant, T, temperature, n_{def}, floor noise density. It indicates that the spring constant of LER can be estimated when the sensitivity of LER is obtained. So it is important to obtain the sensitivity of LER. However, it is difficult to measure the sensitivity because of small amplitude (below 1nm). In this study, the sensitivity which is expressed by the ratio between the output signal and the oscillation amplitude is obtained by combining the TEM observation.

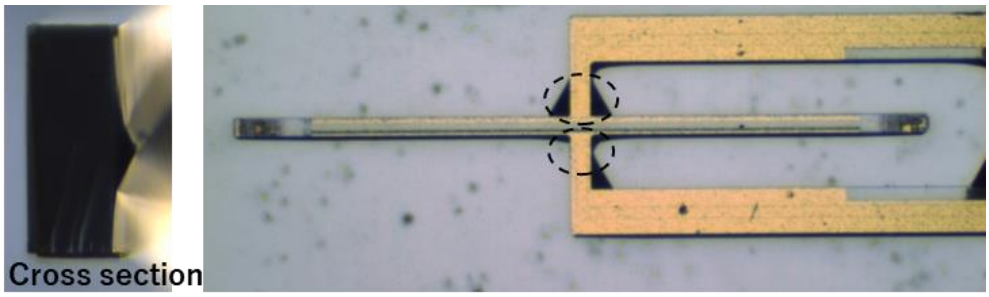

Figure 3.13 photo of the LER. The dashed circles indicate the irregular shape.

For estimating the amplitude of oscillation, a TEM image of thin amorphous carbon, which was adsorbed near the edge of LER, was captured during the oscillation (figure 3.14 a). In FFT pattern of the captured TEM image (figure 3.14 b), white fringes were found, indicating that the FFR pattern was modulated by the LER oscillation. A contrast of a TEM image can be expressed as follows.

$$f(x) = \sum_i \alpha_i \sin(k_i x + \delta_i) + C \tag{3.2}$$

When the sample is shifted by x, the contrast function is described by $\beta(x') = f(x - x')$. Since the LER oscillated as a sinusoid, the duration time at each displacement can be described by arcsine function such as

$$p(X) = \frac{1}{\pi} \frac{1}{\sqrt{A^2 - X^2}} \tag{3.3}$$

Therefore, the contrast of thin amorphous carbon during the oscillation can be described as follows.

$$g(x) = \int_{-\mathrm{A}}^{\mathrm{A}} dx' p(x') \beta(x') \tag{3.4}$$

where A is the amplitude of the oscillation. From calculation, the following formula can be obtained

$$g(x) = \sum_i J_0(k_i A)\alpha_i \sin(k_i x + \delta_i) + C \quad (3.5)$$

Where $J_0(k_i A)$ represents the zero order Bessel function of the first rank. It indicates that the FFT pattern of $g(x)$ is expressed by multiplying the FFT pattern of $f(x)$ with $|J_0(k_i A)|$ and the modulation observed in the FFT pattern of figure 3.14b corresponds to $|J_0(k_i A)|$. By fitting $|J_0(k_i A)|$ with the experimental intensity profile of the FFT pattern (figure 3.14c), the amplitude of LER oscillation was determined to be 0.89nm. This analysis is reasonable, since the intensity modulation in the FFT pattern is well reproduced by the Bessel function (figure 3.14c). Then, the sensitivity was estimated to be 1.75nm/V, since the output voltage was 500mv. The sensitivities were also estimated for different output voltages of 400mv, 450mv, 550mv and 600mv. These results showed a linear relationship between the amplitude and the output voltage as shown figure 3.13d, indicating that the sensitivity was 1.75 nm/V.

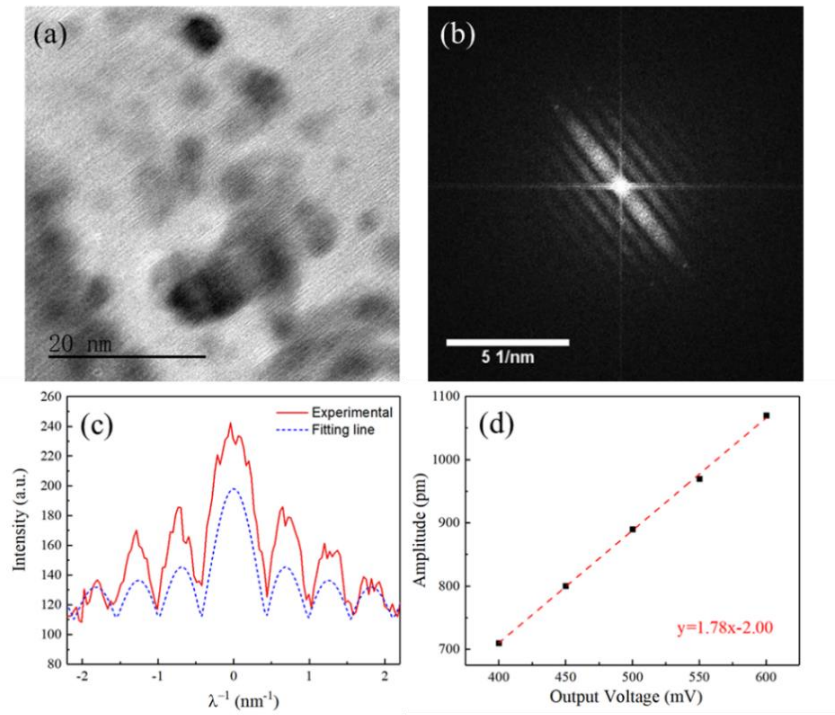

Figure 3.14 (a) A TEM image of thin amorphous carbon, which was adsorbed near the edge of LER, was taken during the oscillation. (b) A FFT pattern of the TEM image. White fringes appear, which corresponds to the LER oscillation. (c) The intensity profile of the FFT pattern was indicated by red line. The fitting curve of $|J_0(k_i A)|$ (the absolute value of the zero order Bessel function of the first rank) was indicated by blue line. The fitting was the best when the amplitude of LER oscillation was 0.89nm. (d) A graph of the amplitude of the LER oscillation as a function of the output voltage. The slope of the linear relationship between the amplitude and output voltage correspond to the sensitivity of the LER.

3.6.2 Calibration of the spring constant of LER

To determine the spring constant of LER, a thermal noise spectrum was acquired around the resonance frequency by spectrum analyzer (FSP of Rohde & Schwarz co.). The measurement band is 10Hz, the center frequency of the sweeping is 995510Hz, and the sweep range is from 994510Hz to 996510Hz. The thermal noise spectrum is obtained for average 2000 time sweeps. The time for one sweep is 5 second and there are 501point in one sweep. After obtain the thermal noise spectrum, the estimated sensitivity was used for fitting the thermal noise spectrum to get the spring constant and Q-factor of LER by Levenberg-Marquardt method [2], which is one of reliable non-linear least squares methods. Figure 3.15 shows an example of such fitting, which the thermal noise spectrum measured in experiment (blue line) is fitted by the equation 3.1. The fitted spring constant of the LER is 1.85×10^{6} N/m, the Q factor is 12000.

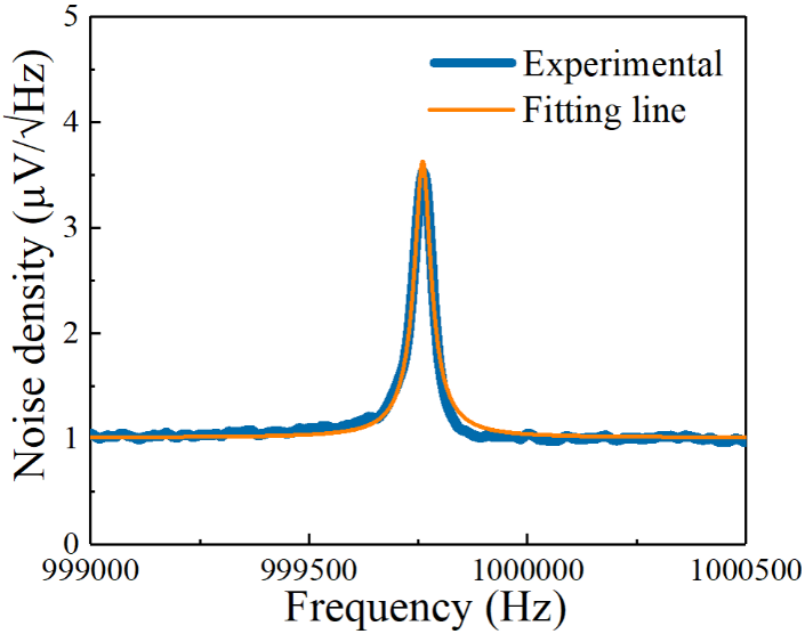

Figure 3.15 The measured thermal noise spectrum (blue line) and the fitted line using the equation 3.1 (orange line).

3.6.3 Influence of the wire connection on the mechanical properties of LER

As we have mentions above, we need to make an electrical connection at the edge of LER to measure electrical conductance of metal nanocontact, which was necessary to investigate the structure and deformation process of metal nanocontacts. However, such an electrical connection was thought to induce imbalance between the two beams of LER. It means that an electrical connection may have an influence on the sensitivity and Q-factor of LER since the output signal comes from two beams. Therefore, the properties including the sensitivity and the spring constant of the LER connected to the Au wire (10μm in diameter), LER connected to the Au foil ribbon (~20 μm in width

and 1 μm in thickness) and a bare LER was estimated. Figure 3.16 shows the photographs of the 3 samples.

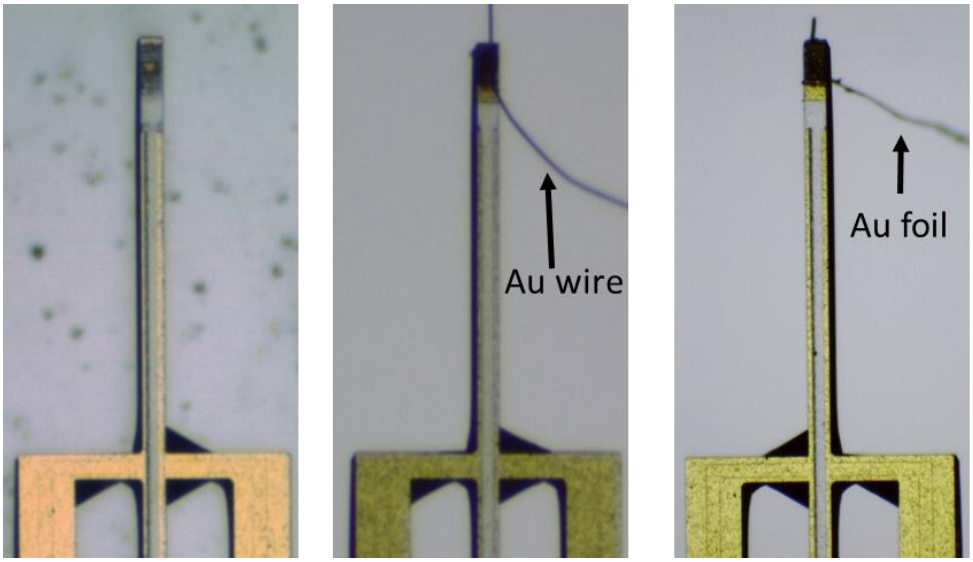

Figure 3.16 The photographs of the bare LER, LER connected with the probe and Au wire, LER connected with the probe and the Au foil ribbon.

The sensitivity of LER was measured to be 0.57, 0.56 and 0.47 V/nm, respectively, for bare LER, LER connected with a gold foil and one with gold wire of 10μm in diameter by analyzing the TEM image of amorphous carbon film as mentioned above. And, we measured individual noise spectrums for them (Figure 3.17) to estimate individual effective spring constants. From the thermal noise spectrums, it is clearly that the peak in the spectrum of bare LER is she sharpest, and the one of the LER connect with Au foil ribbon shows slightly blur than the one of bare LER. However, the

peak in the spectrum LER connect with Au wire is obviously blur than the above two peaks and the peak is not smooth.

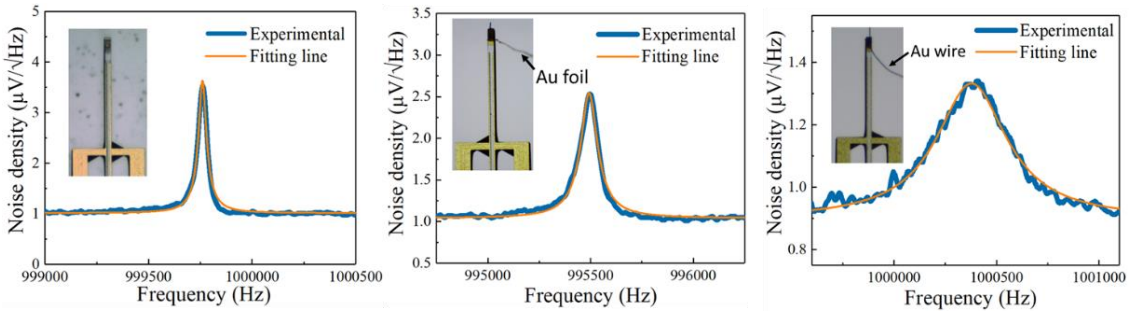

Figure 3.17 Experimental thermal noise spectrums of the LER without electrical connection, with Au-foil and with Au-wire, respectively. The inserted optical microscopy images show these three different LERs. By fitting formula (2) to the experimental thermal noise spectrum as shown by orange curves, the spring constant and Q-factor of the LER were estimated.

The spring constant and Q-factor of the bare LER (one beam) were estimated to be 9.264×105 N/m and 28000, respectively, by fitting the experimental thermal noise spectrum as introduced in the previous chapter. While, in the case of Au-foil, the spring constant and Q-factor of the LER were estimated to be 9.276×10^5 N/m and 12000, respectively, and in the case of Au-wire, they were estimated to be 7.516×10^5 N/m and 2600, respectively. Obviously, the spring constant and Q-factor of the LER connected

with Au-wire are worse than ones of bare LER. This deterioration seems to be caused by imbalance between two beams of LER (the electrical wire is connected to one-side beam). On the other hand, the LER connect with the Au foil showed the similar performance with the bare LER, although the resonance frequency seems to be reduced by energy dissipation due to friction at the connection with the Au foil. Therefore, the LER connect with the Au foil was used for a force sensor in our developed TEM holder.

In the case of the LER connecting with an Au foil, the resonance frequency can be measured with accuracy of 6 digits because of high Q-factor (~12000). The spring constant of LER was estimated with accuracy of 3 digits. For evaluation of the resolution of the measured spring constant, the shift of the resonance frequency was measured for 10 seconds (24000 data). The standard deviation of 24000 data was 0.37 Hz, corresponding to 1.37 N/m, (1 Hz shift of the resonance frequency corresponds to the spring constant of 3.71 N/m). The accuracy of this method seems to be sufficient enough to determine the spring constant of Pt NC or atom chain, which effective spring constant has been reported to be from 10 to 20 N/m in theoretical calculation [3].

3.7 Conclusion

In this chapter, I introduced the experiment setup used in this study. At first I introduce the importance of the vacuum condition in this study and the UHV-TEM used

in the experiment. Then I showed the self-developed TEM holder, which equipped a 3 axis movement system with high stability and resolution. The detail design of the holder is presented and the mechanism of the coarse motion system is discussed. Then I demonstrated how to set the LER in the TEM holder, and how to make electrical connections between the LER to the electrical wires, and how to make electrical connections to measure the conductance of the sample. Then the equipment and method for measure the mechanical response and the conductance are introduced. Finally, the properties of LER including the sensitivity and Q factor and the influence of the wire connection on the LER are discussed. The Au foil ribbon is chosen as the connection media since it has the minimum influence on the LER.

References

[1] T. R. Albrecht, P. Grütter, D. Horne, and D. Rugar, Frequency Modulation Detection Using High-Q Cantilevers for Enhanced Force Microscope Sensitivity, Journal of Applied Physics 69, 668 (1991).

[2] C. Kanzow, N. Yamashita, and M. Fukushima, Levenberg–Marquardt Methods with Strong Local Convergence Properties for Solving Nonlinear Equations with Convex Constraints, Journal of Computational and Applied Mathematics 172, 375 (2004).

[3] G. Rubio-Bollinger, S. R. Bahn, N. Agraït, K. W. Jacobsen, and S. Vieira, Mechanical Properties and Formation Mechanisms of a Wire of Single Gold Atoms, Phys. Rev. Lett. 87, 026101 (2001).

Chapter 4 Mechanical properties of Pt monatomic chains

Introduction

This chapter contains the measurement and analysis of the mechanical properties of the Pt monatomic chains. The spring constant of individual bond in the atomic chains are also calculated.

In Chapter 4.1, we show the measured spring constant value of the monatomic chains with different number of atoms in the chains. In Chapter 4.2, we show the calculation of individual bond spring constant in the monatomic chain. In Chapter 4.3, We analysis the mechanical behavior of the monatomic chains from the theoretical point of view.

4.1 Spring constant and conductance of Pt atomic chains

At first Pt is used for the materials to making the nanocontacts. After making Pt nanocontacts, it was further thinned by stretching. The electrical conductance and effective spring constant were recorded at the same time. The amplitude of the LER oscillation was set to be ~30 pm which is much smaller than the interatomic distance of two neighbor Pt atoms, and the bias voltage for measuring the electrical conductance was set to be 12 mV. The electrical conductance of metal NC was worth investigating because it has been reported to be almost in proportional to the cross section at the narrowest constriction [1]. It means that the conductance reflects on the cross section. It is a supportive information, since a TEM image only provides a projected information.

Figure 4.1 shows a typical time evolution of the spring constant and electrical conductance of the Pt nanocontacts until breaking and a series of TEM images taken from the corresponding process. Very thin Pt nanocontact could be made because of high stability of our developed TEM holder. The conductance decreased stepwise during stretching the sample. By comparing with TEM images, the conductance plateaus seem to appear when the Pt NC has stable structure. In figure 4.1, the conductance of $18.4G_0$ ($= 2e^2/h$: the quantized unit of conductance, where e is elementary charge and h is Planck constant) and one of $2.0G_0$ seem to have a stable structure. Between 18.4 and $2.0G_0$, the conductance decreased with some steps (14.0,

11.1, 9.4 and 7.0 G_0, see the histogram of figure 4.1c), while the spring constant decreased without clear steps (also see the histogram of Figure 4.1h). Some steps in conductance may correspond to meta-stable structures during the thinning process. The spring constant is determined by the entire structure of the Pt nanocontact, while the conductance is determined by the minimum cross section area of the nanocontact. Therefore, the Pt nanocontact of figure 4.1 may deform continuously during the stretching process, while sometimes the minimum cross section area of the nanocontact didn't change so much.

The Pt nanocontacts of $18.4G_0$ in conductance has the effective spring constant of 72.3 N/m and one of $2.0G_0$, has the effective spring constant of 13.2 N/m. The single Pt atomic chain was observed at the last conductance plateau (~$2.0G_0$) [2]. It consisted of three Pt atoms as shown in figure 5e and was maintained for around 2 second so that we could estimate the conductance and spring constant more precisely by average. The average conductance is 2.0 G_0 and effective spring constant is 13.2N/m. We should notice that the measured spring constant values are the total spring constant between the LER and the fixed board. Which contains the contribution not only for the nanocontact, but also from the other part, here we define the parts except the target part as the base part [3,4].

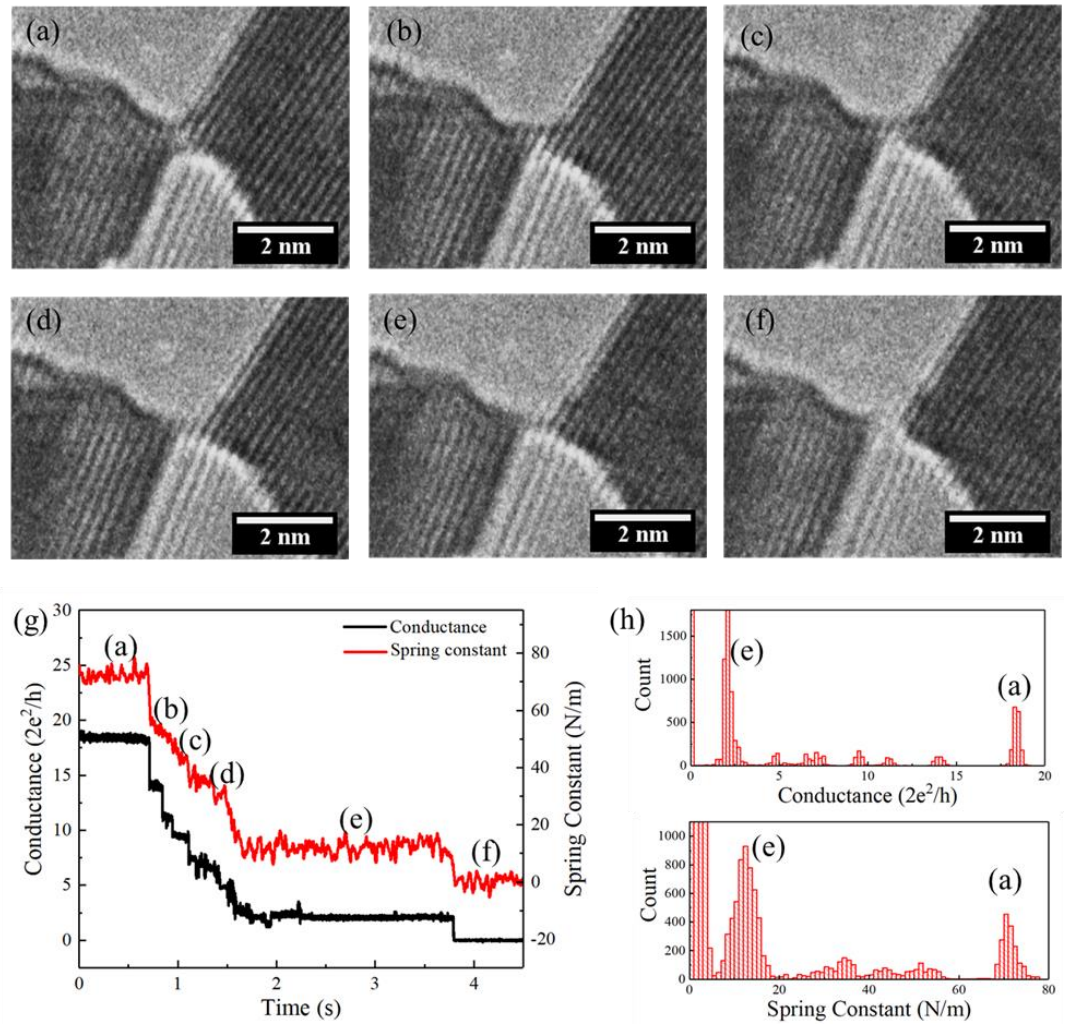

Figure 4.1 (a) A typical time evolution of the spring constant and electrical conductance of the Pt NC until breaking. (b) A series of TEM images taken from the corresponding process. (c) Histogram of electrical conductance and spring constant. The former shows two large peaks and five small peaks except for zero, while the latter, two large peaks and some broad peaks except for zero.

In this study, about 150 Pt atom chains were fabricated and analyzed from the simultaneous TEM obeservations with the measured electrical conductance and spring

constant. We thought that the spring constant of the atomic chains could be determined more accurately when the shape of the base supporting them did not change during the measurement. During making the Pt atomic chains, two different sets of bases are obtained. Figure 4.2 a shows the [110] direction of both bases are horizontal, so the Pt atomic chains made by these bases are called the [110]-[110] chains. Since there is an angle of 108^{o} of both sides of the bases, both sides of the pyramid-shape are composed by the (111) planes. The crystal orientation can be also confirmed by Fast Fourier transformation (FFT) patterning which is shown as the inset in figure 4.2. Figure 4.2b shows a Pt monatomic chain, which axis is parallel to the [110] direction of the right side base and the [111] direction of the left-side base. The atomic chains fabricated by these bases are defined as [110]-[111] chains hereafter. The left-side base is a triangular shape with an angle of 77^{o}, while the right side is a quadrangular pyramid-shape with 113^{o} further confirmed the above suggestion. During the experiment, The [110]-[110] Pt atomic chains and [110]-[111] Pt atomic chains were fabricated and the spring constant are measured.

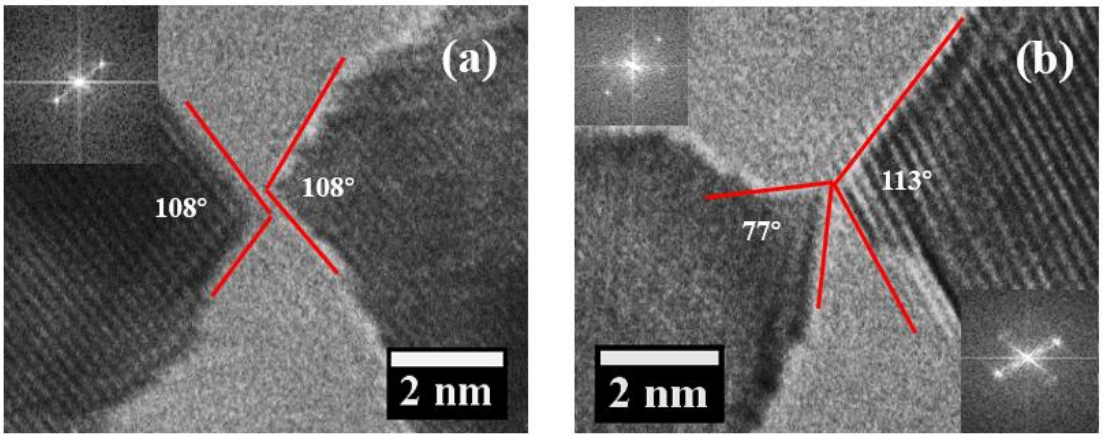

Figure. 4.2 TEM image and Fast Fourier Transform (FFT) pattern of the base wires. (a) The two Pt wires horizontally along the [110] contact from the FFT pattern and the corresponding angles of the edge, indicating the wire is along the [110] direction. (b) The left base wire is horizontally along the [111] direction, and the right base wire is horizontally along the [110] direction from the FFT pattern and the corresponding angles of the edge.

Figure 4.3 shows the measured results of the [110]-[110] chains. The number of Pt atoms in the chain (including two edge atoms in the base) are different in different stretching process, which can be classified by 2, 3, 4 and 5 atoms. However, we did not observe that the number of Pt atoms in the chain increased one-by-one by stretching further, which is different with the previous report [2,5,6]. We think that the number of atoms in the chain may depend on the initial atomic configuration of the nanocontact before the formation of the chain. In calculation, for introduction of a new atom into

the atomic chain, one atom must break the bond with the other atoms at the base supporting the chain, which requires more force (6.9 nN) than breaking the bond in the atom chain (4.2 nN) [7]. It implies that our observation is reasonable. We suppose that the inconsistence may come from the different configuration of the connecting part with the atomic chain. In the TEM images (figure 5.3a–d), the number of atoms in the chains were identified by the intensity profile obtained from the TEM images, which is along the chain axis (figure 4.3e-h). Since the observed TEM images (figure 4.3a–d) were well reproduced by the simulated ones, which was calculated based on the assumption that the atomic distance was 0.25 nm in the chain, the number of atoms was confirmed to be properly counted.

The conductance variations in figure 4.3i-l show that the [110]-[110] chains with 2-4 atoms has a conductance ~1.8 G_0 and ~1.3 G_0 for the chains with 5 atoms. Also, in figure 4.3i-l, we found the conductance value are almost constant when chains are stretched for all the chains with 2-5 atoms. The parity oscillation as previously reported does not appear. This reason may be explained by room temperature measurement [8,9]. In addition, although the s-state and d_{xz} and d_{yz} conductance channels exist in the Pt monatomic chains, the almost constant conductance value indicates the contribution of the d-state is quite small [10].

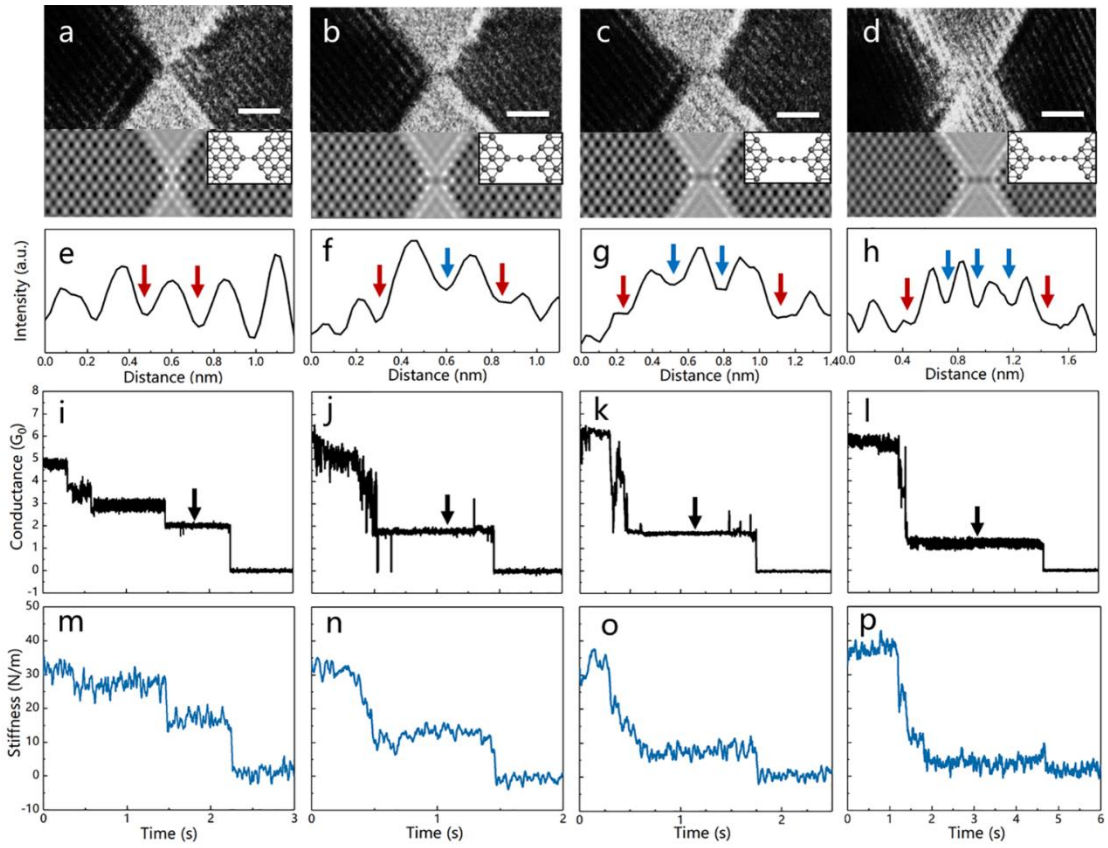

Figure 4.3. (a-d), TEM image of [110]-[110] chains with 2-5 atoms and corresponding simulated TEM image with the atomic configurations shown in the figure. (Scale bars: 1nm). (e-f), line intensity profile along the chain axis of the TEM images shown in figure 5.3 a-d. (i-l), conductance change during stretching of [110]-[110] chains with 2-5 atoms. (m-p), spring constant change during stretching of [110]-[110] chains with 2-5 atoms.

In figure 4.3m-p, the spring constant traces of the atomic chains shows the similar behavior with the conductance when it is stretched. In the spring constant traces, there are some light variations exist. However, we cannot find any correlations between these

variations and the TEM images or conductance of the atomic chains. These slight variations may depend on the slightly difference between the stretching direction and the LER oscillation direction. Because the spring constant is maximum when the stretching direction is the same with the LER oscillation direction. Such influences can be ignored because they are not usually observed and the variation is quite small.

During the stretching of the atomic chains, there are some sudden drops in the spring constant traces, and then the value is recovered to a constant value. Such trends have frequently been observed for the Pt chains and also the Au nanocontact which will be introduced in the next chapter. This behavior suggests that after the plastic deformation, the atomic structure is not stable immediately, after a moment, the structure becomes stable by the atom rearrangement. This result has also been observed in the previous papers [2,11]. The detail of the sudden drops will be discussed in the next chapters in the deformation of Au nanocontacts. As concerned with the spring constant evolution, the spring constant is different depending on the number of atoms such as 18, 11, 8, 5N/m, respectively, for the [110]-[110] chains have 2-5 atoms.

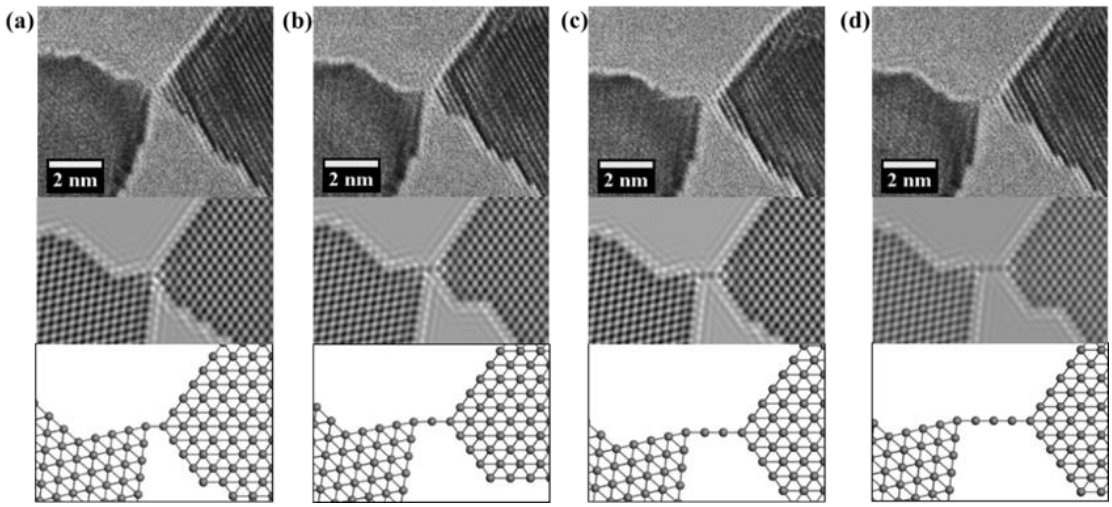

Figure 4.4 (a)–(d) TEM images, simulated TEM images, and corresponding atomic structures of atomic chains containing two, three, four and five atoms (including edge atoms) of the [110]-[111] chains.

4.2 Individual Pt-Pt atomic bond spring constant in the Pt atomic chains

The spring constant histograms of the [110]-[110] and [111]-[110] chains were constructed from the spring constant evolutions of all measured Pt atomic chains (Figure 4.5). In each histogram, 4 peaks correspond to the chains of 2-5 Pt atoms. In the case of the [110]-[110] chain, the measured spring constant was determined to be 18.71±2.08N/m, 10.34±2.06N/m, 7.32±1.92N/m and 5.65±2.65 N/m on average, respectively, for the chains contained 2, 3, 4 and 5 atoms. Similar trend was found in the case of the [111]-[110] chain, where the measured spring constant was determined to be 16.96±1.93N/m, 9.75±1.72N/m, 6.96±1.82N/m and 5.44±1.47 N/m on average,

respectively for the chains contained 2, 3, 4 and 5 atoms. In this analysis, the error in the spring constant value are mainly due to the signal noise and mechanical instability of suspended chains. At a glance, the spring constant of the [110]-[110] chains seems slighter higher than that of the [111]-[110] chains when the number of atoms in the chain are the same. However, since this spring constant correspond to a series coupling of the spring constant of a Pt atomic chain and one of both bases supporting it, it is necessary to subtract the spring constant of the base part from the measured one.

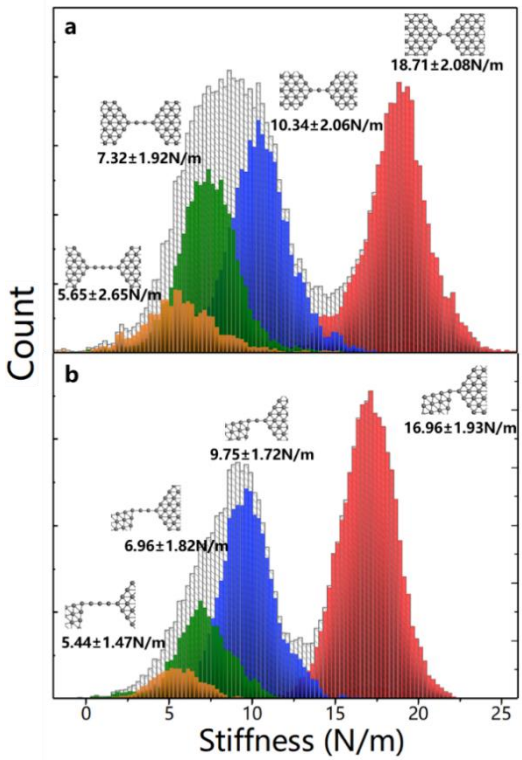

Figure 4.5 (a), (b) Spring constant histogram of the [110]-[110] and the[110]-[111] single atomic chain, respectively. The plot in gray, red, blue, green and yellow is the total histogram and the spring constant of chains contained 2-5 atoms, respectively.

For estimating the spring constant of the Pt atomic chain, we assumed that the spring constant of two bases supporting the atomic chain (k_{base}) was constant. Because the atomic chain was connected to the apex at crossing two different (111) facets of the base, which shape was observed not to change during stretching. In addition, the number of atoms constituting the atomic chain is so small that the volume difference in the base can be ignored. We also assumed that the bond spring constant between the edge atom of the base and the chain atom (k_{edge}) was different from one between two neighbor chain atoms in the chain. In addition, the central bond in chains have 4 and 5 atoms are assumed to be different($k_{central1}$ for central bonds in 4atoms and $k_{central2}$ for central bonds in 4atoms) [12,13]. The model is shown in figure 5.6. Because the bond strength is expected to decrease when increasing the coordination number in metallic bond. The measured spring constant of the Pt atomic chain, which was obtained from the histogram ($k_m(i)$, i represents the number of constituent atoms in the chain), can be expressed as follows.

$$\frac{1}{k_m(2)} = \frac{1}{k_{base}} + \frac{1}{k_{edge}} \tag{4.1}$$

$$\frac{1}{k_m(3)} = \frac{1}{k_{base}} + \frac{2}{k_{edge}} \tag{4.2}$$

$$\frac{1}{k_m(4)} = \frac{1}{k_{base}} + \frac{2}{k_{edge}} + \frac{1}{k_{central1}} \tag{4.3}$$

$$\frac{1}{k_m(5)} = \frac{1}{k_{base}} + \frac{2}{k_{edge}} + \frac{2}{k_{central}} \tag{4.4}$$

Using formula (4.1) to (4.4), the spring constant of the bases, k_{base}, was estimated

to be 96.0 N/m for [110]-[110] chains and 67.3 N/m for [111]-[110] chains. By subtracting the contribution of the base part, the spring constant for the [110]-[110] chain contained 2-5 atoms was estimated to be 23.1±2.08N/m, 11.6±2.06N/m, 7.9±1.92N/m and 6.0±2.6 N/m, respectively. And those value for the [111]-[110] chain contained 2-5 atoms were estimated to be 22.9±1.93 N/m, 11.5±1.72, 7.8±1.82 and 5.9±1.47, respectively. Therefore, the spring constant of the [110]-[110] chains well match with ones of the [111]-[110] atomic chains. It implies that the spring constant of the bases is estimated appropriately. For confirmation, we estimated the spring constant of the bases from the viewpoint of the shape by assuming that the Pt junction was cylindrical shape, which was connected with the cone-shaped base in both sides (See the detail in the Appendix A). In the case of the [110]-[110] chains, the spring constant of the base part was considered to be equal to the measured spring constant for the Pt junction of 0.6nm in length and 0.8nm in diameter, which was 96±6 N/m. In the case of the [111]-[110] chain, the spring constant of the base part was considered to be 55±4 N/m. These values were close to ones obtained by expressions (4.1) to (4.4) as mentioned above.

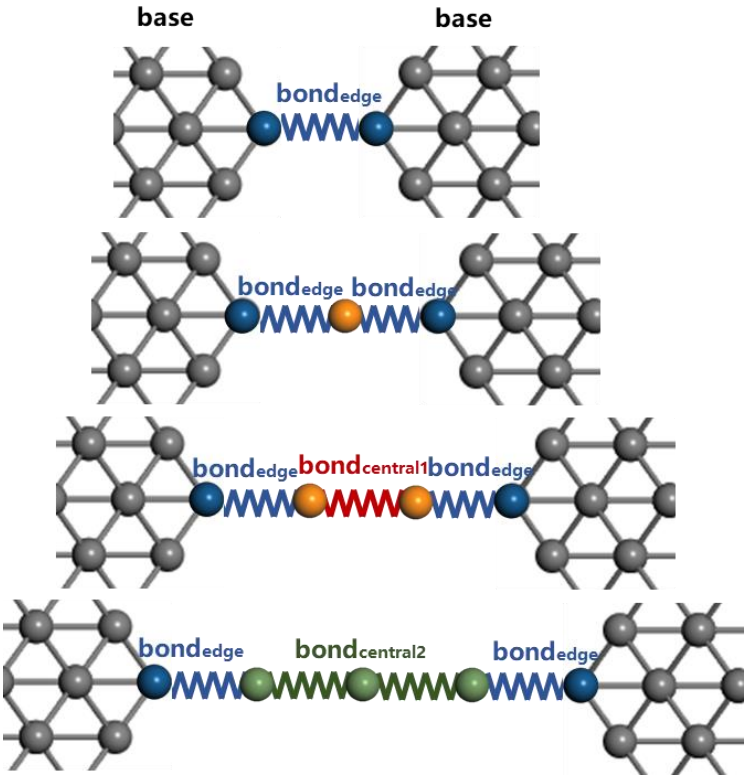

Figure 4.6 model to calculate the spring constant of each part in the chain.

By formula (4.1) to (4.4), the k_{edge}, $k_{central1}$ and $k_{central2}$ are determined to be 23.1, 25.1 and 24.9N/m in [110]-[110] chains and also, to be 22.9, 24.3 and 24.6N/m, respectively, for the [111]-[110] chains. The $k_{central1}$ and $k_{central2}$ shows the similar value indicates the spring constant between the bonds inside the chains are almost independent with the number of atoms in the chain. Taking into account that the minimum measurable spring constant is about 1 N/m in the present experimental condition, the bond spring constant between two neighbor chain atoms, $k_{central}$ (~25N/m) is obviously higher than one between the edge atom of the base and the chain

atom, k_{edge} (~23N/m). And these values are higher than the bulk value by our simply calculation (~20 N/m). Assuming that the bond length is 0.25 nm and cross sectional area and $\pi \times 0.12^2$ nm2 in the Pt atomic chain, the Young's modulus of the Pt atomic chain can be estimated to be about 130 GPa. This value is slightly smaller than the Young's modulus of bulk Pt crystal (160 GPa), although it changes largely depending on the spatial spread of electrons involved in the bonding. However, considering that the bulk bond has 12 coordination numbers, it can be said to be extremely high. Theoretically, for 5d metals such as Ir, Pt and Au, the bond spring constant in low coordinated structures such as chains are suggested to be strong relative to bulk bonds [5,14].

4.3 Analysis of the mechanics in Pt-Pt atomic chains

Quantitative measurement of the bond spring constant is quite important to understand the physical or chemical properties of one dimensional atomic chains, because they do not correspond to a structure of the lowest energy. We can imagine that a single atom chain cannot be maintained without it being stretched by the supporting materials or fixed by other constrains. It indicates that it is necessary to take into account that the atomic chain is maintained under stretching. Such effect, which is called as string tension, is unique to one-dimensional atomic chains and may give rise to specific

physical or chemical properties. The string tension can be defined by consider the positive work to pull the wire out of the bulk tips, and is given by [15], $f = (F - \mu N)/L$, where F is the free energy of the wire, N is the number of atoms, μ is the chemical potential of bulk Pt and L is the length of the wires. The string tension f is a force which is generated by a suspended wire seek to shrink to a stable structure. Previously, the string tension has been pointed out to be a critical parameter to determine the stable atomic configuration in one-dimensional materials. Because it has been predicted that a tip-suspended wire has a stable configuration at the minimum string tension rather than at that of the free energy F [15,16].

To further analyses the mechanical properties of Pt-Pt bond in the atomic chains, we attempted to calculated the string tension using density functional theory (DFT) calculations. The calculations in this work were carried out using the DMOL3 code because this code is both fast and well-suited to cluster calculations, as it employs localized basis sets [17,18]. The cores of the Pt atoms were described based on the hardness conserving semilocal pseudopotential (dspp) method, and only outer electrons were handled explicitly [19]. A real-space cutoff of 0.45 nm and a double-zeta, atom-centered basis set (dnd) were employed in our calculations, which was comparable to the use of a Gaussian 6-31G* basis set although the numerical basis set is much more accurate than a Gaussian basis set of the same size [19]. The exchange-correlation was

determined using the Revised Perdew-Burke-Ernzerhof (RPBE) generalized gradient approximation (GGA) approach [20]. The super unit cell consisting of one Pt atom was made. The dimension was fixed to be 15 Å in both X and Y directions to avoid interactions between neighbor atomic chains. The dimension in the Z direction was varied from 2.17 to 3.57 Å in a step of 0.1 Å to calculate atomic distance dependence of binding energy. In the Brillouin zone of the supercell, the 1×1×30 k-point (Monkhorst-Pack k-point) are included in our calculation. Finally, the atomic distance dependence of binding energy for infinite chain was obtained by difference between the total energy of the infinite atomic chain and the energy of the isolate atom as follows [21]

$$E_{binding} = E_{total} - E_{isolated\ atom} \tag{4.5}$$

The calculated binding energy as a function of interatomic distance is shown in figure 4.7.

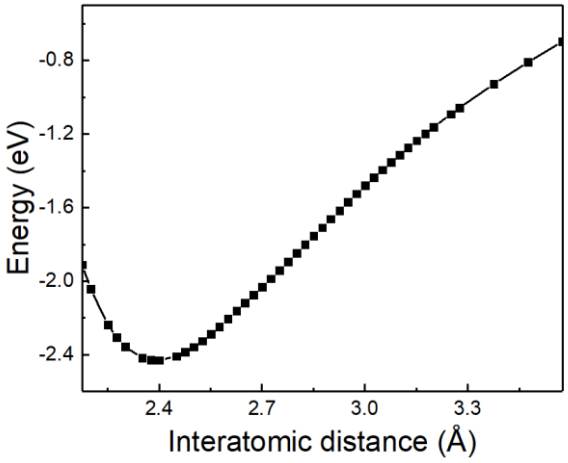

Figure 4.7 The calculated binding energy as a function of atomic distance for single Pt atomic chains.

Figure 4.8 shows the string tension calculated based on equation 4.5. The string tension have a minimum value when the interatomic distance is ~2.5 Å. Based on the theory of string tension, the stable structure occurred when the string tension is minimum, which is consistent with our experiment result. During the experiment, the chains are elongated from the stable structure of the chain which interatomic distance is ~2.5 Å up to 0.25 Å. So, the binding energy curve of the Pt atomic chains from 2.5 Å to 2.75 Å is fitted to a parabolic potential. The total energy was fitted to $E_{binding} = 0.82x^2 - 2.62x - 0.65$ with an R-squared value (coefficient of determination) of 99.98%. Figure 4.9 shows the fitting curve. It suggests that the binding energy can be expressed as parabolic function during the stretching. Therefore, the spring constant which can be calculated from the second derivative of energy is assumed to be constant during the stretching. It matches with our experiment result. The calculated spring constant value is 1.64 eV/Å^2 (26.24 N/m).

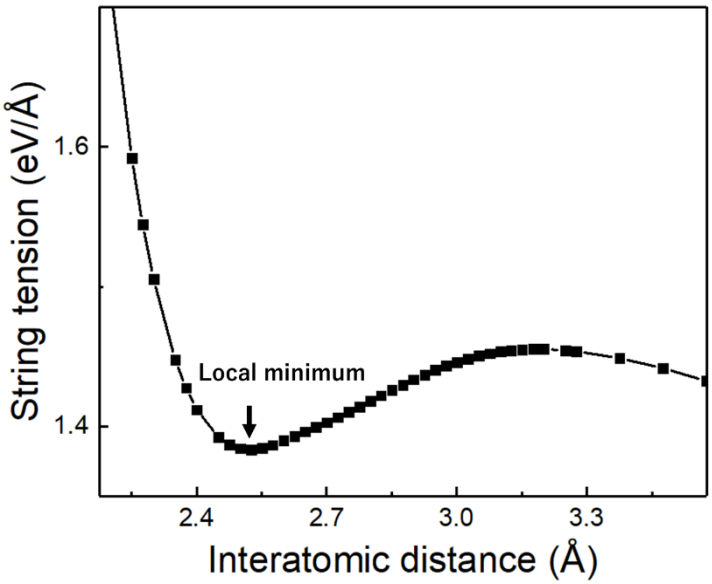

Figure 4.8 The calculated string tension as a function of atomic distance for single Pt atomic chains.

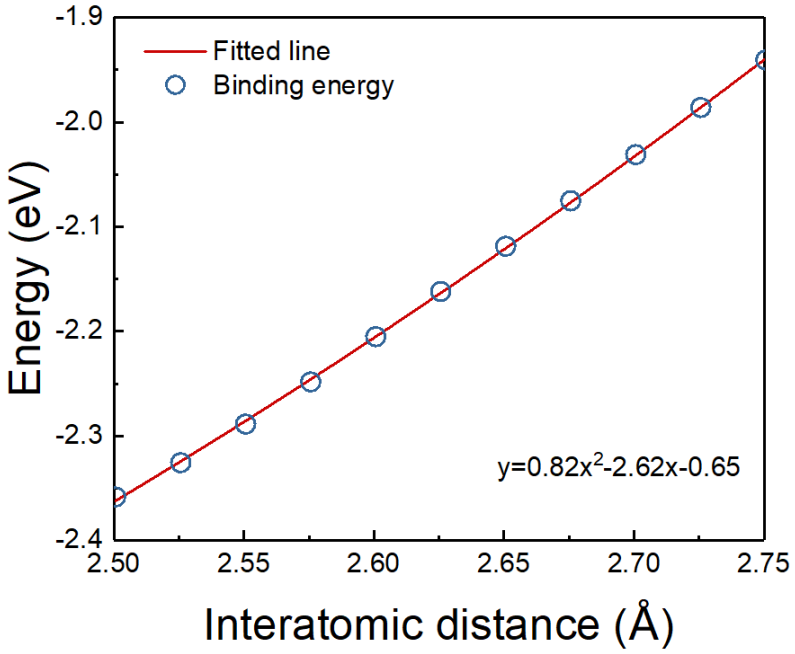

Figure 4.9 The fitting of the binding energy to a parabolic function

In addition, the theoretical breaking bond length when the string tension reaches to its barrier is 0.32 nm. To compare with the theoretical result, the breaking point of the atomic chains are also investigated. The elongations of monatomic chains can be calculated from the applied voltage on the piezo tube use the ratio mentions in chapter 3. The elongations of the monatomic chains at rupture are summarized in Figure 4.10. The breaking point seems scattered, which may be caused by accident rupture of the atomic chains. The maximum elongation distances are ~0.07nm, ~0.13nm, ~0.2nm and ~0.25nm for the chains with 2-5 atoms.

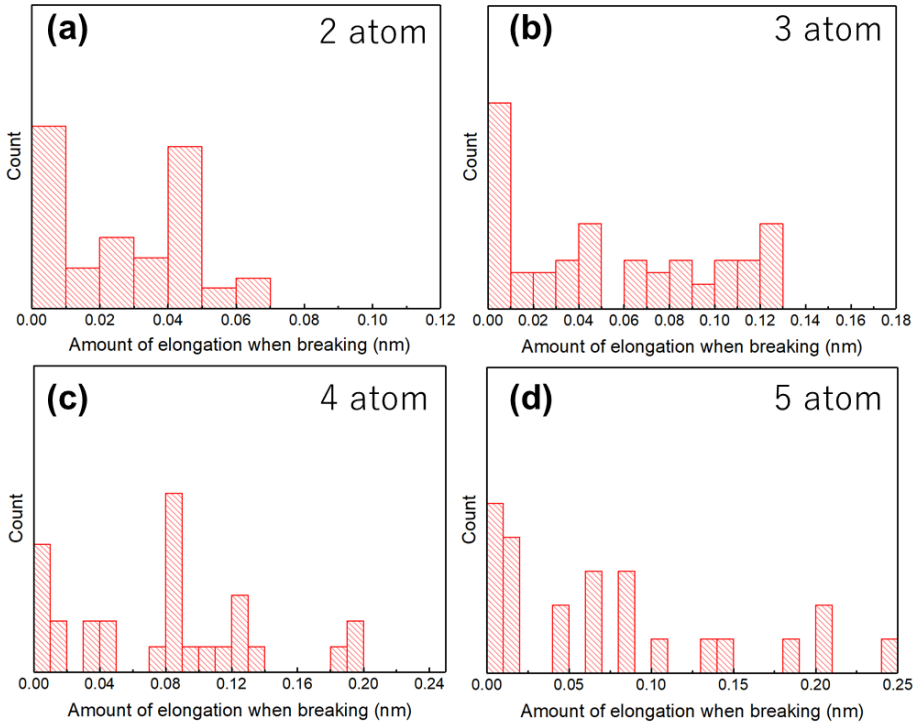

Figure 4.10 Elongation distance of the atomic chains when they are broken for chains with 2-5 atoms, respectively.

To calculate the breaking point of one bond in the monatomic chain, the ratio between of base spring constant and the chains spring constant are considered. The total elongation ($d_{total(i)}$, where i represents the number of constituent atoms in the chain) can be expressed by the sum of the elongations of the base (d_b), the bond between the edge atom of the base and the chain atom (d_{edge}) and the bond at the middle of the chain (d_{chain}),

$$d_{total(2)} = d_{edge} + d_{base} \tag{4.6}$$

$$d_{total(3)} = 2d_{edge} + d_{base} \tag{4.7}$$

$$d_{total(4)} = 2d_{edge} + d_{chain} + d_{base} \tag{4.8}$$

$$d_{total(5)} = 2d_{edge} + 2d_{chain} + d_{base} \tag{4.9}$$

The d_{base}, d_{edge} and d_{chain} have the following relationships:

$$\frac{d_{base}}{d_{edge}} = \frac{k_{edge}}{k_{base}} \tag{4.10}$$

$$\frac{d_{chain}}{d_{edge}} = \frac{k_{edge}}{k_{chain}} \tag{4.11}$$

The elongation of the monatomic chains can be calculated by combining equations (10) and (11) and assuming k_{chain}= 25 N/m, k_{edge}= 23 N/m and k_{base}= 90 N/m. Since the oscillation amplitude of LER is 0.027 nm, the calculated breaking points of single bond are shown in Table 4.1. The breaking point of single bond in the Pt monatomic chains is estimated to be approximately 0.31±0.02nm. This value is in agreement of breaking point when the string tension reaches to its barrier, where the

breaking point is 0.32 nm.

Table 4.1 The breaking point of the atomic chains and individual bonds in the chain

Number of atoms in a chain	Maximum breaking point of atomic chains (nm)	Breaking point for one bond (nm)
2	0.056 ± 0.021	0.305 ± 0.021
3	0.058 ± 0.011	0.308 ± 0.011
4	0.061 ± 0.008	0.311 ± 0.008
5	0.059 ± 0.006	0.309 ± 0.006

Previously, the string tension has been pointed out to be a critical parameter to determine the stable atomic configuration in one-dimensional materials. However, these studies remained on the theoretical side. The present study is valuable in showing that string tension is an important parameter by precise measurement of the bond spring constant, the excellent agreement of the bond length, spring constant and the breaking point with the experiment support the string tension in the Pt atomic chains. In the future, it is necessary to include the effect of string tension in understanding the physical or chemical properties of one-dimensional system. Alternatively, we can expect to find new physical properties in one-dimensional system by including the effect of string tension [22-24].

4.4 Conclusion

In this chapter, we investigated the mechanical properties of single Pt atomic chains. During stretching the nanocontact, it becomes thinner and thinner and finally becomes a single atomic chains. The structures of the atomic chains and base supporting it can be identified with the TEM images combined with the conductance value. The conductance of single atomic chains is about $1.7G_0$. *In situ* TEM images confirmed the formation of one-dimensional Pt atom chains—consisting of two, three, four, or five atoms—between Pt bases with equivalent shapes. The spring constant and electrical conductance of the chains were measured concurrently during TEM observation, and both were found to remain unchanged throughout each elastic stretching stage.

By eliminating the spring constant of the bases, the bond spring constant between two atoms in the chain was estimated to be approximately 25 N/m; regardless of the chain length. The experimental results show good agreement with the theoretical calculation of the string tension. The results indicate that the string tension plays an important role in the structure properties of the one-dimensional atomic chains. The concept of string tension is a key to understand the physical or chemical properties of one-dimensional system or fabricated new functional one-dimensional materials.

References

[1] J. N. Armstrong, S. Z. Hua, and H. D. Chopra, Mechanics of Quantum and Sharvin Conductors, Physical Review B 83, 235422 (2011).

[2] T. Shiota, A. I. Mares, A. M. C. Valkering, T. H. Oosterkamp, and J. M. van Ruitenbeek, Mechanical Properties of Pt Monatomic Chains, Phys. Rev. B 77, 125411 (2008).

[3] K. Ishizuka, M. Tomitori, T. Arai, and Y. Oshima, Mechanical Analysis of Gold Nanocontacts during Stretching Using an In-Situ Transmission Electron Microscope Equipped with a Force Sensor, Appl. Phys. Express 13, 025001 (2020).

[4] J. Zhang, K. Ishizuka, M. Tomitori, T. Arai, and Y. Oshima, Atomic Scale Mechanics Explored by in Situ Transmission Electron Microscopy with a Quartz Length-Extension Resonator as a Force Sensor, Nanotechnology 31, 205706 (2020).

[5] R. H. M. Smit, C. Untiedt, A. I. Yanson, and J. M. van Ruitenbeek, Common Origin for Surface Reconstruction and the Formation of Chains of Metal Atoms, Phys. Rev. Lett. 87, 266102 (2001).

[6] M. R. Calvo, C. Sabater, W. Dednam, E. B. Lombardi, M. J. Caturla, and C. Untiedt, Influence of Relativistic Effects on the Contact Formation of

Transition Metals, Phys. Rev. Lett. 120, 076802 (2018).

[7] E. Yu. Zarechnaya, N. V. Skorodumova, S. I. Simak, B. Johansson, and E. I. Isaev, Theoretical Study of Linear Monoatomic Nanowires, Dimer and Bulk of Cu, Ag, Au, Ni, Pd and Pt, Computational Materials Science 43, 522 (2008).

[8] R. H. M. Smit, C. Untiedt, G. Rubio-Bollinger, R. C. Segers, and J. M. van Ruitenbeek, Observation of a Parity Oscillation in the Conductance of Atomic Wires, Phys. Rev. Lett. 91, 076805 (2003).

[9] V. M. García-Suárez, A. R. Rocha, S. W. Bailey, C. J. Lambert, S. Sanvito, and J. Ferrer, Conductance Oscillations in Zigzag Platinum Chains, Phys. Rev. Lett. 95, 256804 (2005).

[10] M. Kumar, O. Tal, R. H. M. Smit, A. Smogunov, E. Tosatti, and J. M. van Ruitenbeek, Shot Noise and Magnetism of Pt Atomic Chains: Accumulation of Points at the Boundary, Physical Review B 88, (2013).

[11] J. Comtet, A. Lainé, A. Niguès, L. Bocquet, and A. Siria, Atomic Rheology of Gold Nanojunctions, Nature 569, 393 (2019).

[12] T. N. Todorov, J. Hoekstra, and A. P. Sutton, Current-Induced Embrittlement of Atomic Wires, Phys. Rev. Lett. 86, 3606 (2001).

[13] F. Picaud, A. D. Corso, and E. Tosatti, Phonons Softening in Tip-Stretched Monatomic Nanowires, Surface Science 532–535, 544 (2003).

[14] S. R. Bahn and K. W. Jacobsen, Chain Formation of Metal Atoms, Phys. Rev. Lett. 87, 266101 (2001).

[15] E. Tosatti, S. Prestipino, S. Kostlmeier, A. D. Corso, and F. D. Di Tolla, String Tension and Stability of Magic Tip-Suspended Nanowires, Science 291, 288 (2001).

[16] E. Tosatti, Nanowire Formation at Metal–Metal Contacts, Solid State Communications 135, 610 (2005).

[17] B. Delley, An All-electron Numerical Method for Solving the Local Density Functional for Polyatomic Molecules, J. Chem. Phys. 92, 508 (1990).

[18] B. Delley, From Molecules to Solids with the DMol3 Approach, J. Chem. Phys. 113, 7756 (2000).

[19] B. Delley, Hardness Conserving Semilocal Pseudopotentials, Phys. Rev. B 66, 155125 (2002).

[20] B. Hammer, L. B. Hansen, and J. K. Nørskov, Improved Adsorption Energetics within Density-Functional Theory Using Revised Perdew-Burke-Ernzerhof Functionals, Phys. Rev. B 59, 7413 (1999).

[21] J. H. Rose, J. Ferrante, and J. R. Smith, Universal Binding Energy Curves for Metals and Bimetallic Interfaces, Phys. Rev. Lett. 47, 675 (1981).

[22] A. Smogunov, A. Dal Corso, A. Delin, R. Weht, and E. Tosatti, Colossal

Magnetic Anisotropy of Monatomic Free and Deposited Platinum Nanowires, Nature Nanotech 3, 22 (2008).

[23] F. Strigl, C. Espy, M. Bückle, E. Scheer, and T. Pietsch, Emerging Magnetic Order in Platinum Atomic Contacts and Chains, Nat. Commun. 6, (2015).

[24] A. Delin and E. Tosatti, Magnetic Phenomena in 5 d Transition Metal Nanowires, Phys. Rev. B 68, 144434 (2003).

Chapter 5 Mechanical properties of sub-2nm Au nanocontacts

Introduction

This chapter contains the measurement of the deformation process and mechanicial properties of Au nanocontacts under different orientations. Young's modulus of Au [111] nanocontacts is calculated by removing the contribution of the base part and the mechanism of the mechanical properties are discussed.

In Chapter 5.1, we show the deformation process of Au nanocontacts along the [110] direction. In Chapter 5.2, we show the deformation process of Au nanocontacts along the [111] direction. In Chapter 5.3, we discussed the Young's modulus of Au nanocontacts along the [111] direction.

5.1 Deformation process of sub-2nm Au nanocontact along [110] direction

Figure 5.1 shows a typical TEM image of an Au nanocontact along the [110] direction [1-3]. The diameter of the nanocontact is around 1.7nm and the length is around 1nm. Similar with the previous report, the main feature of the [110] contact is that the diameter of the contact area is uniform [1,3]. The direction of the nanocontact can be also confirmed from the FFT patterns as shown in figure 5.1b.

Detail of the structure of the nanocontact can be identified from our HR-TEM images. Here we show an example as shown in figure 5.1c, which is enlargement of the contact area in figure 5.1a. The structure model analyzed from figure 5.1c is present in figure 5.1d. The dark dots in the TEM images correspond to the [110] gold atomic rows as marked in yellow dots in figure 5.1d. The [110] gold atomic rows are parallel to the direction of the incident electron beam. The proposed structure model is shown as the inset in figure 5.1d, indicating that this nanocontact have 9 (100) planes perpendicular to the contact direction. And the length of the nanocontact contains 8 (110) planes.

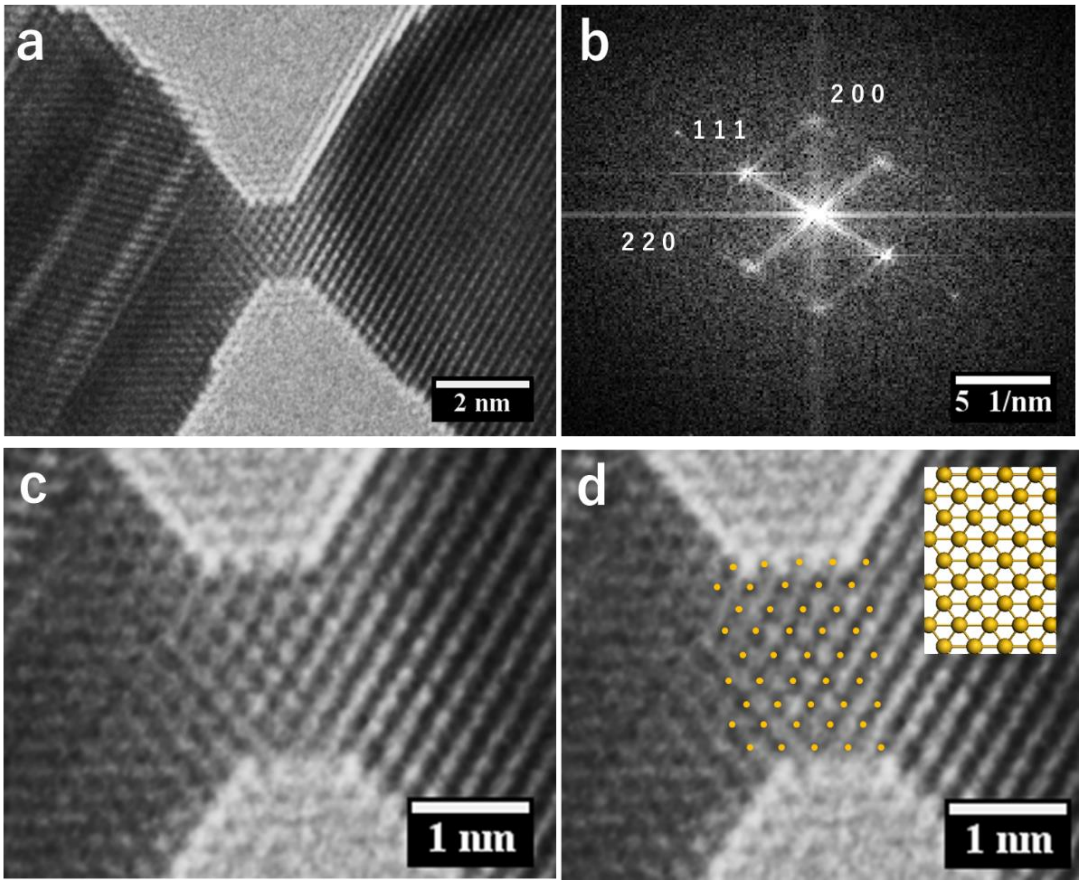

Figure 5.1 (a) TEM image of a [110] nanocontact. (b). FFT pattern of figure 5.1a, which shows the nanocontact is parallel to the [110] direction of the crystal. (c) Enlargement of the contact area. (d) The yellow dots represent [011] atomic columns along the incident electron beam direction. And the inset shows the structure model.

After the nanocontact was fabricated, it was further stretched to exam its deformation process and mechanical properties. A series of TEM images of the deformation process of the [110] nanocontact and it corresponding conductance and spring constant value are shown in figure 5.2. The deformation of thick metal wires

with uniform diameter usually have a necking process where large amounts of strain is localized in a small region of the material causes a local deformation to form a narrower neck. Such process is also observed in the Au nanowires which have the diameter of ~20nm and ~100nm in the previous report [4,5].

Different with the bulk crystal and nanowires with diameters ranging from tens of nanometers, the deformation process of [110] nanocontacts didn't have such necking process. From figure 5.2c, it is clearly that the diameter of Au [110] contact kept uniform when stretching it. Instead of necking, the total diameter of the nanocontact is reduced during the deformation process. It suggests that when the sub-2mn [110] nanocontact is stretched and thinned, the hole [110] atomic rows in the contact that parallel to the contact direction disappear. The deformation process can also be revealed from the conductance variations as shown in figure 5.2a. During stretching, the conductance shows stepwise decreased, which shows plateaus and sudden drops in the conductance traces. The conductance value is proportional to the cross sectional area of the narrowest part [6]. In Au [110] nanocontacts, the conductance value can be reflecting its diameters since their diameter are the same. So, the conductance variation behavior reveals that the deformation process of [110] contact is occurring alternately by elastic deformation and plastic deformation. The plateaus in conductance traces indicates the elastic deformation since the diameter is constant and the sudden decrease

corresponds to the plastic deformation which indicate the diameter suddenly shrink. The spring constant shows gradually decrease separated by some sudden drops and subsequent recovers. The sudden drops usually occurred at the moment of conductance changes. After the sudden drop of the spring constant, it will recover to a value which is smaller than the value before the drop.

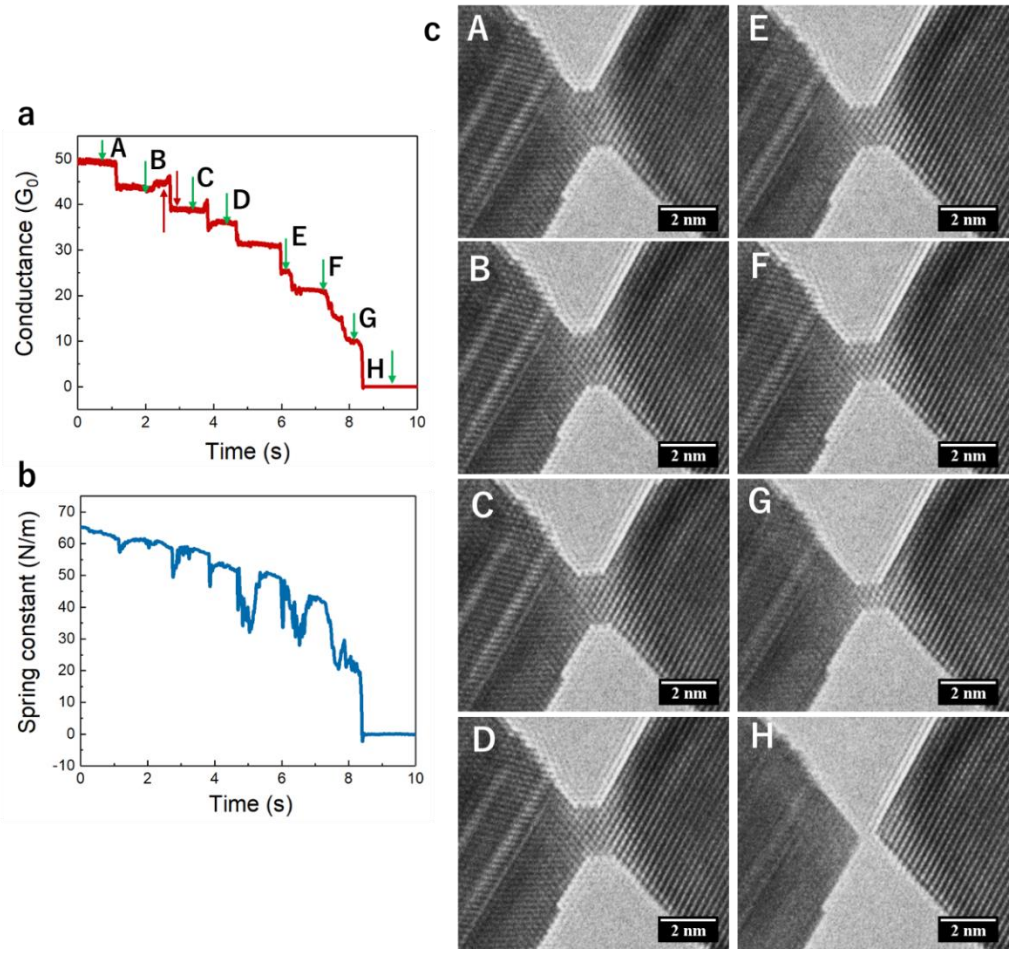

Figure 5.2 (a) conductance value of [110] nanocontact during stretching. (b). spring constant value of [110] nanocontact during stretching. (c) TEM images captured during stretching process at the moment indicated in (a).

In addition, from figure 5.2c, the nanocontact almost kept a constant length while its diameter continuously decreased during stretching it. This phenomenon is quite unique and interesting and never been reported. To further analysis the deformation process of the [110] nanocontact, the HR-TEM images are further analyzed as shown in figure 5.3, where the left figure shows the contact before the deformation and the right figure, just after the deformation as indicated as the red arrow in figure 5.2a.

For the nanocontact before deformation, there are 11 atomic rows along the contact direction and length in 3 atomic rows. After the deformation, the nanocontact becomes 10 atomic rows along the contact direction and length keeps constant. From our observation, the deformation mechanism is explained as the model shown in figure 5.3. When the nanocontact was stretched, the elastic deformation occurred first and the conductance in this region kept constant. When further stretched the nanocontacts, a plastic deformation occurred so that the nanocontact was thinned by the slip along the (111) planes in the contact as indicated in the lower models of figure 5.3. The diameter becomes smaller due to the slip while the length of the nanocontacts still keeps constant.

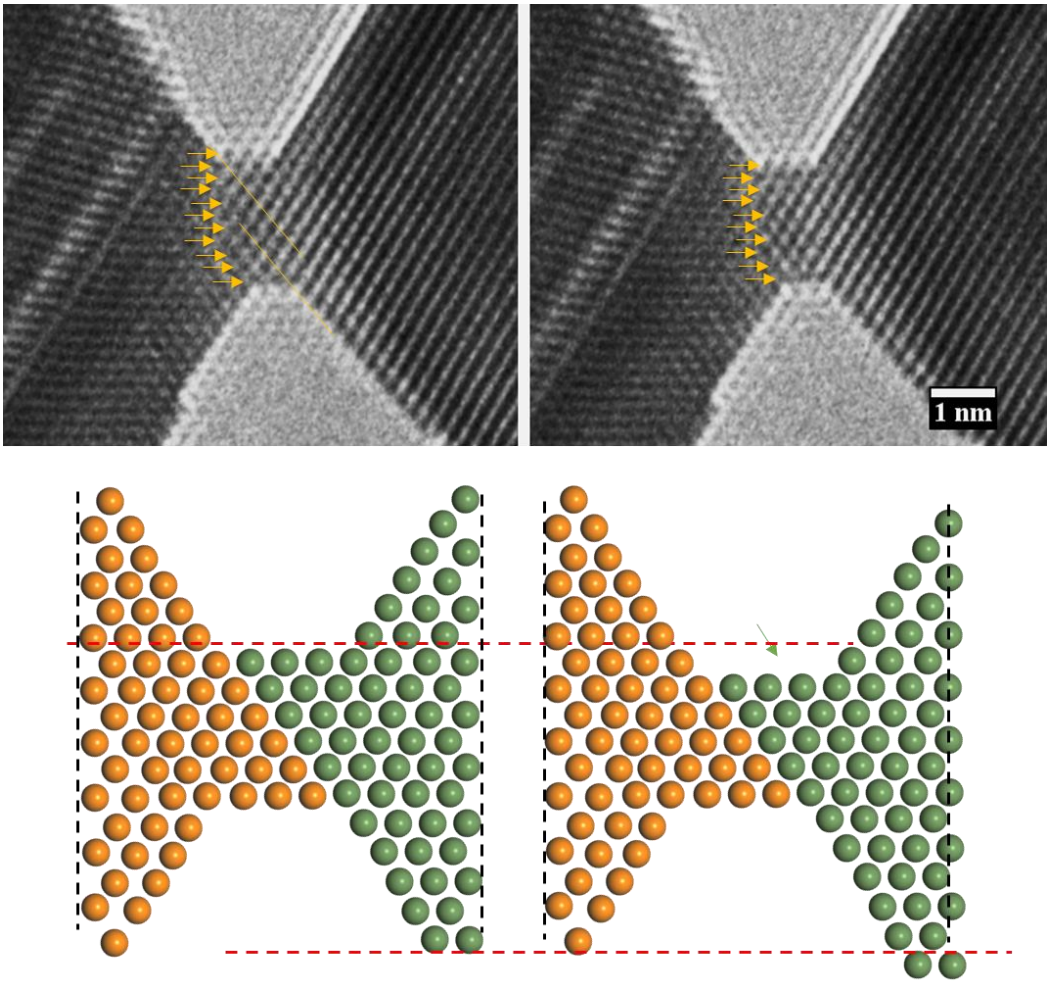

Figure 5.3 TEM images of an Au [110] nanocontact before (left) and after deformation (right). The lower shows the model of the deformation process of the Au [110] nanocontact.

5.2 Deformation process of Au nanocontact along [111] direction

Atomic scale deformation process and the corresponding conductance and spring constant of the Au nanocontacts are captured in figures 5.4, we respectively show the typical variations in spring constant, conductance and corresponding TEM images

when the nanocontact is continuously thinned by stretching. The variations in the conductance is different from that of the [110] contact. When the nanocontacts are stretched, the nanocontacts gradually becomes thinner, its conductance and spring constant gradually decrease as shown in Figure 5.4a and b. The spring constant value sometimes suddenly drops to a small value and subsequently recovered. However, we cannot obtain the correlation between this sudden drops and the TEM image since the sudden drop only lasts for a very short time, which is not enough to capture the clear TEM images. These sudden drops are also observed in the deformation process of the Pt nanocontacts and Au [110] nanocontacts, which can be explained by rearrangement of the atomic structure after the plastic deformation [7]. These sudden drops are usually occurred with the beginning point of the stepwise change in the conductance, indicate the atom rearrangement occurred after the plastic deformation occurred. Figure 1c shows the TEM image at the corresponding moment shown in figures 5.4a and b. The Au [111] nanocontact shows a typical shape of a narrow neck formed by the connection of two cone shape Au tips. From the TEM image and the videos, the narrowest part of the junction becomes thinner during stretching while the apex angles of the cone shape didn't change as the dash line indicated in the figures. The conductance is ~$5G_0$ and spring constant is ~19N/m before the rupture of the nanocontact.

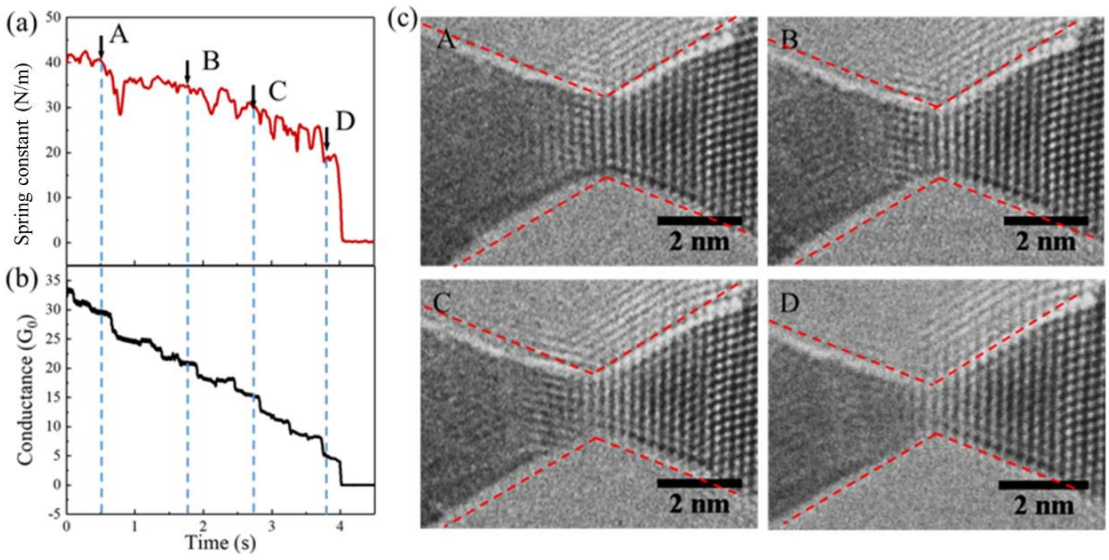

Figure 5.4 (a), (b). Typical variations of conductance, stiffness for Au nanocontacts during stretching. The stretching direction is the horizontal direction of the picture. (c). Corresponding TEM images captured at moments A, B, C, and D arrowed in a and b.

To further analysis the shape of the nanocontact, we analyzed the TEM images with different conductance values. Here we assume the cross section of the narrowest part of the contact is circle in shape and the diameter can be directly measured in the corresponding TEM images. To confirm this assumption, we investigate the conduction as a function of the narrowest cross sectional area of the contact. As shown in figure 5.5, the measured conductance value is proportional to the cross-sectional area up to $45G_0$. Furthermore, this linear relationship was in agreement with the Sharvin formula [8].

$$G = G_0{}^{*}\pi S/\lambda_f^2 \tag{5.1}$$

where S is the cross-sectional area and λ_f is the electron Fermi wavelength (=0.52 nm for gold). This result indicates that the Au contact is a ballistic conductor up to a conductance of 45 G_0, also indicate our assumption is reasonable.

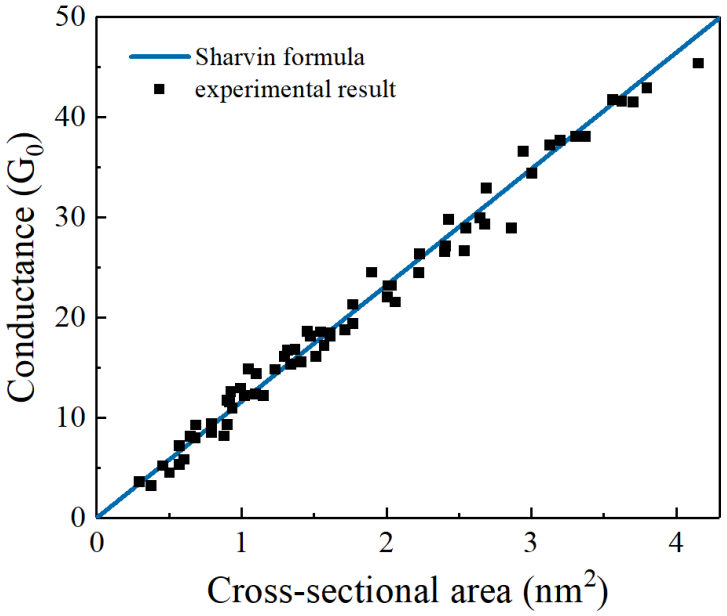

Figure 5.5 Conductance as a function of cross-sectional area of the narrowest part of the nanocontacts, if we assume the cross-section of the nanocontact is round, and the diameter is measured in the TEM images.

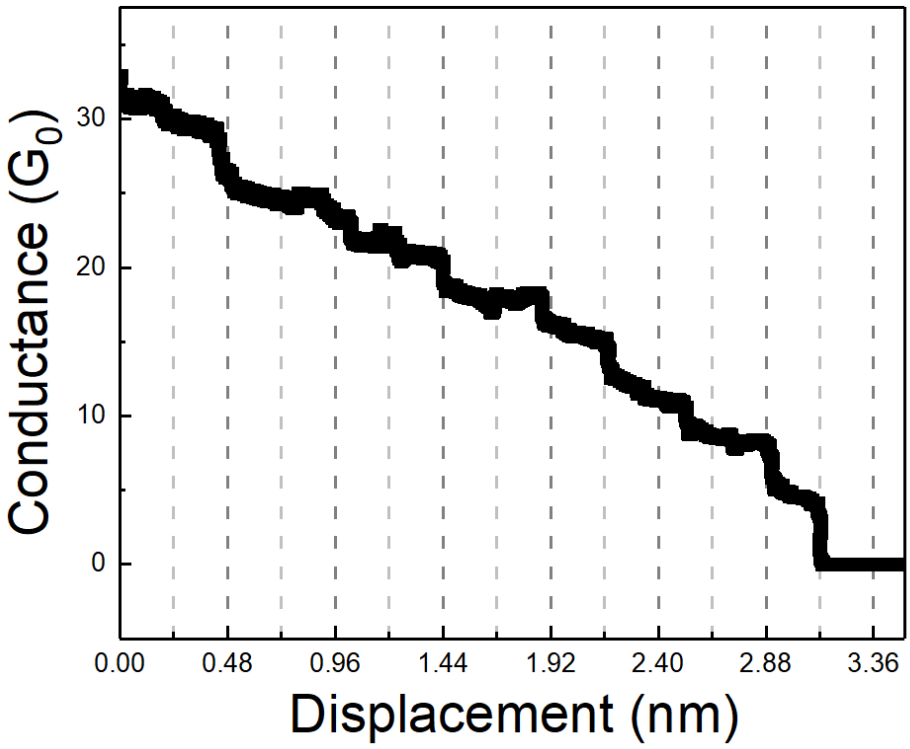

Figure 5.6 Conductance as a function of electrode displacement during stretching of a gold [111] contact. The gradual decrease and abrupt jumps correspond to elastic and plastic deformations, respectively.

To further analyses the deformation process of Au nanocontact, conductance as a function of stretching distance is shown in figure 5.6. When stretching, conductance stepwise changes and it gradually decreased between steps. Among them, there are some big steps and small steps. The big steps and small steps appeared alternatively marked at the moment marked in dark and light gray dashed line. We found that the conductance value is almost constant between the small steps while it changes rapidly when big steps appeared. In addition, the steps usually appeared when the contacts were

stretched by approximately 0.24 nm, which corresponds to the spacing of the (111) lattice.

As we have mentions above, the apex angles of the cone kept constant when the contacts were stretched. It indicates that the number of atoms are not constant so that such angle can be maintained. From the TEM images (figure 5.7a-f), we can observe the surface atoms are not stable and seem to easily migrate. The similar surface diffusion process is also observed in the gold [112] nanowires from the previous papers [9,10]. However, the mechanism of the [111] contact is different from the previous observed [112] contact. The previous report of the [112] contact shows the surface atoms move away from the contact area, while the surface atoms in our [111] contact move to the contact area. From the TEM images and videos which shows the upper side of the nanocontact in our [111] contact, we can clearly see the surface atoms disappeared one by one from the side far away from contact and the other atoms still maintained in a gold FCC structure. It indicates the surface atoms are migrating to the contact part to maintain the apex angles of the cone shape when a nanocontact is stretched. The similar migration of the surface atoms is also observed on the down side of the nanocontact. Combined with the above observation and change behavior of electrical conductance during stretching, the atomic scale deformation process of the stretched nanocontact is shown in figure 5.7 (g), where the green and yellow atoms

present the surface and inter atoms, respectively. When the nanocontact is stretched, the narrowest part of the contact is easily deformed and thinned. At the same time, the surface atoms migrate to the narrowest part of contact and form a new atomic plane due to the high mobility of the surface atoms. When the narrowest part contains one atomic plane, the new atomic plane will have the almost same size with the narrowest one, which corresponding to the small steps in the conductance evolution. Then after further stretching, the next new atomic plane will have a smaller size, corresponding to the big steps in the conductance evolution. Due to the unique deformation process of the Au [111] nanocontact, the apex angles of the cone shape can be kept. The surfaces of the [111] contacts are mainly (111) surface, which is the close packed plane of FCC crystal and have the lowest surface energy. Maintaining a complete (111) surface is contribute to the stability of contact [11].

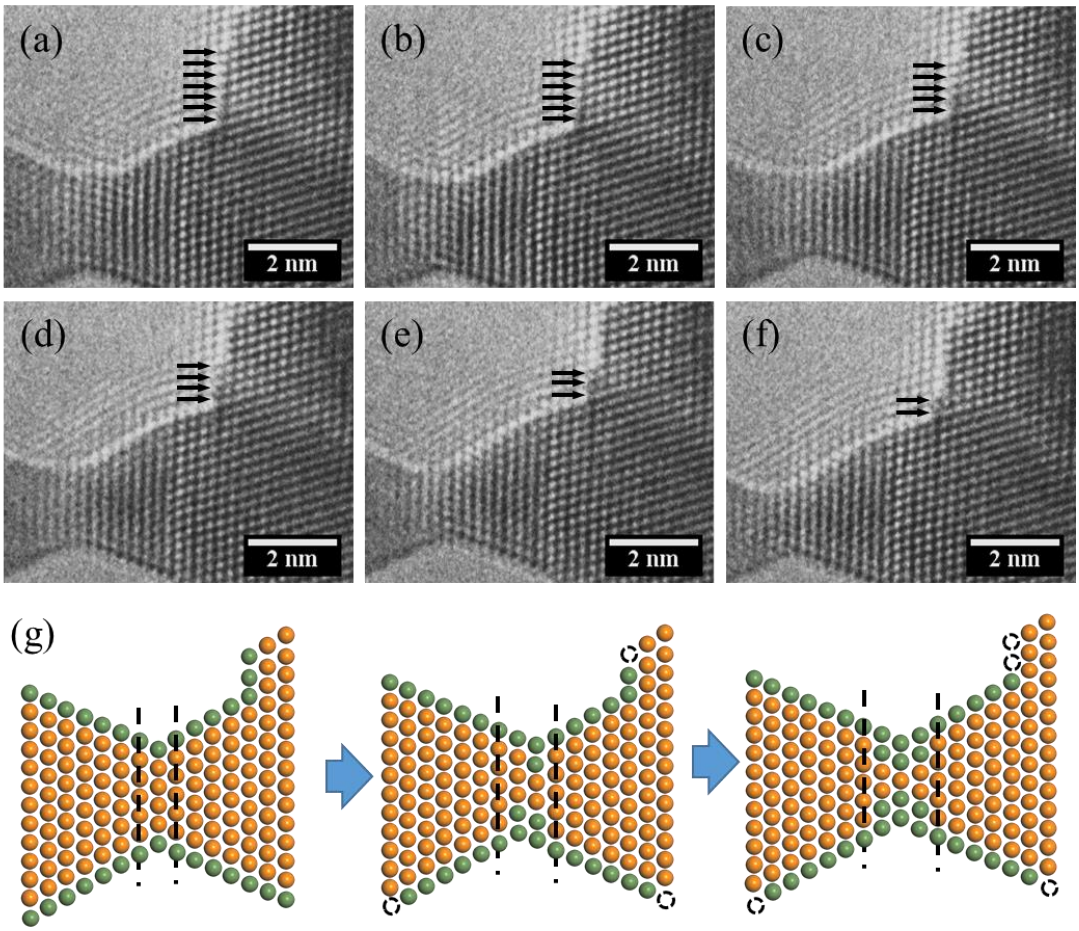

Figure 5.7 (a-f). TEM images of the nanocontact and connected base part during the stretching, the stretching direction is the horizontal direction of the picture. (g). The proposed atomic scale deformation mechanism of the Au [111] nanocontacts.

Obviously, the deformation mechanism between the [110] and [111] contact is different, such difference may come from the (111) planes. In our opinion, since the (111) plane is the close packed plane and the most stable plane in FCC crystal, it is more difficult to destroy this plane. The sliding between (111) is easier occurred rather than destroy it. For [110] contact, the (111) planes have an angle of about 55 degrees

with the contact direction. So during stretching, the sliding along the (111) plane is easily occurred. However, for the [111] contact, the [111] plane is perpendicular to the contact direction. So during stretching, the surface atom migration contributes to the deformation of the contact.

5.3 Size-dependence Young's modulus of Au nanocontact along [111] direction

The size effect on the Young's modulus of Au [111] nanocontacts is further investigated. The Young's modulus (Y) can be expressed as the ratio between the elastic strain ($\delta, = \frac{F}{A}$, where F is the applied force and A is the cross-sectional area) and stress ($\varepsilon, = \frac{\Delta l}{l}$, where Δl is the amount of elongation and l is the length) simply shown as below.

$$Y = \frac{\delta}{\varepsilon} = \frac{Fl}{A\Delta l} \tag{5.2}$$

Since the applied force can be expressed by the spring constant of the materials, which is $F = k\Delta l$, the Young's modulus of the materials can be expressed by:

$$Y = \frac{kl}{A} \tag{5.3}$$

Which indicate the Young's modulus of the materials can be calculated from its spring constant and dimensions. We should notice that our measured stiffness value is the total value including all the materials connected between the LER and the fixed counter electrode. The contribution of the other part should be excluded to clarify the

size dependence of the mechanical properties [12]. Here we propose a model to calculate the Young's modulus under the different diameter as shown in figure 5.7. Here we use the size and stiffness data of a nanocontact before and after being stretched. As we mentioned above, the apex angle of the cone kept constant after the contact was stretched. It indicates that an additional plane was inserted into the contact as shown in figure 5.8. If we assume the nanocontact before deformation as the base contact, the measured stiffness ($k_{measure1}$) can be expressed as:

$$\frac{1}{k_{measure1}} = \frac{1}{k_{base}} \tag{5.4}$$

Where k_{base} is the stiffness of the base part. After the nanocontact is stretched, the total stiffness is reduced due to the insert of the new atomic layer. Then the measured stiffness ($k_{measure2}$) becomes:

$$\frac{1}{k_{measure2}} = \frac{1}{k_{disk}} + \frac{1}{k_{base}} \tag{5.5}$$

Where k_{disk} is the stiffness of the inserted disk-like shaped atom layer. Then by taking the difference between equation 5.4 and equation 5.5, the stiffness of the such disk can be calculated as:

$$k_{disk} = \frac{k_{measure1}k_{measure2}}{k_{measure1}-k_{measure2}} \tag{5.6}$$

The elongation (l) of the nanocontact, corresponding to the length of the disk, was almost the same with the spacing of the (111) lattice (0.24 nm). The cross-sectional area of the disk can be calculated from the conductance through the Sharvin formula. The

Young's modulus can be obtained as follows:

$$Y_{disk} = \frac{k_{measure1}k_{measure2}}{k_{measure1}-k_{measure2}} \times \frac{l}{A} \tag{5.7}$$

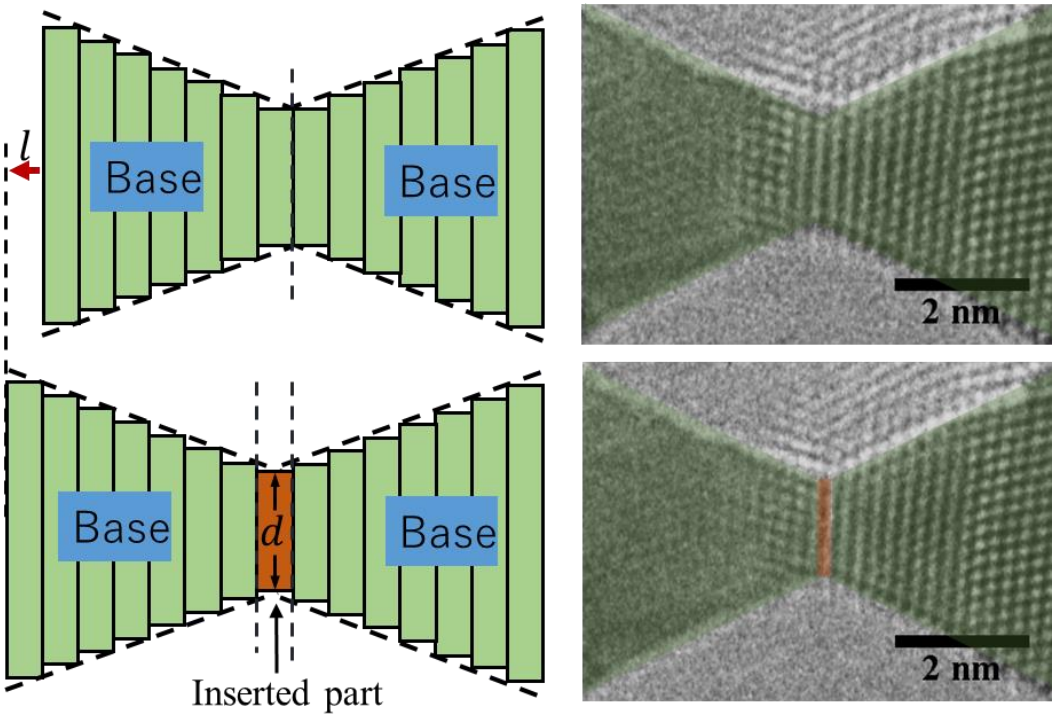

Figure 5.8 Model of the Au [111] nanocontact which separate it to several nanodisks. The Young's modulus of the narrowest nanodisk can be calculate from this model.

To explore the size effect on the disk, we have calculated the Young's modulus of the disks ranged from $5G_0$ to $40G_0$ in conductance, which is corresponding to a cross-sectional area from 0.43 to 3.4 nm^2. The Young's modulus as a function of diameter is shown in figure 5.9. The Young's modulus value shows a little scattered, which mainly come from the measurement error of the size of the disk. In addition, the size

dependence of the Young's modulus of the Au [111] disk is obtained, showing that the Young's modulus gradually reduce with reducing the diameter. The Young's modulus is about 80Gpa when the conductance is about $40G_0$ and it reduce to around 20Gpa when the conductance reduce to $5G_0$. These value are smaller than the theoretical value along the [111] direction, which is about 116 GPa [13].

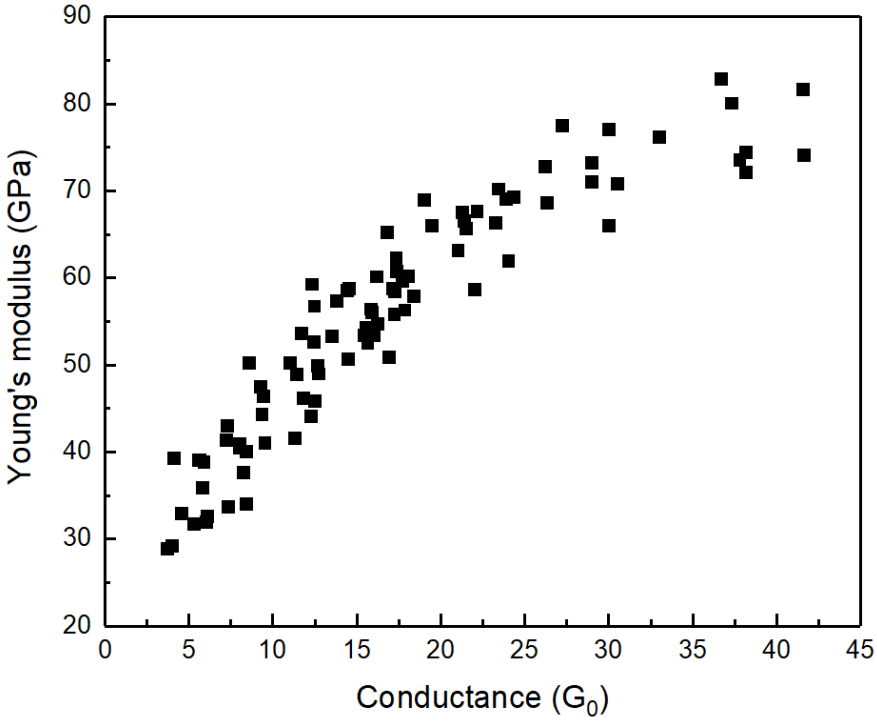

Figure 5.9 The variation of Young's modulus with conductance of the Au (111) disk.

For metal nanomaterials, the surface to volume ratio is quite high, it is common that the surface and core parts of the nanomaterials has different physical properties, the Young's modulus of the surface part and core parts are considered to be different since

the surface atoms have lower coordination numbers than the core part [14,15]. In this sense, here we assume the surface atom layer, sub-surface atom layer and the core have the different Young's modulus, which is $Y_{surface}$, $Y_{sub-surface}$, Y_{core}, respectively. The Young's modulus of the disk (Y_{disk}) is:

$$Y_{disk} = Y_{core}\frac{A_{core}}{A_{disk}} + Y_{sub-surface}\frac{A_{sub-surface}}{A_{disk}} + Y_{surface}\frac{A_{surface}}{A_{disk}} \qquad (5.8)$$

where the A_{core}, $A_{sub-surface}$, $A_{surface}$, A_{disk} is the cross-sectional area of the core part, sub-surface layer, surface layer and the whole disk, respectively. The cross-sectional area of each part is calculated from the corresponding atomic configurations, which is obtained by combine the TEM images and conductance of the nanocontacts. For example, the nanocontacts shown in figure 5.4(c) have a conductance of about 30, 21.3, 15.6 and 4.6G_0, which cross-sectional areas are estimated to be about 2.58, 1.83, 1.34, 0.4nm^2, respectively, based on Sharvin formula. If we assume that the area occupied by one atom in a {111} crystal plane is 0.051nm^2, the minimum cross-section of these contact include 51, 36, 26 and 7atoms, respectively. Since the nanocontact has 8, 7, 6, and 3 [110] atomic rows, the atomic configuration of the nanocontact can be assumed to be the structure having the highest symmetry as shown in the figure 5.10[3]. Then the number of atoms in surface atom layer, sub-surface layer and the core can be counted, as shown as the atoms with blue, green and yellow colors in figure 5.10.

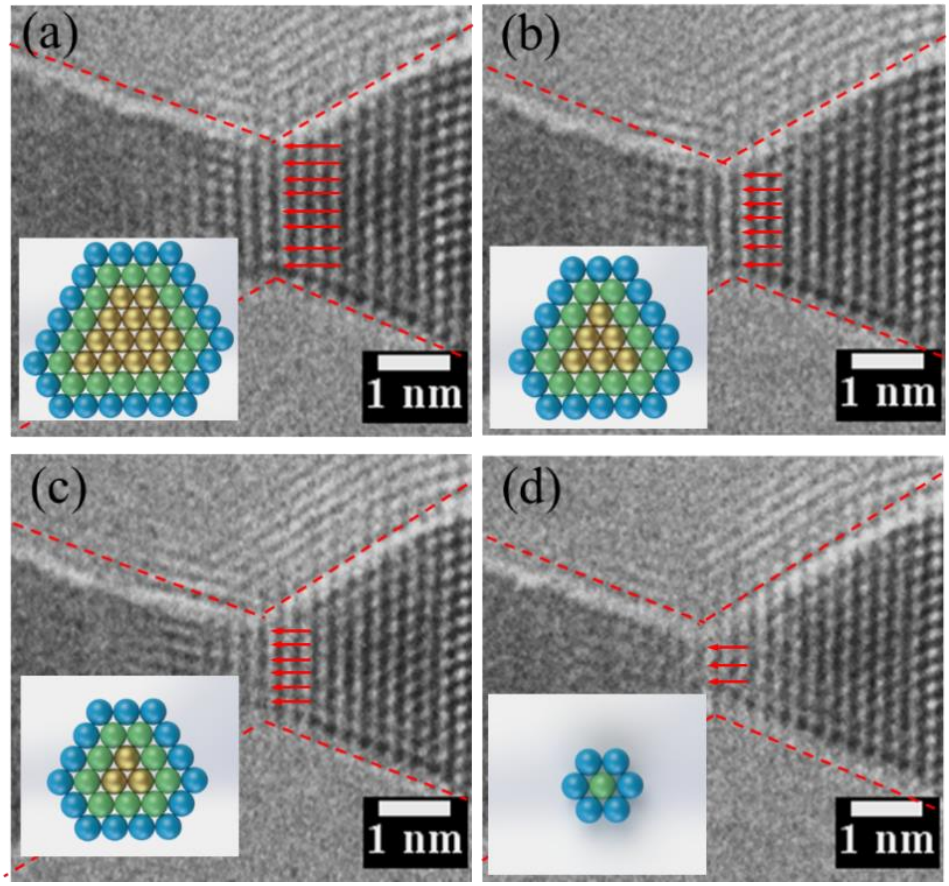

Figure 5.10 TEM images and atomic configurations of the minimum cross section captured at moments A, B, C, and D arrowed in figure 5.4 a.

Then our experimental data can be fitted by equation (5.8) as shown by the blue dots in figure 5.11. By fitting, we obtain that Y_{core} is 130.2Gpa, $Y_{sub-surface}$ is 93.3GPa and $Y_{surface}$ is 22.2Gpa. The fitted Young's modulus of the core part is slightly higher than that of the bulk [111] crystal, which is expected to be 116 GPa in theoretical calculation [16], while the Young's modulus of sub-surface is similar to the bulk one. However, the Young's modulus of the shell part is quite low compared with

the other parts.

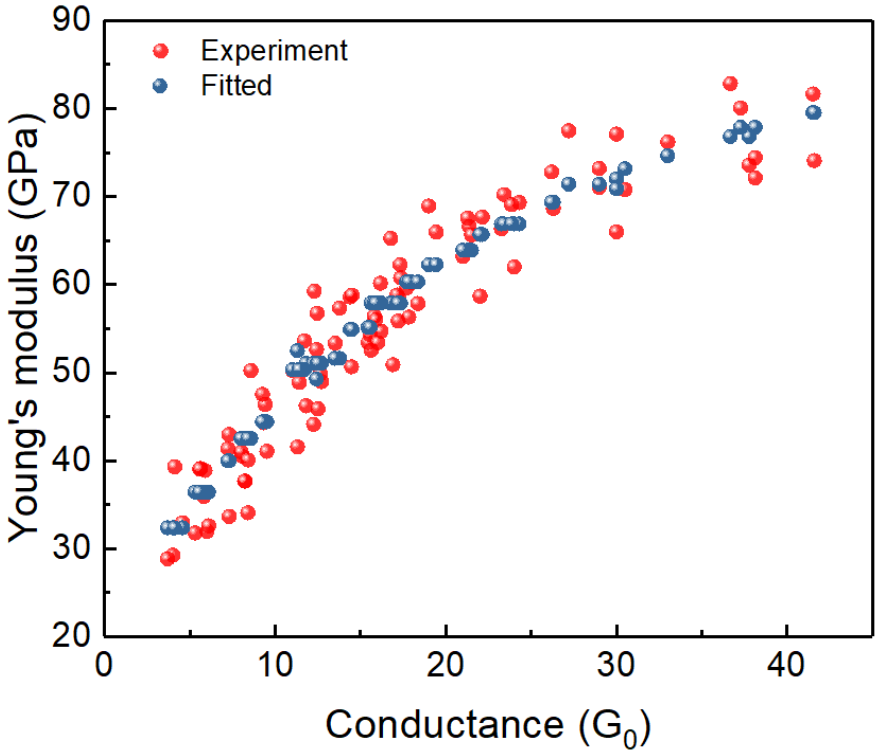

Figure 5.11 The variation of Young's modulus with conductance of the Au nanodisks. The red dots are experiment result and the red dots are the fitting one with equation (5.8)

The higher Young's modulus of the core part may be related to contraction due to inner pressure, since the disk is quite small in radius. It is evident by our measured distance between the (111) planes. As shown in the figure 5.12, the measured distance between the two (111) spot in the FFT pattern is 8.3 1/nm for the bulk part and 8.7 1/nm for the contact part, corresponding to 2.4 Å and 2.3 Å in period, respectively. Such

contraction may lead to slight increase of the Young's modulus. Such contraction would be negligible in the nanomaterial which is over tens of nanometers in diameter. And the total Young's modulus will be almost recovered to the bulk value since the contribution of the surface atoms is also reduced due to increasing the size. There are several experiment results support our idea. Seo et al obtained Young's modulus of 72GPa for Au [110] nanowire with about 100nm in diameter, which was close to the theoretical value [4]. Wu et al, obtained the almost constant Young's modulus which was compatible to the bulk value for Au nanowires ranging from 40-250nm in diameter [17]. These result shows similar Young's modulus values compared to the bulk one that support our idea. In addition, the small Young's modulus of the surface atomic layer supported our above observations that the surface atoms were easily migrated and the deformation of Au contact was assisted by such migration.

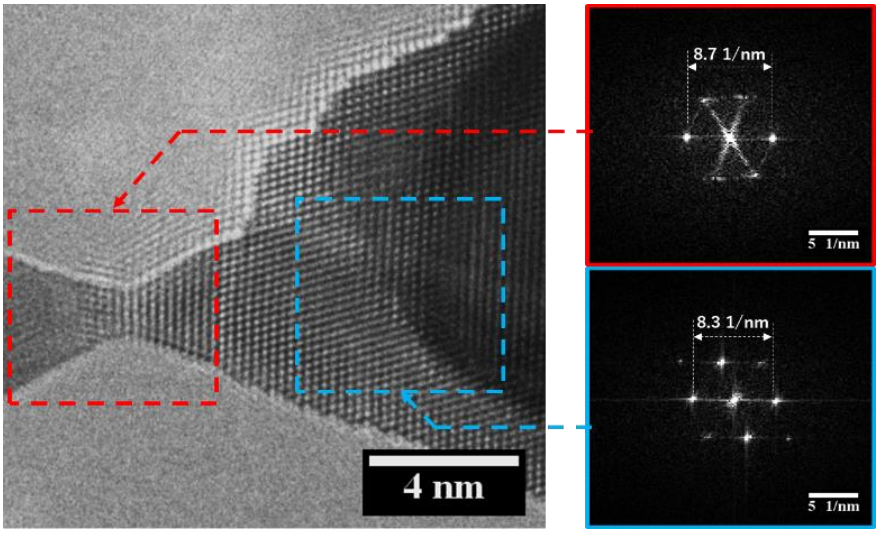

Figure 5.12 TEM images of an Au [111] contact with base part and corresponding FFT patterns of the contact part and the bulk part. The FFT pattern in the red frame is obtained from the contact part and the one in the blue frame is obtained from the bulk part.

The previous research indicated that the Young's modulus of the nanomaterials linearly decreased with increasing the temperature when it is higher than the Debye temperature of the material (~170K for Au). As shown below [18]:

$$\frac{Y_{disk}(T)}{Y_{bulk}(T)} = \frac{T_{m(disk)} - T}{T_{m(bulk)} - T} \tag{5.9}$$

Where $Y_{disk}(T)$ and $Y_{bilk}(T)$ are the Young's modulus of the Au disk and bulk Au at temperature T, respectively. The $T_{m(disk)}$ and $T_{m(bulk)}$ are the melting temperature nanodisk and bulk Au. Here we use the melting temperature of bulk polycrystalline Au is 1337K and Young's modulus is 79 GPa. Since the experiment is

conducted at the room temperature which is about 293.15K, the melting temperature of the surface atoms of Au [111] nanocontact is estimated to be ~604K. Previous MD simulations of Au nanoparticles shows that the surface premelting of the Au nanoparticles start at ~500K and the surface totally melt at ~773K [19]. Since the materials are usually stressed and worked in the high temperature in their practical application environments, these result provide a critical temperature for using such nano materials.

5.4 Conclusion

In this chapter, we investigated the deformation process of the Au nanocontact along [110] direction and [111] direction respectively. The Au [110] contact have a uniform diameter along the contact direction. When the nanocontacts are stretched, the length keeps constant and the diameter is reduced. It indicates that the [110] nanocontact is deformed by sliding along the (111) planes in the nanocontacts when stretching.

We also have successful observed the deformation process of Au [111] nanocontact below 2 nm in diameter in atomic-scale by our homemade TEM holder, which the conductance and stiffness was captured at the same time with the TEM observation. Our result shows the [111] contacts are in the hourglass shape and the apex angle of the cone shape kept constant when stretching the nanocontact. We observe that the [111]

contacts introduced the (111) atomic layer at the narrowest constriction during thinning by stretching. This process was achieved by migration of surface atoms from the base part to the contact area. Since the [111] contact kept the same shape during the thinning process, we could estimate the Young modulus of the (111) disk by subtracting the spring constant of the [111] contact before thinning from one after thinning. We obtained the size dependence Young's modulus of the Au (111) disk in the range from 2 to 0.8 nm in diameter, showing that the Young's modulus reduced with reducing the diameter. This dependence can be explained by softening of the surface atoms which Young's modulus was estimated to be about 24 GPa, while the bulk vale is about 120 GPa. The observed surface softening and measured Young's modulus will provide guidance for the designing and fabrications of future nanodevices or nanocatalysts.

References

[1] Y. Kurui, Y. Oshima, M. Okamoto, and K. Takayanagi, Integer Conductance Quantization of Gold Atomic Sheets, Physical Review B (Condensed Matter and Materials Physics) 77, 161403 (2008).

[2] Y. Kurui, Y. Oshima, and K. Takayanagi, One-by-One Evolution of Conductance Channel in Gold [110] Nanowires, Journal of the Physical Society of Japan 76, 123601 (2007).

[3] Y. Kurui, Y. Oshima, M. Okamoto and K. Takayanagi, onductance quantization and dequantization in gold nanowires due to multiple reflection at the interface, Physical Review B 79, 165414 (2009).

[4] Lu Yang, Song Jun, Huang Jian Yu, and Lou Jun, Fracture of Sub-20nm Ultrathin Gold Nanowires, Advanced Functional Materials 21, 3982 (2011).

[5] J.-H. Seo, Y. Yoo, N.-Y. Park, S.-W. Yoon, H. Lee, S. Han, S.-W. Lee, T.-Y. Seong, S.-C. Lee, K.-B. Lee, P.-R. Cha, H. S. Park, B. Kim, and J.-P. Ahn, Superplastic Deformation of Defect-Free Au Nanowires via Coherent Twin Propagation, Nano Letters 11, 3499 (2011).

[6] Y. Oshima and Y. Kurui, In Situ TEM Observation of Controlled Gold Contact Failure under Electric Bias, Physical Review B 87, 081404 (2013).

[7] J. Comtet, A. Lainé, A. Niguès, L. Bocquet, and A. Siria, Atomic Rheology of

Gold Nanojunctions, Nature 569, 393 (2019).

[8] D. Erts, H. Olin, L. Ryen, E. Olsson, and A. Thölén, Maxwell and Sharvin Conductance in Gold Point Contacts Investigated Using TEM-STM, Physical Review B 61, 12725 (2000).

[9] S. Sun, D. Kong, D. Li, X. Liao, D. Liu, S. Mao, Z. Zhang, L. Wang, and X. Han, Atomistic Mechanism of Stress-Induced Combined Slip and Diffusion in Sub-5 Nanometer-Sized Ag Nanowires, ACS Nano 13, 8708 (2019).

[10] P. Liu, Time-Resolved Atomic-Scale Observations of Deformation and Fracture of Nanoporous Gold under Tension, Acta Materialia 10 (2019).

[11] J.-M. Zhang, F. Ma, and K.-W. Xu, Calculation of the Surface Energy of FCC Metals with Modified Embedded-Atom Method, Applied Surface Science 229, 34 (2004).

[12] K. Ishizuka, M. Tomitori, T. Arai, and Y. Oshima, Mechanical Analysis of Gold Nanocontacts during Stretching Using an In-Situ Transmission Electron Microscope Equipped with a Force Sensor, Appl. Phys. Express 13, 025001 (2020).

[13] J. Diao, K. Gall, and M. L. Dunn, Atomistic Simulation of the Structure and Elastic Properties of Gold Nanowires, Journal of the Mechanics and Physics of Solids 52, 1935 (2004).

[14] F. Xu, Q. Qin, A. Mishra, Y. Gu, and Y. Zhu, Mechanical Properties of ZnO Nanowires under Different Loading Modes, Nano Res. 3, 271 (2010).

[15] H. Yao, G. Yun, N. Bai, and J. Li, Surface Elasticity Effect on the Size-Dependent Elastic Property of Nanowires, J. Appl. Phys. 7 (2012).

[16] H. Petrova, J. Perez-Juste, Z. Zhang, J. Zhang, T. Kosel, and G. V. Hartland, Crystal Structure Dependence of the Elastic Constants of Gold Nanorods, J. Mater. Chem. 16, 3957 (2006).

[17] B. Wu, A. Heidelberg, and J. J. Boland, Mechanical Properties of Ultrahigh-Strength Gold Nanowires, Nat. Mater. 4, 525 (2005).

[18] Z. M. Ao, S. Li, and Q. Jiang, The Determination of Young's Modulus in Noble Metal Nanowires, Appl. Phys. Lett. 93, 081905 (2008).

[19] D. M. Foster, Th. Pavloudis, J. Kioseoglou and R.E. Palmer, Atomic-resolution imaging of surface and core melting in individual size-selected Au nanoclusters on carbon, Nat. Commun. 10, 2583 (2019).

Chapter 6 Influence of dislocation on the mechanical properties of Au nanocontact

Introduction

This chapter contains the observation and investigation of edge dislocation in the Au [111] nanocontact.

In Chapter 6.1, we show an edge dislocation in the edge Au [111] nanocontact. The creation and annihilation of the edge dislocation during stretching was analyzed. In Chapter 6.2, we show the influence of the dislocation on the mechanical properties of a crystal.

6.1 Observation of dislocation forming in Au nanocrystal

In the case of nanoscale materials, it is well known that the dislocation is easily removed from the surface, which is different from bulk counterpart. The previous experimental results have indicated that the nanoscale metallic crystals deform though the partial dislocation, which is different from the coarse-grained materials or the bulk one[1-2].

Figure 6.1 shows a [111] nanocontact in which the (111) planes is perpendicular to the contact axis. However, we observed that the (111) planes in left-side base was not parallel to the (111) planes in right-side base as indicate as the red dash line in figure 6.1. The angle between the left-side base and right-side base was estimated to be around 7 degrees by FFT pattern of the TEM image as shown in figure 7.2. In this nanocontacts, the complete FCC crystal structure is observed even though there is an angle between the bases of the two sides.

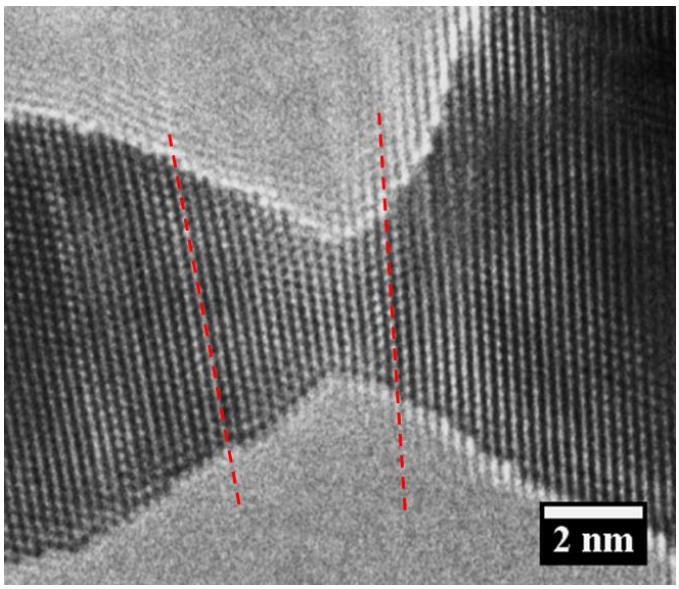

Figure 6.1 TEM image of a nanocontact along the [111] direction. The left-side base and right-side base is tilted with an angle.

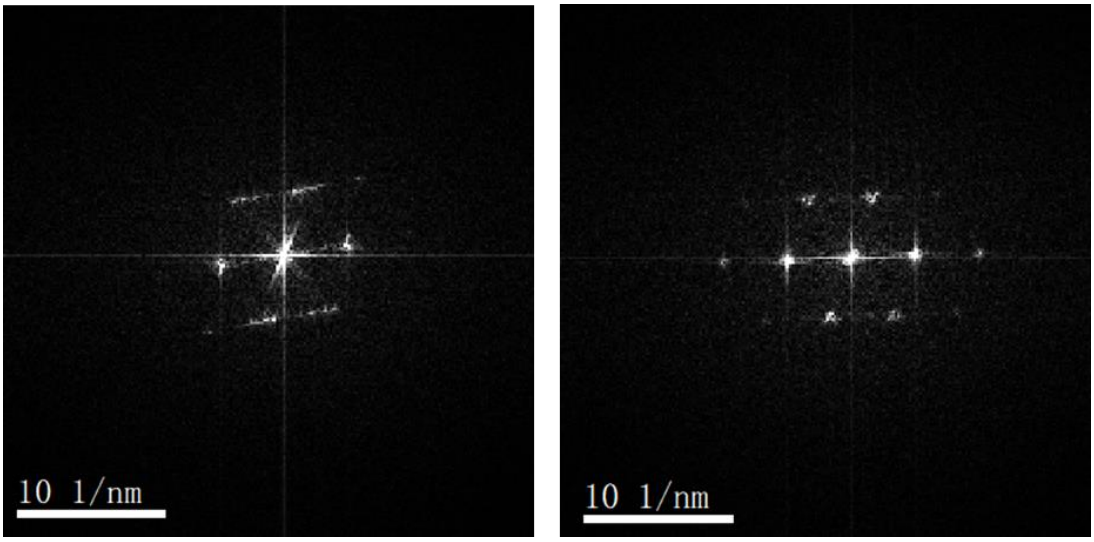

Figure 6.2 FFT patterns of the left-side base (figure in left) and the right-side base (figure in right).

When the nanocontacts was stretched, an edge dislocation was observed to be created in the middle of the nanocontact as shown in figure 6.3a. we found that the (111) plane was introduced only on the upper side of the nanocontact, and the dislocation core existed almost in the center. The dislocation core was observed to move toward the lower side during the stretching as shown in figure 6.3b and c, and finally, it removed from the surface.

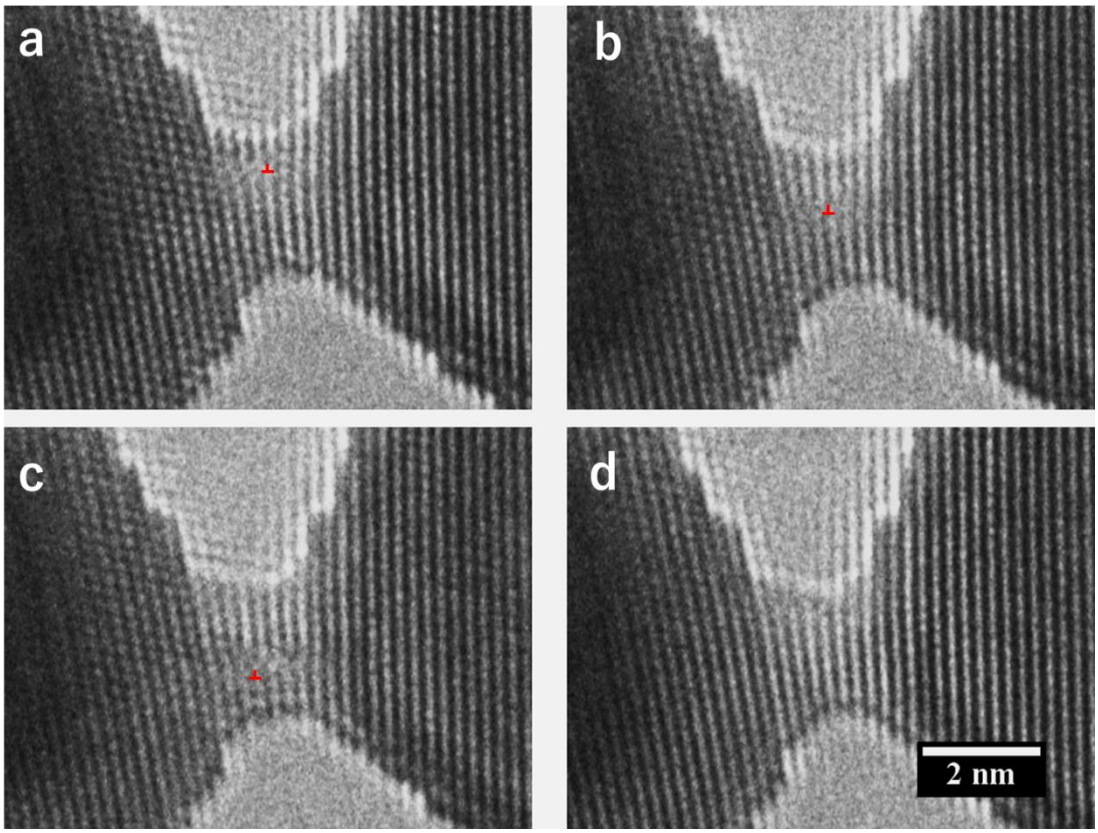

Figure 6.3 Edge dislocation in the [111] nanocontact. A half (111) plane is inserted to the nanocontact. When further stretch the nanocontact, the dislocation climb down as shown in (b) and (c). finally, a complete (111) plane is inserted to the nanocontact.

The deformation process of the contact was analyzed to make the structure model as shown in figure 6.4. At first, when a perfect FCC crystal is stretched, a (111) lattice plane is partially introduced due to orientation tilt between left and right electrodes as shown by green atomic planes in figure 6.4. Such introduction may be caused by migration of the surface atom as we have discussed in the previous chapter. The (111) lattice plane was introduced from the side which have a larger lattice spacing. The atom migration is easily occurred at sub-2nm scale [3]. So when the nanocontact was further stretched, the introduced (111) lattice plane could climb towards the side which lattice spacing is narrower. Finally, when the stretching distance was equal to the spacing of the (111) lattice plane, a (111) lattice plane was fully introduced to the nanocontact and the dislocation disappeared. When the crystal is further stretched, a new (111) lattice plane was inserted and the dislocation was created again. The above process was occurred repeatedly.

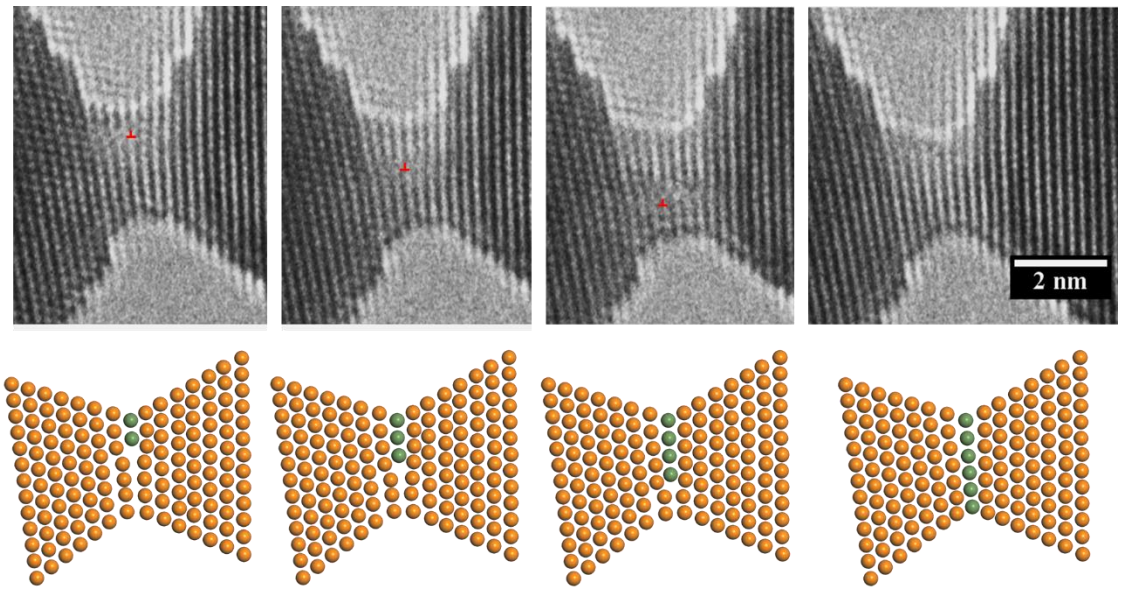

Figure 6.4 Model of the deformation process with the dislocations compared with the TEM images.

6.2 Influence of the dislocation on the mechanical properties of Au nanocrystal

For investigating the influence of the dislocation on the mechanical properties of the Au nanocontact. We measured the conductance and spring constant of the Au [111] nanocontact which have a dislocation.

As shown in Figure 6.5, the conductance shows stepwise changes when stretching it. Interestingly, the plateaus in the conductance traces can be separate into long and short plateaus. The long and stepped short plateaus alternately appear. While, the spring constant decreases to a low value and then recovers to the original value after a while. Such changes occurred repeatedly as the contacts become thinner by stretching, which

correlates with the time evolution in electrical conductance. We found that the range when the spring constant dropped corresponded to the stepped short plateau in the conductance and the range when the spring constant recovered to the original value, to the long plateau as indicated in the figure 6.5.

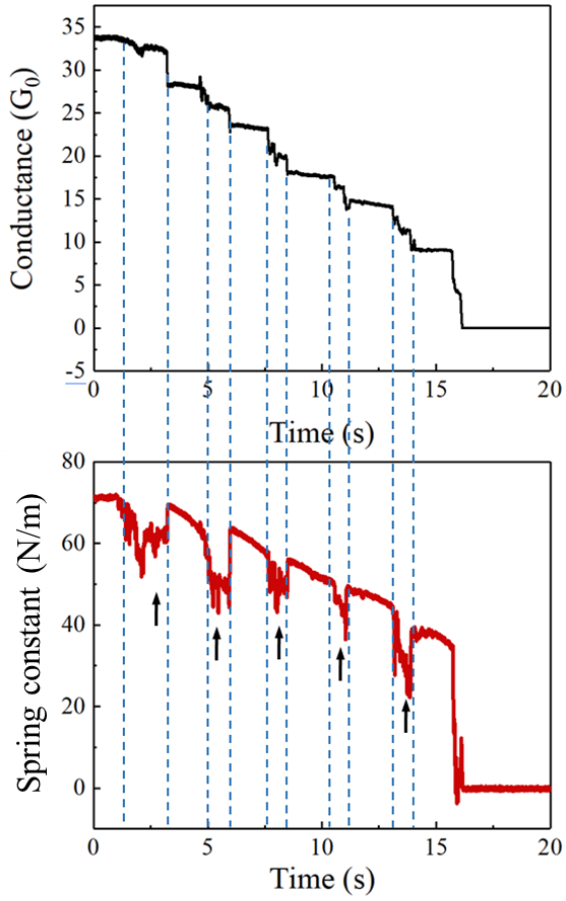

Figure 6.5 Typical variations of conductance, spring constant of an Au nanocontacts during stretching.

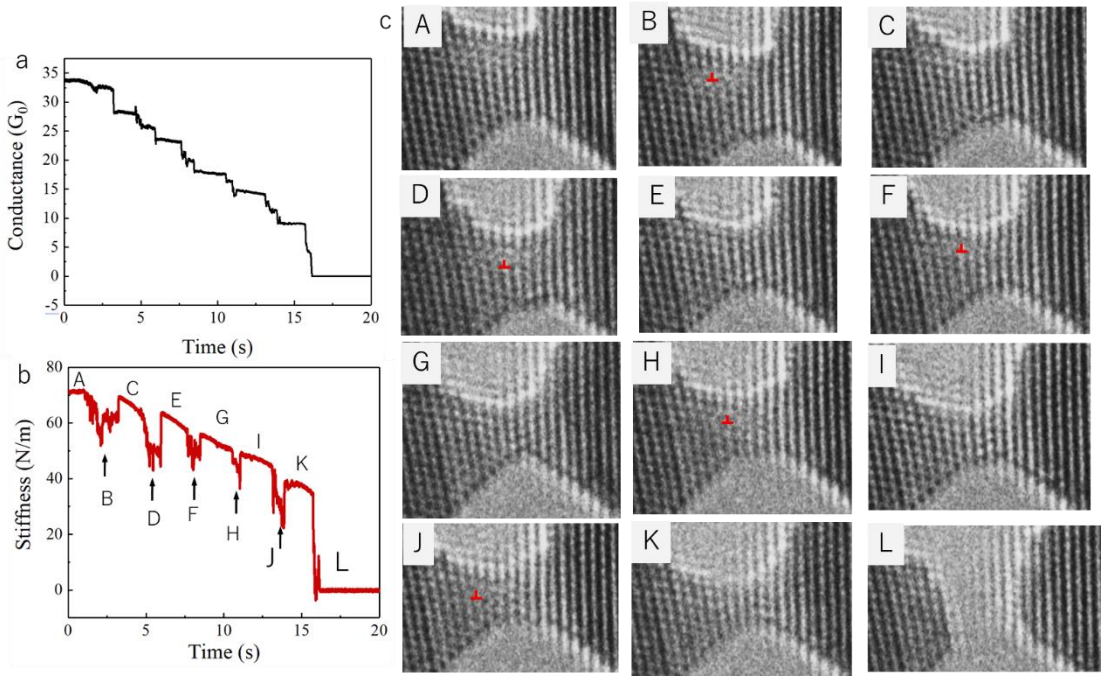

Figure 6.6 (a)Typical variations of conductance and (b) spring constant of an Au nanocontacts during stretching and (c) corresponding TEM images captured at the time indicate in figure (b).

Then we have checked the video and extracted the TEM images at the moment of the normal and low spring constant appeared as shown in figure 6.6. We found that during the stretching of the crystal, the dislocation was repeatedly occurred and disappeared as explained in chapter 6.1. The spring constant reduced when the dislocation occurred, and it was recovered when the dislocation disappeared. This result indicate the dislocation weaken the mechanical properties of the Au nanocontact.

6.3 Conclusion

In this chapter, we investigated the edge dislocation in the Au [111] nanocontact which two bases have an angle. An edge dislocation which is generated by induce a half (111) plane that perpendicular to the stretching direction. After the nanocrystal is stretched, the dislocation will climb toward the direction which lattice spacing is smaller due to the angle between the two bases. Finally, a complete (111) will be inserted thus the dislocation will be disappeared and form a prefect crystal. These processes alternate, so that dislocations appear intermittently.

Then, we investigated the effect of the dislocation on the mechancial properties of Au nanocrystal. When stretching the nanocontact with dislocations, the spring constant sometimes drops to a low value and subsequently recover. This phenomenon always occurred. By comparing with the TEM images, we found the spring constant drop occurred when the dislocation appears, and it will recover when a complete (111) plane is inserted and the crystal is defect free.

All above results indicate that the dislocation is very important for nanoscale crystals and it is a key factor to understanding the mechanical properties of nano materials.

References

[1] L. Wang, P. Guan, J. Teng, P. Liu, D. Chen, W. Xie, D. Kong, S. Zhang, T. Zhu, Z. Zhang, E. Ma, M. Chen, and X. Han, New Twinning Route in Face-Centered Cubic Nanocrystalline Metals, Nat Commun 8, 2142 (2017).

[2] L. Wang, J. Teng, X. Sha, J. Zou, Z. Zhang, and X. Han, Plastic Deformation through Dislocation Saturation in Ultrasmall Pt Nanocrystals and Its in Situ Atomistic Mechanisms, Nano Letters 17, 4733 (2017).

[3] S. Sun, D. Kong, D. Li, X. Liao, D. Liu, S. Mao, Z. Zhang, L. Wang, and X. Han, Atomistic Mechanism of Stress-Induced Combined Slip and Diffusion in Sub-5 Nanometer-Sized Ag Nanowires, ACS Nano 13, 8708 (2019).

Chapter 7 Summary

In this thesis, we demonstrated a new technique, which is an *in situ* TEM holder, equipped with a LER as force sensor, to explore the mechanical properties of nano or atomic-scale materials. This method enables us to clarify the mechanical properties of atomic scale materials by identify their atomic arrangement since the physical properties of atomic-scale materials are strongly depend on their structures.

Chapter 1 introduces mechanical properties of nanomaterials, which is target in this thesis. We explain the importance of the mechanical properties for the nanomaterials. Then we introduce a brief overview of recent theoretical and experimental progress to study the nano-mechanics. Based on these result we explain the advantage of our method.

Chapter 2 introduces the main principles which is important for the measurement in this study. Including the principle of transmission electron microscopy, force measurement by frequency modulation method and the principle of the LER, which is as the force sensor in this study.

Chapter 3 contains all the experiment setup. The detail information including the design and the performance of the design of our TEM-AFM holder is introduced. After that, the sample preparation process is introduced in detail. And the properties of the

force sensor are carefully calibrated. Finally, the method and equipment for conductance and spring constant measurement are introduced.

Chapter 4 introduces mechanical properties of single Pt atomic chains. Around 150 Pt atomic chains are fabricated and the conductance and spring constant value are obtained simultaneously with TEM observation. The spring constant of individual bond in Pt atomic chains is estimated to be 25N/m by remove the contribution of the base part. The mechanical properties of the Pt-Pt bond can be explained by the theory of string tension.

Chapter 5 shows the deformation mechanism and mechanical parties of Au nanocontact are investigated. For the Au [110] nanocontacts, the diameter is uniform diameter along the contact direction. However, for the Au [111] nanocontacts show a hourglass shape which have a narrow neck. When stretching the contact, the [110] nanocontacts mainly deformed though the slide of (111) planes and keep the diameter constant. For the [111] nanocontacts, it deformed by the surface atom migration, which the atoms from the base part to the contact area. The Young's modulus of Au [111] nanocontact decrease with the reduction of the diameter, which can be explained by a core-shell model, that a shell part has a one atom thickness. The Young's modulus of the shell part is only 25GPa, while the core part is around 130GPa almost the same with the one of bulk one. It indicate the surface atoms is much softer and reduce the total

Young's modulus of the materials.

Chapter 6 reports an edge dislocation in the Au [111] nanocontact. A half (111) plane is inserted in to the nanocontact which is perpendicular to the contact direction. The dynamic of the dislocation during stretching the nanocontact is introduced. When stretching the contact along [111] direction, the dislocation climbed and finally a complete (111) surface is formed. When further stretch the nanocontact, the above process is repeated. By measure the spring constant of the nanocontact, we found it reduced when the dislocation appears and recoverd to normal value when the dislocation disappeared by inserted a complete (111) plane. It indicated the dislocation weaken the mechanical properties of materials.

Appendix A

Here we show the method to estimate the spring constant of the base part. The measured stiffness (k_m) can be regarded as a series coupling of the stiffness of a Pt junction (k_j) and of both bases supporting it (k_b) as follows.

$$\frac{1}{k_{total}} = \frac{1}{k_{junction}} + \frac{1}{k_{base}} \quad (1)$$

where k_{total}, $k_{junction}$ and k_{base} correspond to the stiffness of the total, the junction and both bases, respectively. The stiffness of both bases must be larger than one of the total, which the junction is relatively thick (a few nm in diameter). It is reduced until breaking the junction. From this consideration, we noticed that the Pt junction which total stiffness was the same with the stiffness of both bases, must exist during the thinning process. Therefore, we identified the geometry of the Pt junction which total stiffness had the same with the stiffness of both bases by the following calculation and obtained the measured stiffness of the corresponding Pt junction in our experimental data as the stiffness of both bases.

We assume that the base is a quadrangular pyramid which apex is truncated and the Pt junction of a cylindrical shape is connected to the truncated facet of the quadrangular pyramid as shown in Figure S3. By assuming that the Young's modulus is constant, a series coupling of the stiffness of the Pt junction (colored in green) and of the

connecting part (colored in blue) can be obtained as follows.

$$k_b = \frac{1}{E}\left\{\frac{l}{\pi r'^2} + \int_{h'}^{h}\frac{\mathrm{d}x}{\pi x^2 \tan^2\theta_1} + \int_{h'}^{h}\frac{\mathrm{d}x}{\pi x^2 \tan^2\theta_2}\right\}, \quad (2)$$

where x is the coordinate along the axis of Pt junction (Figure S3), r_0 is the radius of the cone, r' and l are the radius and length of the Pt junctions, respectively, θ_1 and θ_2 are the semi-angle of the left and right side's cones, respectively, and h and h' are defined as $h = r_0/\tan\theta$ and $h' = r'/\tan\theta$, respectively. This model is applied to explain the experimental stiffness evaluation of gold [110] noncontact as reported previously. From the geometrical point of view, we can find a thick Pt junction which has the same stiffness with the base parts, supporting the Pt atomic chain as follows.

$$\frac{1}{E}\left\{\int_{h''}^{h}\frac{\mathrm{d}y}{\pi y^2 \tan^2\theta_1} + \int_{h''}^{h}\frac{\mathrm{d}y}{\pi y^2 \tan^2\theta_2}\right\} = \frac{1}{E}\left\{\frac{l}{\pi r'^2} + \int_{h'}^{h}\frac{\mathrm{d}y}{\pi y^2 \tan^2\theta_1} + \int_{h'}^{h}\frac{\mathrm{d}y}{\pi y^2 \tan^2\theta_2}\right\}, \quad (3)$$

Where r'' is the radius of an atomic contact and $h'' = r''/\tan\theta$. The radius of the Pt junction (cone), r', is obtained from expression (3).

$$r' = \sqrt{\frac{(\tan\theta_1 + \tan\theta_2) l r'' + r''}{4}} + r''/2 \quad (4)$$

For the [110]-[110] atomic contact in our experiment, θ_1 and θ_1 are 54º. And the radius of Pt atomic chain (r'') is considered to be 0.15nm.

$$r' = \sqrt{\frac{0.413l + 0.15}{4}} + 0.075 \quad (5)$$

Therefore, the Pt junction with radius of 0.4 nm and length of 0.6nm can be obtained to have the same stiffness with one of the base parts suspending the Pt atomic chain. Figure S1 (a) shows a typical conductance and stiffness evolution of Pt junction during

stretching in the case of the [110]-[110] junction. The TEM image (figure S1 (b)), which was taken at the time indicated by an arrow in Figure S1 (a), shows the Pt junction with such dimensions (almost 0.4 nm in radius and 0.6 nm in length). The corresponding stiffness was measured to be 95.6±5.8 N/m.

For the [111]-[110] atomic contact, θ_1 and θ_2 are 38.5º and 56.5 º, respectively, in our experiment. The following formula was obtained from formula (4).

$$r' = \sqrt{\frac{0.34l+0.15}{4}} + 0.075 \quad (6)$$

The Pt junction with radius of 0.43 nm and length of 0.9 nm can be obtained to have the same stiffness with one of the base parts suspending the Pt atomic chain. Figure S2(a) shows a typical conductance and stiffness evolution of a Pt junction during stretching in the case of the [111]-[110] junction and a TEM image, which was taken at the time indicated by an arrow in Figure S2(b), shows the Pt junction with such dimensions (almost 0.43 nm in radius and 0.9 nm in length). The corresponding stiffness was measured to be 55±3.7 N/m.

In this section, the stiffness of the bases could be estimated from the geometrical point of view. The stiffness of the bases was estimated to be 95.6±5.8 N/m in the case of the [110]-[110] junction and 55±3.7 N/m in the case of the [111]-[110] junction. These values reproduce ones obtained by solving simultaneous equations in the main text, indicating that these values are reasonable.

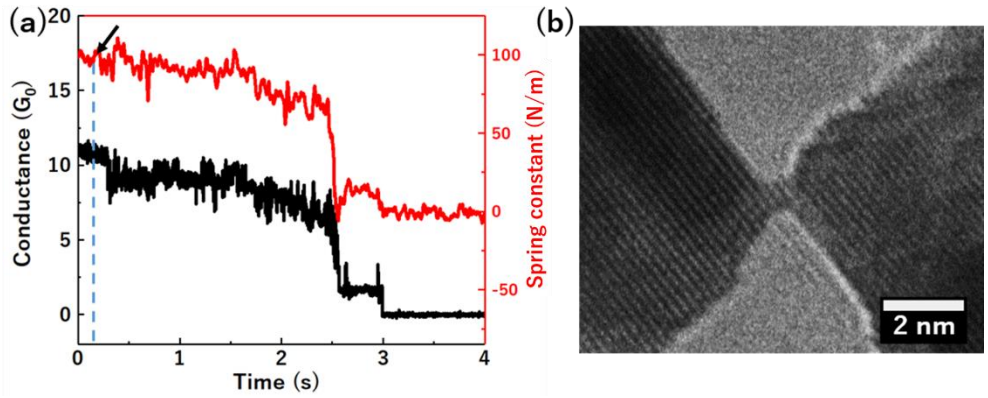

Figure S1. Stiffness of a 110-110 contact and corresponding TEM images. The arrow indicate the time capture the TEM image.

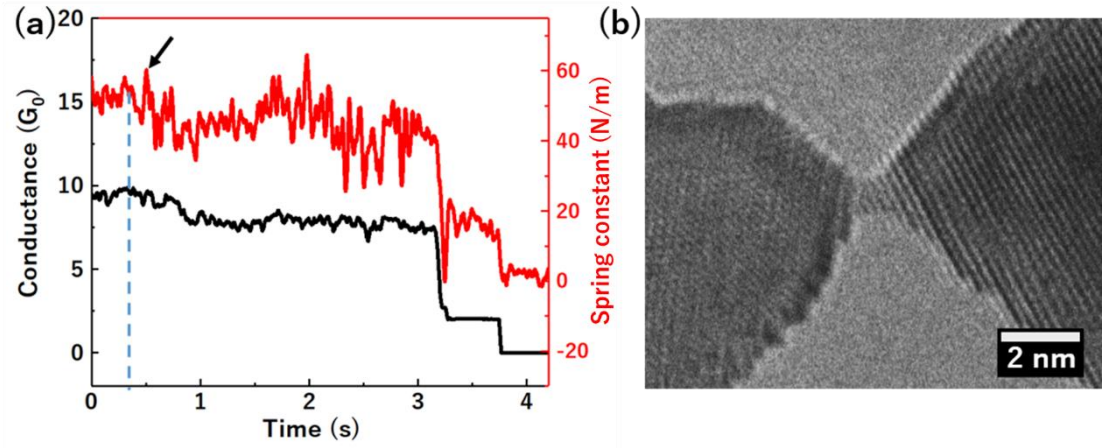

Figure S2. Stiffness of a 110-111 contact and corresponding TEM images. The arrow indicate the time capture the TEM image

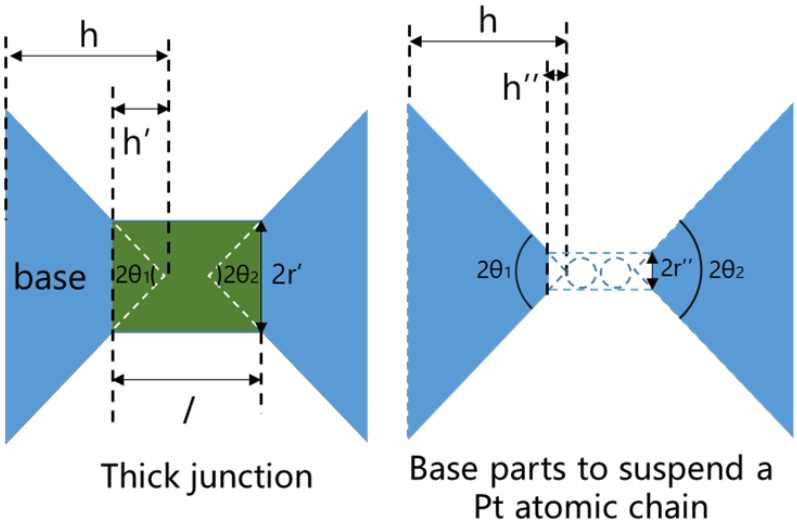

Fig S3. Illustration of the structure model for estimate the spring constant.

Acknowledgements

First of all, I would like to express my sincere thanks to my supervisor, Professor Yoshifumi Oshima. All the research is under his strongly support and great encouragement and advice. Thanks for provided guidance and encouragement on the principles of transmission electron microscopy, know-how on in-situ observation methods, attitudes and ways of thinking about research, and daily life. In addition, I had a valuable experience because I had many opportunities to give presentations in the international conferences. I sincerely thank you.

Then I would like to express my deep thanks to Prof. Masahiko Tomitori, my Second supervisor, provided me with various advice and suggestions based on our abundant experience and knowledge in atomic force microscopy. In addition, he read my papers carefully and giving me useful comments on my papers.

I also would like to thank Prof. Toyoko Arai of the Graduate School of Natural Sciences, Kanazawa University, who was our collaborator, gave us many advices from the perspective of a non-contact atomic force microscope expert.

I am thankful for Prof. Ryo Maezono, who is the supervisor of my minor research. He gives me advices for the DFT calculations from the calculation method to the analysis of the calculation results.

I also thank Prof. Kenta Hongo for supporting the DFT calculations and suggestion on the calculated result and assistance with the analysis.

I would like to express my appreciation to Dr. Ishizuka and Mr. Kobori in our lab for their suggestion and discussion to the experiment. I also thanks my fellow lab mates Ms. Chiew, Mr. Chen, Mr. Honda, Mr Liu and Mr. Xie for the kindly discussions and useful ideas when working together. Especially, I am greatly thanks to my husband Mr. Zhang for the designing of TEM holder and useful suggestions for improving my experiments.

In addition, thanks for MEXT scholarship which support me during the doctoral course.

Finally, I would like to express my gratitude again to all those who supported me to complete this dissertation and help me in life.

List of Publications

[1] Jiaqi Zhang, Keisuke Ishizuka, Masahiko Tomitori, Toyoko Arai and Yoshifumi Oshima, “Atomic scale mechanics explored by in situ transmission electron microscopy with a quartz length-extension resonator as a force sensor” Nanotechnology. 2020, 31, 205706.

[2] Jiaqi Zhang, Keisuke Ishizuka, Masahiko Tomitori, Toyoko Arai, Kenta Hongo, Ryo Maezono, Erio Tosatti, Yoshifumi Oshima, “Atom-mechanics in platinum monatomic chains.” (submitted)

[3] Chunmeng Liu , Jiaqi Zhang, Muruganathan Manoharana, Hiroshi Mizuta, Yoshifumi Oshima, Xiaobin Zhang, “Origin of nonlinear current-voltage curves for suspended zigzag edge graphene nanoribbon.” Carbon. 2020, 165, 476-483.

[4] Jiaqi Zhang, Keisuke Ishizuka, Masahiko Tomitori, Toyoko Arai, Yoshifumi Oshima, “Size dependent Young’s modulus of sub-2nm gold nanocontacts” (in preparation)

Presentation

- **International Conference (Poster)**

1. Jiaqi Zhang, Yuki kobori, Keisuke Ishizuka, Masahiko Tomitori, Toyoko Arai and Yoshifumi Oshima, "Mechanical Properties of Pt Nano-contacts Measured by TEM Combined with a Frequency-Modulation Force Sensor", 10th International Conference on Materials for Advanced Technologies (ICMAT) No. 191177, 25th, June, 2019, Singapore.

2. Jiaqi Zhang, Yuki kobori, Keisuke Ishizuka, Masahiko Tomitori, Toyoko Arai and Yoshifumi Oshima, "Mechanical Properties of Metal Nano-contacts Measured by TEM Combined with Frequency Modulation Force Sensor" (7P-005), Asian Conference on Nanoscience and Nanotechnology 2018 October 18-21th, Qingdao (China)

- **Domestic Conference**

1. Jiaqi Zhang, Yuki kobori, Keisuke Ishizuka, Masahiko Tomitori, Toyoko Arai and Yoshifumi Oshima, “Mechanical properties of Pt nano-contacts measured by TEM

combined with a frequency-modulation force sensing system” The 66th JSAP spring meeting, 9p-PA5-3, 9th, March, 2019, Tokyo Institute of Technology

2. Jiaqi Zhang, Yuki kobori, Keisuke Ishizuka, Masahiko Tomitori, Toyoko Arai and Yoshifumi Oshima, "Mechanical properties of Pt nano-contacts measured by TEM combined with frequency modulation force sensor" The 74th Annual Meeting of the Japanese Society of Microscopy, P-M_48, 8th, June, 2019, Nagoya convention center

3. Jiaqi Zhang, Keisuke Ishizuka, Masahiko Tomitori, Toyoko Arai and Yoshifumi Oshima, "Mechanical properties of Pt atomic chain measured by TEM combined with a frequency-modulation force sensing system" The 80th JSAP autumn meeting, 19th, September, 2019, 19a-C310-4, Hokkaido University

4. Jiaqi Zhang, Keisuke Ishizuka, Masahiko Tomitori, Toyoko Arai and Yoshifumi Oshima "Mechanical properties of Pt atomic chain measured by TEM combined with a frequency-modulation force sensing system" Annual meeting of the Japan Society of Vacuum and Surface Science 2019, 3Ea05S, 31th, October, 2019, Tsukuba

5. Jiaqi Zhang, Keisuke Ishizuka, Masahiko Tomitori, Toyoko Arai and Yoshifumi

Oshima, "Mechanical properties of Pt-Pt bond in an atomic chain measured by TEM combined with a frequency-modulation force sensing system" The 67th JSAP Spring meeting, 13th, March, 2020, 13p-D519-1~12, Sophia University